

Simulations of Particle Dynamics in Stokes Flow: Polydispersity and Flexibility

Li, H.

DOI

[10.4233/uuid:38963e7c-295c-4a60-9db4-898be64f1f91](https://doi.org/10.4233/uuid:38963e7c-295c-4a60-9db4-898be64f1f91)

Publication date

2025

Document Version

Final published version

Citation (APA)

Li, H. (2025). *Simulations of Particle Dynamics in Stokes Flow: Polydispersity and Flexibility*. [Dissertation (TU Delft), Delft University of Technology]. <https://doi.org/10.4233/uuid:38963e7c-295c-4a60-9db4-898be64f1f91>

Important note

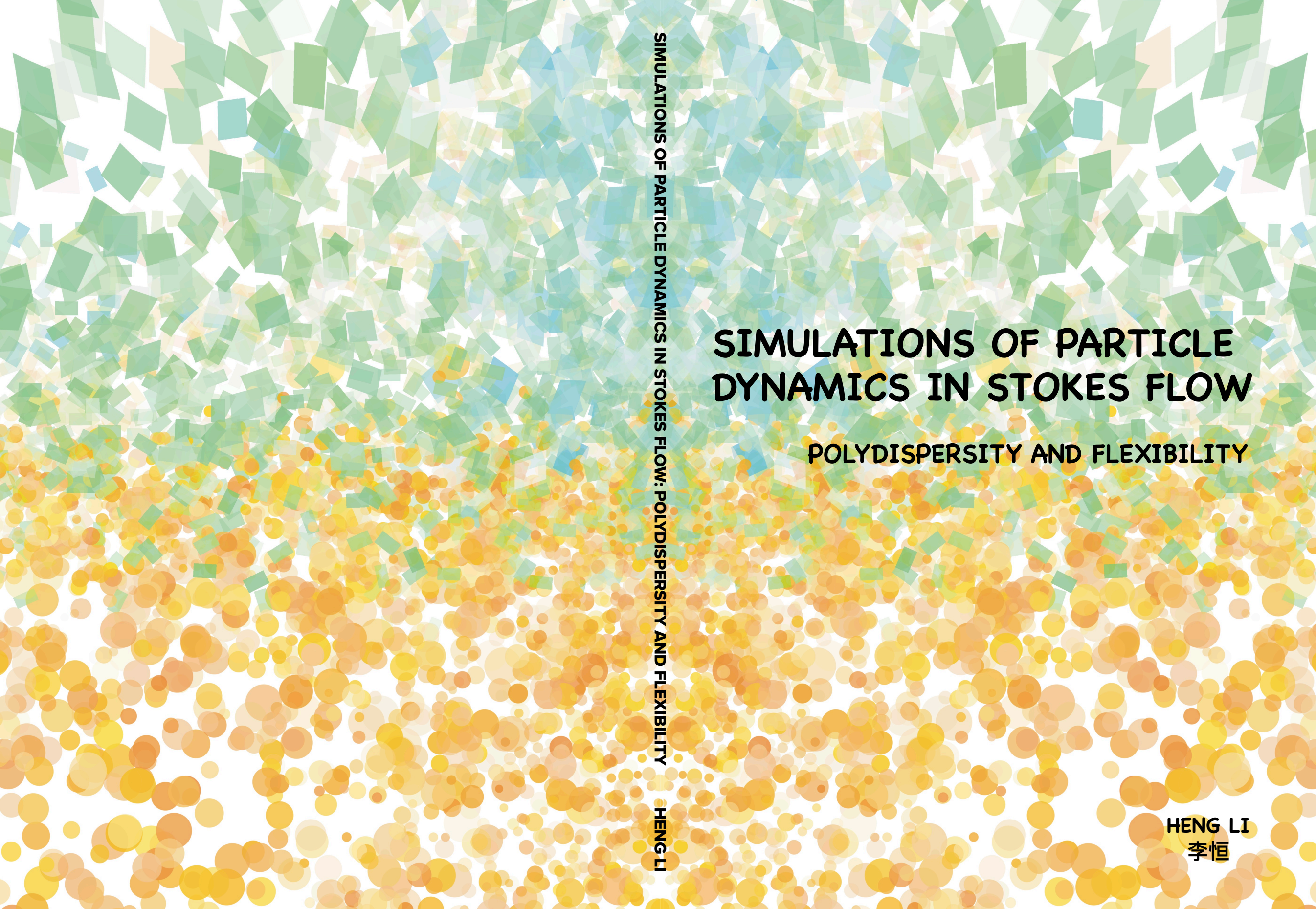
To cite this publication, please use the final published version (if applicable). Please check the document version above.

Copyright

Other than for strictly personal use, it is not permitted to download, forward or distribute the text or part of it, without the consent of the author(s) and/or copyright holder(s), unless the work is under an open content license such as Creative Commons.

Takedown policy

Please contact us and provide details if you believe this document breaches copyrights. We will remove access to the work immediately and investigate your claim.



SIMULATIONS OF PARTICLE DYNAMICS IN STOKES FLOW

POLYDISPERSITY AND FLEXIBILITY

SIMULATIONS OF PARTICLE DYNAMICS IN STOKES FLOW: POLYDISPERSITY AND FLEXIBILITY HENG LI

HENG LI
李恒

HENG LI

SIMULATIONS OF PARTICLE DYNAMICS IN STOKES FLOW:
POLYDISPERSITY AND FLEXIBILITY

Simulations of Particle Dynamics in Stokes Flow: Polydispersity and Flexibility

Dissertation

for the purpose of obtaining the degree of doctor
at Delft University of Technology
by the authority of the Rector Magnificus, prof.dr.ir. T.H.J.J. van der Hagen,
chair of the Board for Doctorates
to be defended publicly on
Thursday 26 June 2025 at 15:00 o'clock

by

Heng LI

Master of Science in Fluid Mechanics,
Zhejiang University, Hangzhou, China,
born in Henan, China.

This dissertation has been approved by the promotor.

Composition of the doctoral committee:

Rector Magnificus,	chairperson
Dr. L. Botto	Delft University of Technology, promotor
Prof. dr. ir. J. T. Padding	Delft University of Technology, promotor

Independent members:

Prof. dr. ir. C. Poelma	Delft University of Technology
Prof. dr. ir. D. L. Schott	Delft University of Technology
Dr. B. Delmotte	École Polytechnique Paris / CNRS, France
Dr. S. Pirola	Delft University of Technology
Prof. dr. ir. W. de Jong	Delft University of Technology, reserve member

This work was funded by the European Research Council (ERC) under the European Union's Horizon 2020 research and innovation program (Grant Agreement No. 715475, project FLEXNANOFLOW).



European Research Council
Established by the European Commission

Cover by: Julia Jeblick

Printed by: Ridderprint | www.ridderprint.nl

Copyright © 2025 by H. Li, all rights reserved

ISBN 978-94-6518-063-2

An electronic version of this dissertation is available at

<http://repository.tudelft.nl/>

CONTENTS

SUMMARY	ix
SAMENVATTING	xi
Part I	1
1 INTRODUCTION	3
1.1 Background	4
1.1.1 Liquid processing of nanosheets	4
1.1.2 Size distribution of nanosheets produced by LPE	5
1.1.3 Fractionation of nanosheets by centrifugation	6
1.1.4 Flexibility influences the shapes of nanosheets in flows	8
1.2 Motivation	9
1.3 Thesis objectives and outline	12
References	19
2 FUNDAMENTALS OF MICROHYDRODYNAMICS	21
2.1 Introduction	22
2.2 Point force and other singularities	22
2.3 Integral representation and multipole expansion	24
2.4 Numerical methods	25
References	31
3 ANALYSIS AND OPTIMIZATION OF A MULTICASCADE METHOD	33
3.1 Introduction	34
3.2 Overview of mathematical models of sedimentation/centrifugation	36
3.3 Mathematical model of this chapter	37
3.4 Results and discussion	40
3.4.1 Time evolution of the frequency distribution: supernatant v.s. sediment layer	40
3.4.2 Particle fractions in the supernatant and in the sediment layer	41
3.4.3 Minimisation of impurities	45
3.5 Practical applications of the theory	51
3.5.1 Fractionation of nearly spherical metallic nanoparticles (isotropic particles)	51
3.5.2 Fractionation of graphene (anisotropic particles)	53
3.6 Conclusions	55
References	63

4	HINDERED SETTLING OF A LOG-NORMALLY DISTRIBUTED STOKESIAN SUSPENSION	65
4.1	Introduction	66
4.2	Overview of one-dimensional models for the class-averaged settling velocity	68
4.3	Numerical approach and validation	69
4.3.1	Relation between the mobility formulation and Batchelor's formula	75
4.4	Hindered settling of monodisperse and bidisperse suspensions	76
4.5	Polydisperse suspensions	79
4.5.1	Velocity statistics	79
4.5.2	Comparison with hindered settling models	85
4.5.3	Velocity slip	87
4.6	Comparison with dynamic simulations	91
4.7	Summary and discussion	92
	References	106
5	ENHANCED SETTLING OF A GROUP OF SPHERES	107
5.1	Introduction	108
5.2	Experimental method	109
5.3	Simulation approach	111
5.4	Results and discussions	112
5.5	Conclusions	122
	References	128
6	BUCKLING OF FLEXIBLE SHEETS IN SHEAR FLOW	129
6.1	Introduction	130
6.2	Experiments	131
6.3	Simulation Method	132
6.4	Dynamics of a single sheet	134
6.5	Dynamics of a pair of parallel sheets	136
6.6	Conclusion	142
	References	148
7	CONCLUSIONS AND RECOMMENDATIONS	149
7.1	Conclusions	150
7.2	Recommendations	154
	References	155
	Part II Appendices	157
A	APPENDIX TO CHAPTER 3	159
A.1	Derivation of Eq.3.8	159
A.2	Derivation of Eq.3.10	160

B	APPENDIX TO CHAPTER 4	161
B.1	Derivation of the slip velocity closure in the MLB model	161
C	APPENDIX TO CHAPTER 6	163
C.1	PIV measurement of the shear flow	163
C.2	Angle versus time for two parallel sheets	164
C.3	Curvature versus time	164
C.4	Measurement of the curvature and orientation	165
C.5	Fig.6.2(b) in lin-lin scale and log-log scale	165
C.6	Maximum curvature versus elastoviscous number for a single sheet from simulations	166
C.7	Non-monotonic relation between curvature and separation distance . .	166
C.8	Curvatures of convex shapes	168
	References	171
	Part III	173
	ACKNOWLEDGMENTS	175
	CURRICULUM VITÆ	177
	LIST OF PUBLICATIONS	179

SUMMARY

2D materials are promising high-performance sheet-like nanomaterials with unique properties. Liquid-phase exfoliation (LPE) is a scalable and cost-effective process to produce 2D materials on large scales. However, the product of LPE is highly polydispersed. An efficient procedure to fractionate 2D materials is the liquid cascade centrifugation (LCC), which is currently done by trial and error. Moreover, 2D materials are easily deformed when processed in liquids because of their low bending rigidities. To exploit the unique properties of 2D materials, it is essential to control the sizes and morphologies of the nanosheets.

To provide insights for the rational design of the LCC procedure and the understanding of deformation of nanosheets in the shear flow, this thesis tackles two relevant fluid dynamics problems: (i) sedimentation of polydisperse suspensions, and (ii) buckling of flexible particles in the shear flow, both in the Stokes flow regime. The approaches adopted in this thesis are mainly numerical, including Stokesian dynamics and boundary integral method, which are efficient methods to simulate particle dynamics in Stokes flow. Moreover, collaborations with experimentalists have been established during this thesis. The code developed has been used to answer practical questions (e.g. see chapter 5).

The objective of understanding sedimentation of polydisperse suspensions is to be able to analyze the liquid cascade centrifugation of polydisperse systems and to design centrifugation procedures with theoretical guidelines for particle size fractionation. In chapter 3, a one-dimensional sedimentation model is used to predict the time evolution of the volume fraction distribution of each size class for a polydisperse size distribution. Assuming the suspension to be dilute, the settling velocity of each size class is calculated by the corresponding Stokes velocity, neglecting hydrodynamic interactions. Using this model, the outcomes of the centrifugation procedure including the purity and yield are analyzed. Moreover, an optimized procedure is proposed based on the analysis. This work establishes a theoretical framework for analyzing and rationally designing the centrifugation procedures. In chapter 4, the effect of hydrodynamic interactions on the particle settling velocities of polydisperse suspensions is studied. Settling velocity statistics for dilute suspensions of polydisperse spheres are generated from Stokesian dynamics simulations. Both the average velocities and the velocity fluctuations of each size class are analyzed. Moreover, the validities of existing polydisperse hindered settling models are examined by comparing model predictions with our numerical results. It is found that current models fail to predict the settling velocities of small size classes in a polydisperse size distribution. Potential

model improvements are discussed. This is the first work where velocity statistics of each size class in a widely polydisperse system are reported in the literature. In chapter 5, the implications of the widely used experimental procedure based on pipetting a suspension drop in a settling tank to measure the single particle Stokes velocity are discussed. This is a collaborative work with experimentalists from Deltares who conducted the experiments. The developed Stokesian dynamics code is used to illustrate the effect of hydrodynamic interactions in this experimental procedure. We found that the particle Stokes velocities are overestimated by a large margin in measurements following this experimental procedure.

For the second problem, we want to understand what is the criterion for a flexible sheet to buckle in the shear flow, and how hydrodynamic interactions change this criterion for a pair of sheets. In chapter 6, both experiments and simulations are carried out to answer these questions. The simulations are done by me using the boundary integral method, and the experiments are done by a collaborator using thin Mylar sheets in a shear cell. The criterion for a single sheet to buckle based on the competition between the viscous force from the shear flow and the elastic response of the sheet is characterized, with a good match between experiments and simulations. Surprisingly, a pair of sheets bend under a much lower shear rate compared to that for a single sheet given the same material properties. This is attributed to the hydrodynamic interactions between the sheets which exert lateral loads on the sheets. This is the first study where the buckling threshold for a pair of flexible particles in the shear flow is measured in the literature. Our study suggests that the deformation of flexible sheets in a shear suspension may not only depend on the mechanical and geometric properties of the sheets, but also on the microstructure of the suspension (e.g. sheet orientation and pair-sheet distance).

Overall, this thesis contributes to the understanding of particle dynamics in Stokes flow, including the settling of polydisperse suspensions and buckling of flexible sheets in the shear flow, utilizing the theories and numerical approaches of microhydrodynamics. Results of this thesis can be used to optimize the procedures of liquid processing of 2D nanomaterials and in other relevant applications.

SAMENVATTING

2D-materialen zijn veelbelovende, hoogwaardige nanomaterialen in de vorm van platen met unieke eigenschappen. Vloeistoffase-exfoliatie (Engels: liquid-phase exfoliation, LPE) is een schaalbare en kosteneffectieve methode om 2D-materialen op grote schaal te produceren. Het product van LPE is echter sterk polydispers. Een efficiënte methode om 2D-materialen te fractioneren is vloeistofcascade-centrifugatie (Engels: liquid cascade centrifugation, LCC), die momenteel wordt uitgevoerd door middel van vallen en opstaan. Bovendien vervormen 2D-materialen gemakkelijk tijdens verwerking in vloeistoffen vanwege hun lage buigstijfheid. Om de unieke eigenschappen van 2D-materialen te benutten, is het essentieel om de grootte en morfologie van de nanoplaten te controleren.

Om inzicht te geven in het rationeel ontwerp van de LCC-procedure en in het begrijpen van de vervorming van nanobladen in een schuifstroming, dit proefschrift behandelt twee relevante problemen uit de stromingsleer: (i) sedimentatie van polydisperse suspensies, en (ii) het knikken van flexibele deeltjes in een schuifstroom, beide in het Stokes-stroomregime. De aanpak in dit proefschrift is voornamelijk numeriek, waaronder Stokesian dynamics en de boundary integral method, die efficiënte methoden zijn om de dynamica van deeltjes in Stokes-stromen te simuleren. Daarnaast zijn samenwerkingen met experimentele onderzoekers opgezet tijdens dit onderzoek. De ontwikkelde code is gebruikt om praktische vragen te beantwoorden (bijvoorbeeld in hoofdstuk 5).

Het doel van het begrijpen van sedimentatie van polydisperse suspensies is om de vloeistofcascade-centrifugatie van polydisperse systemen te analyseren en centrifugeerprocedures te ontwerpen met theoretische richtlijnen voor de fractionering van deeltjesgroottes. In hoofdstuk 3 wordt een eendimensionaal sedimentatiemodel gebruikt om de tijdsevolutie van de volumefractieverdeling van elke grootteklasse te voorspellen voor een polydisperse grootteverdeling. Aangenomen dat de suspensie verdund is, wordt de zinksnelheid van elke grootteklasse berekend met behulp van de overeenkomstige Stokes-snelheid, waarbij hydrodynamische interacties worden genegeerd. Met dit model worden de uitkomsten van de centrifugeerprocedure, inclusief de zuiverheid en opbrengst, geanalyseerd. Bovendien wordt een geoptimaliseerde procedure voorgesteld op basis van de analyse. Dit werk vormt een theoretisch kader voor het analyseren en rationeel ontwerpen van centrifugeerprocedures. In hoofdstuk 4 wordt het effect van hydrodynamische interacties op de deeltjeszinksnelheden van polydisperse suspensies bestudeerd. Zinksnelheidsstatistieken voor verdunde suspensies van polydisperse bollen worden gegenereerd met Stokesian dynamics

simulaties. Zowel de gemiddelde snelheden als de snelheidsfluctuaties van elke grootteklasse worden geanalyseerd. Daarnaast wordt de geldigheid van bestaande modellen voor polydisperse gehinderde sedimentatie onderzocht door modelvoorspellingen te vergelijken met onze numerieke resultaten. Er wordt vastgesteld dat huidige modellen falen in het voorspellen van de zinksnelheden van kleine grootteklassen in een polydisperse grootteverdeling. Mogelijke verbeteringen aan modellen worden besproken. Dit is het eerste werk waarin snelheidsstatistieken van elke grootteklasse in een breed polydispers systeem worden gerapporteerd in de literatuur. In hoofdstuk 5 worden de implicaties besproken van de veelgebruikte experimentele methode waarbij een druppel suspensie wordt gepipetteerd in een sedimentatietank om de Stokes-snelheid van individuele deeltjes te meten. Dit is een samenwerking met experimentele onderzoekers van Deltares, die de experimenten hebben uitgevoerd. De ontwikkelde Stokesian dynamics code wordt gebruikt om het effect van hydrodynamische interacties in deze experimentele methode te illustreren. We ontdekten dat de Stokes-snelheden van deeltjes aanzienlijk worden overschat bij metingen die deze methode volgen.

Voor het tweede probleem willen we begrijpen wat het criterium is voor een flexibele plaat om te knikken in een schuifstroom, en hoe hydrodynamische interacties dit criterium veranderen voor een paar platen. In hoofdstuk 6 worden zowel experimenten als simulaties uitgevoerd om deze vragen te beantwoorden. De simulaties zijn door mij uitgevoerd met behulp van de boundary integral method, en de experimenten zijn uitgevoerd door een samenwerkingspartner met behulp van dunne Mylar-platen in een schuifcel. Het criterium voor een enkele plaat om te knikken, gebaseerd op de competitie tussen de viskeuze kracht van de schuifstroom en de elastische respons van de plaat, is gekarakteriseerd, met een goede overeenkomst tussen experimenten en simulaties. Verrassend genoeg buigen een paar platen bij een veel lagere schuifnelheid dan een enkele plaat met dezelfde materiaaleigenschappen. Dit wordt toegeschreven aan de hydrodynamische interacties tussen de platen, die zijdelingse krachten uitoefenen op de platen. Dit is de eerste studie waarin de knikdrempel voor een paar flexibele deeltjes in een schuifstroom wordt gemeten in de literatuur. Onze studie suggereert dat de vervorming van flexibele platen in een schuif suspensie niet alleen afhankelijk kan zijn van de mechanische en geometrische eigenschappen van de platen, maar ook van de microstructuur van de suspensie (bijvoorbeeld de oriëntatie van de platen en de afstand tussen de platen).

Over het geheel genomen draagt dit proefschrift bij aan het begrip van deeltjesdynamica in Stokes-stroom, inclusief de sedimentatie van polydisperse suspensies en het knikken van flexibele platen in schuifstroom, met gebruikmaking van de theorieën en numerieke methoden van microhydrodynamica. De resultaten van dit proefschrift kunnen worden gebruikt om de procedures voor vloeistofverwerking van 2D-nanomaterialen te optimaliseren en in andere relevante toepassingen.

PART I

INTRODUCTION

Two-dimensional materials are promising high-performance materials due to their unique properties. Liquid-phase exfoliation is an effective way to produce them in large amounts. However, the products of liquid-phase exfoliation are highly polydispersed, which hinders their applications. Moreover, due to their high flexibility, two-dimensional materials are easily deformed during liquid-phase exfoliation. This thesis provides insights for the size fractionation of polydisperse particles and the deformation of flexible particles in the shear flow. In this chapter, the background of liquid processing of two-dimensional materials is introduced, where the research questions are identified. The objectives and outline of this thesis are also provided.

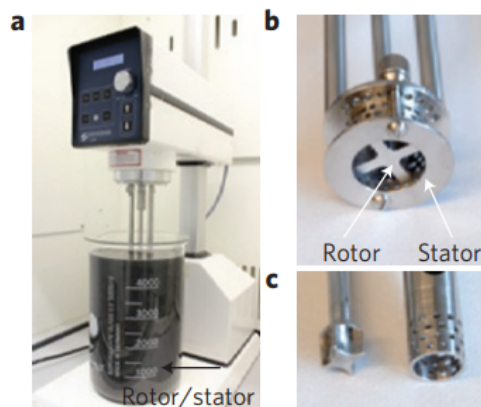


Figure 1.1: A high-shear mixer with mixing head in a beaker of graphene dispersion and a close-up view of the mixing head. Reproduced from [4].

1.1 Background

1.1.1 Liquid processing of nanosheets

Two-dimensional (2D) materials (e.g. graphene, MoS_2 , WS_2 , BN) are crystalline materials consisting of single- or few-layer atoms, which are sheet-like particles with lateral length around $O(1 \mu\text{m})$ and thickness around $O(1 \text{nm})$. They are promising high-performance materials due to their unique electrical, optical, mechanical, chemical and thermal properties [1]. For example, graphene could be useful in over 40 major application areas such as composites, energy storage, thermal management, sensors and coatings [2]. Many of these applications will require few-layer graphene flakes (< 10 layers) in large multi-tonne quantities. Production of graphene has increased from 14 tonnes in 2009 to nearly 120 tonnes in 2015, and is nearly 1200 tonnes in 2019 [3].

One effective way to produce large amount of graphene flakes is by liquid-phase exfoliation (LPE) [1]. The most common techniques to undertake exfoliation in liquid are ultrasonication, ball milling, shear-mixing, electrochemical exfoliation, wet-jet milling and microfluidization. One of the apparatuses used in LPE is shown in figure 1.1. In LPE, microparticles of graphite are suspended in a liquid solvent, and the resulting colloidal dispersion is subject to energetic mixing. At a critical value of the local shear rate, layers of graphene are removed from the mother graphite particles. The micro-mechanics in LPE has been previously studied, and two models are developed: a sliding model for relatively rigid nanosheets [5] and a peeling model for graphene sheets which are able to bend [6, 7]. The product of LPE is a mixture of plate-like particles having different thicknesses and lateral lengths suspended in a liq-

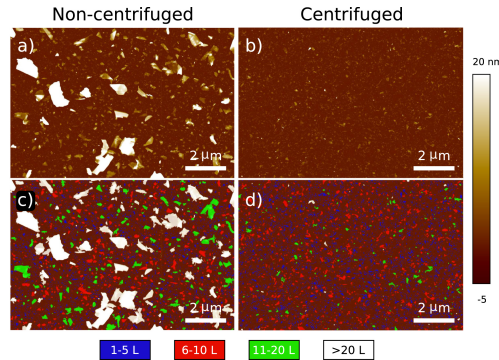


Figure 1.2: AFM images of two graphene dispersions. (a) and (c) show a non-centrifuged dispersion. (b) and (d) show a centrifuged dispersion. The labelled flakes in (c) and (d) in blue, red, green and white colors are flakes with 1-5, 6-10, 11-20 and more than 20 layers, respectively. Reproduced from [10].

uid solvent. The lateral dimension of graphene flakes produced by LPE is from a few tens of nanometers to a few micrometers, and the thickness varies from monolayer to more than ten layers. Before being put to applications, the product of LPE should be fractionated by their sizes since specific applications require certain size ranges.

Besides polydispersity, another two properties of graphene nanosheets which will influence their qualities (e.g. shape of the flakes) when being produced by LPE and transport properties (e.g. viscosity of the suspension) when being transported in liquids are anisotropy and flexibility. Graphene nanosheets are highly anisotropic with aspect ratio of $O(1000)$ since their lateral sizes are about $1 \mu\text{m}$ and thicknesses are about 1 nm . It was found that due to surface slip, Jeffery orbit might be suppressed and a graphene nanosheet might attain a stable orientation in shear flow [8]. Graphene has very high Young's modulus and very low bending stiffness [9], so out-of-plane bending might happen and influence the morphology of graphene nanosheets in shear flows.

1.1.2 Size distribution of nanosheets produced by LPE

The nanosheets produced by LPE are polydisperse, as can be seen from the AFM images of a graphene dispersion shown in figure 1.2 (a) and (c). There are many flakes with more than 10 layers, which are graphite, and they can be removed by centrifugation (see figure 1.2 (c) and (d)).

The characterization of lateral size and thickness of nanosheets produced by LPE is shown in figure 1.3. From figure 1.3 (a) and (c), it is seen that both the lateral size and thickness follow approximately log-normal distributions. The slopes of the dotted

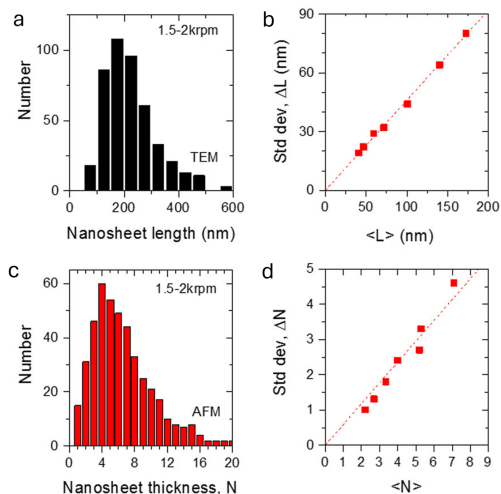


Figure 1.3: Lateral size (a) and thickness (c) distributions of nanosheets produced by LPE after pre-centrifugation. Correlations between standard deviations and mean values of lateral size (b) and thickness (d) of nanosheets under different centrifugation strengths. Reproduced from [11].

lines in figure 1.3 (b) and (d) are 0.46 and 0.59, respectively, which means the standard deviation of lateral size with aspect to mean lateral size is $\Delta L / \langle L \rangle \sim 0.46$, and the standard deviation of thickness (i.e. number of layers) with respect to mean thickness is $\Delta N / \langle N \rangle \sim 0.59$.

Log-normal distributions are almost universal when the particle size distribution is the result of repetitive break-up processes [12]. For example, growth and division processes of cells could lead to a log-normal cell size distribution [13]. Log-normal approximations are used to model the size distributions of aerosols due to their Brownian coagulation [14, 15]. The size distribution of cohesive sediment in the river also can be fitted well by a log-normal distribution because of flocculation [16–18].

1.1.3 Fractionation of nanosheets by centrifugation

The broad size distributions of the nanosheets produced by LPE hamper their applications, since most applications need controlled nanosheet sizes. For example, large nanosheets are suitable for mechanical reinforcement [20], whereas small ones are preferred for catalysis [21]. For the inks used for printed optoelectronic devices, they have to be monolayer nanosheets enriched [22], whereas the dispersions after LPE contain very low amount of monolayer nanosheets as seen from the previous section (typically lower than 10%). Moreover, after size selection, the graphene produced from LPE can form networks with increasing electrical conductivity as the lateral

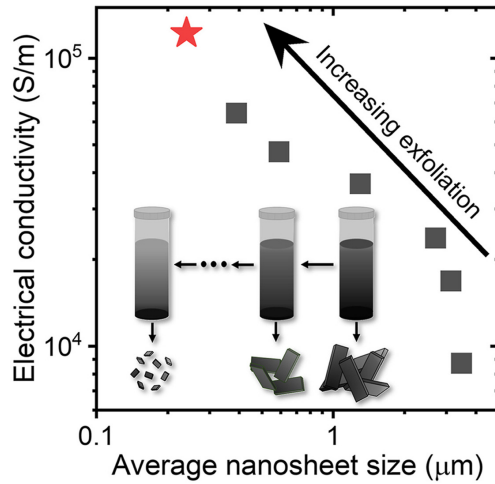


Figure 1.4: Electrical conductivity versus graphene nanosheet lateral size for graphene produced by LPE. Reproduced from [19].

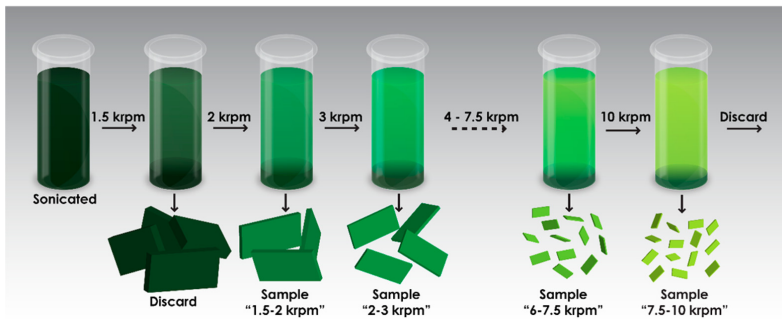


Figure 1.5: Schematic description of liquid cascade centrifugation process. Reproduced from [11].

size of the graphene nanosheets decreases, as shown in figure 1.4 [19]. In general, rather monodisperse dispersions containing nanosheets with specific lateral size and thickness (i.e. number of layers) are needed for different applications, with the size depending on the application. Thus, the nanosheets produced from LPE need to be fractionated.

A widely used procedure to fractionate nanosheets is the liquid cascade centrifugation (LCC) [11, 19, 23, 24]. The process of LCC is sketched in figure 1.5. In LCC, the sedimented layer is removed from the supernatant after being centrifuged for a specified time at a certain g -force in one step, then the supernatant is centrifuged again; the process is then repeated. The average size of the sedimented layer decreases as more steps of centrifugation are carried out. Apart from nanosheets, centrifugation

is also broadly used for the fractionation of nanoparticles with other shapes [25–27]. Despite its wide use, there is currently no theoretical guidelines for LCC. The operating conditions (e.g. g-force, centrifugation time, number of steps) are completely determined by trial and error. Thus, the outcome of LCC is very difficult to predict and the procedure is hard to optimize.

Centrifugation is essentially a sedimentation process. The principle of centrifugation for particle fractionation is the differential settling (i.e. for particles with the same density, larger ones settle faster and smaller ones settle slower). To model centrifugation, it is important to know the average settling velocity of certain particle class at the given condition (e.g. g-force, concentration, etc). While, this turns out to be difficult due to the long-range hydrodynamic interactions between particles.

Based on the Stokes drag law, the settling velocity of a spherical particle with radius a and density ρ_p in a centrifugal field with equivalent g-force g_e is

$$u^s = \frac{2(\rho_p - \rho_f)g_e a^2}{9\mu}, \quad (1.1)$$

where ρ_f and μ are fluid density and viscosity, respectively. The particle Reynolds number during centrifugation is

$$Re_p = \frac{\rho_f u^s a}{\mu}. \quad (1.2)$$

The Peclet number is

$$Pe = \frac{a u^s}{D}, \quad (1.3)$$

where D is the diffusion coefficient.

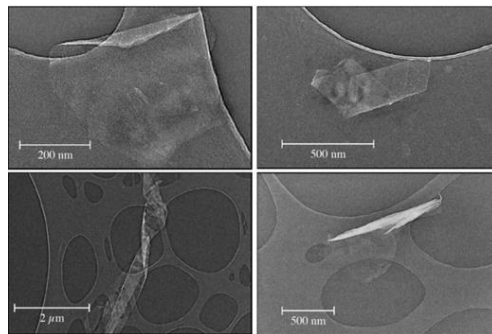
Take $\rho_p = 2500 \text{ kg/m}^3$ (e.g. the density of graphene), $a = 1 \text{ }\mu\text{m}$, and water as the fluid, values of the typical parameters in centrifugation are listed in table 1.1. It is seen that the centrifugation happens in Stokes flow regime and translational Brownian motion can be neglected because of the large centrifugal force.

1.1.4 Flexibility influences the shapes of nanosheets in flows

2D nanosheets have large Young's moduli and low bending rigidities [1, 29], which makes them nearly inextensible but highly flexible. During the liquid processing of these nanosheets, they can be highly deformed because of the energetic shear mixing. For example, fig.1.6 shows that after LPE, some of the graphene nanosheets are folded. It is important to understand and control how these nanosheets are deformed in the flow because the material properties (e.g. electron mobility) highly depend on the

Table 1.1: Values of typical parameters in centrifugation [11, 19, 23, 24].

Parameter	Value
Concentration	10 – 100 mg/mL
Volume fraction	0.004 – 0.04
Equivalent g-force	100g – 10000g
Settling velocity	0.33 – 33 mm/s
Reynolds number	$3.3 \times 10^{-4} - 3.3 \times 10^{-2}$
Peclet number	$1.5 \times 10^3 - 1.5 \times 10^5$

**Figure 1.6:** Transmission electron microscopy images of deformed graphene nanosheets after liquid phase exfoliation. Reproduced from [28].

nanosheet morphology [30], and certain shapes of the nanosheets are required in some applications (e.g. soft robotics and wearable sensing) [31].

Because the fluid-structure interaction happens at the micro-scale, currently there is no experiment which observes the deformation dynamics of a single nanosheet in the flow. Apart from understanding how a single sheet deforms in the flow, it is also very practical to understand how the inter-particle interactions alter the deformation of the nanosheets in the flow, as they tend to stack in the dispersion and the hydrodynamic interaction is long-ranged in Stokes flow.

1.2 Motivation

This thesis is particularly motivated by the fluid dynamics problems encountered during the liquid processing of 2D material nanosheets, where either polydispersity or flexibility of the nanosheets is the core of the problem. However, the findings in this thesis can also be generalized for other multiphase flow systems involving poly-disperse or flexible particles, as described in the following.

Particles suspended in flowing fluids are ubiquitous in both natural and industrial applications, and play an important role in various processes. In nature, particles are involved in phenomena like the formation of clouds, transport of sediment, etc. In industry, they are critical in fields like pharmaceuticals, food production, and material science, where they influence the product properties, stability, and performance. Understanding the behavior of particles, particularly their sorting and transport, is key to optimizing processes and developing advanced technologies in both environmental and engineering contexts.

Due to the variability in the processes generating the particles (e.g. grinding, crystallization, milling) and the stochastic nature of the natural forces exerted on the particles (e.g. erosion, weathering, biological activities), particulate systems are typically polydisperse with wide size distributions or consisting multiple components. For instance, figure 1.7 shows several examples of polydisperse particle systems at different length scales. These polydisperse particle systems usually need to be sorted by size (also referred to as size fractionation) or by other properties to acquire desired size ranges, shapes, or compositions, depending on the specific application. For example, in pharmaceutical applications, the size of the drug particle crucially influences its bioavailability in the patient's body and the efficacy of its delivery, as smaller particles are easier to be dissolved and overcome biological barriers [32, 33]. By controlling the sizes of drug-loaded nanoparticles, it is possible to achieve precision therapeutics [34]. In material science, the mechanical properties, thermal and electrical conductivities of composite materials depend crucially on the shape and size distributions of the filler particles [35–37]. Moreover, re-usable materials can be recycled via the fractionation of particulate wastes, for instance in the recycling of battery materials [38] and plastics [39], contributing to a circular economy and sustainable future. Popular fractionation techniques include sieving, sedimentation and centrifugation, froth flotation, magnetic separation, filtration, etc. Understanding and optimizing these processes will lead to higher purity of the fractionated samples and better designs of products which can be more efficiently recycled. This thesis aims to establish fluid dynamics fundamentals of sedimentation or centrifugation for the sorting by size.

Another property of particles which enriches their dynamics and promotes their applications is their flexibility. Flexible particles can deform under external forces like compression or shear forces which can be produced by non-uniform flows. Several examples of flexible particles are shown in figure 1.8. The ability of flexible particles to adapt to different environments and conditions is utilized in various applications. For instance, biological cells such as red blood cells are highly flexible, enabling them to pass through narrow capillaries without rupturing [41]. Soft hydrogels are biocompatible and responsive to external stimuli like temperature and pH, making them suitable for drug delivery and tissue engineering [42]. Microorganisms rely on the interaction between their flexible flagella and the surrounding fluid to swim [43]. In

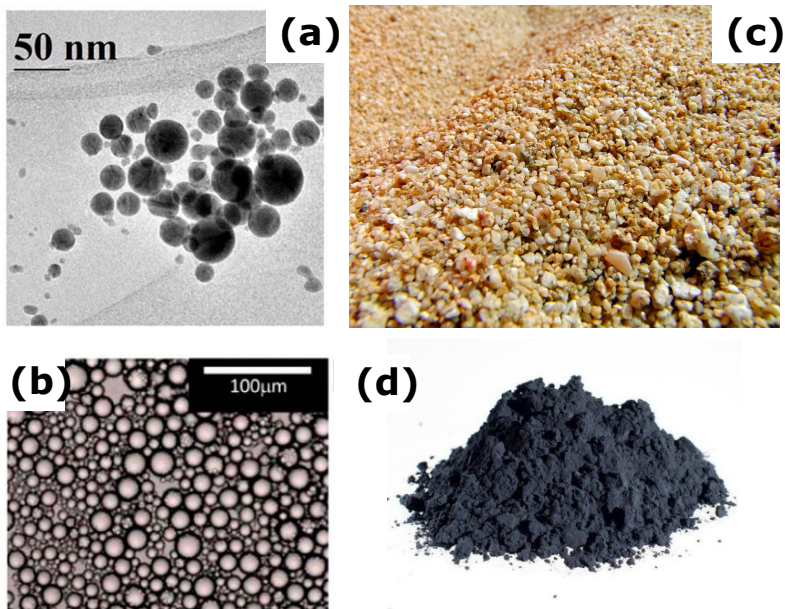


Figure 1.7: Examples of polydisperse particles: (a) transmission electron microscopy image of gold nanoparticles (reproduced from [25]); (b) optical microscope image of a polydisperse emulsion (reproduced from [40]); (c) sand grains with varying sizes (source: pixabay.com); (d) black mass a mixture of anode and cathode particles; the black mass is the main output of shredding of spent Li-ion batteries (source: elcanindustries.com).

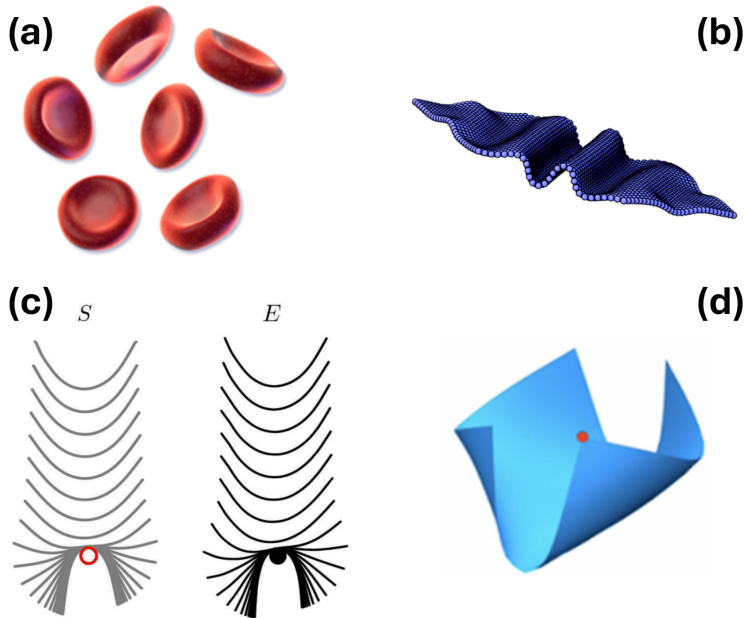


Figure 1.8: Examples of flexible particles: (a) red blood cells (source: en.wikipedia.org); (b) a buckled flexible hexagonal sheet in a simple shear flow (reproduced from [44]); (c) sedimenting flexible fibers interacting with an obstacle in a viscous liquid (reproduced from [45]); (d) a folded flexible rectangular sheet during sedimenting in a viscous liquid (reproduced from [46]).

these applications, it is essential to understand how flexible particles react to external stimuli, e.g. how they deform under external forces or when immersed in fluid flows. This thesis focuses on flexible particles immersed in fluid flows.

1.3 Thesis objectives and outline

Objectives

The goal of this thesis is to study the fluid dynamics of graphene in liquids using numerical simulations. The objectives of this thesis are two: (1) understanding the sedimentation of polydisperse suspensions in the Stokes regime, and (2) investigating the deformation dynamics of flexible sheets in shear flow, still under condition of low Reynolds numbers. The first objective contributes to the rational design of liquid cascade centrifugation procedure, and the second one contributes to the control of the morphologies of nanosheets in liquids. These objectives are addressed through numerical simulations carried out with a Stokesian dynamics method and a simplified

boundary integral method, and through the theoretical analysis of experiments carried out by collaborators. The numerical methods adopted and theoretical analysis done in this thesis are based on the theories of microhydrodynamics, and some fundamentals of microhydrodynamics are provided in chapter 2 to make the thesis self-contained thus. For the first objective, we want to understand:

- What are the optimal parameters to obtain a relatively monodisperse suspension starting from a polydisperse suspension through a liquid cascade centrifugation process? (chapter 3)

To answer this question, we theoretically analyze the centrifugation of a polydisperse suspension using a one-dimensional sedimentation model. In this model, we neglect the hydrodynamic interactions between particles and assume each size class settles with the corresponding Stokes velocity, aiming at extremely dilute suspensions.

- How to predict the average settling velocity of each size class in a dilute settling polydisperse suspension? (chapter 4)

To model the sedimentation of a polydisperse suspension, it is crucial to accurately predict the settling velocity of each size class. Towards this goal, we carried out discrete particle simulations using Stokesian dynamics to quantify the settling velocity statistics in polydisperse suspensions with broad size distributions. We also compare our results with predictions of existing hindered settling function models. Here, we study the sedimentation of spheres although the work is motivated by centrifugation of nanosheets. The reason is that we consider dilute systems and since the particles are far from each other, the hydrodynamic interaction has weak dependence on the particle shape and they can be treated approximately as point forces at the first order. Sedimentation of bidisperse suspensions and polydisperse suspensions with small polydispersities has been studied in the literature, but there is no study of polydisperse suspensions with wide continuous size distributions where the velocity of each size class is characterized, as pointed out in chapter 4.

- What are the implications of the widely used experimental procedure based on pipetting a suspension drop in a vertical tank to measure the single particle Stokes velocity? (chapter 5)

To quantify the hindered settling function from the experiments, it is important to accurately measure the single particle Stokes velocity. We collaborate with researchers from Deltares to show the limitations of this widely used experimental procedure (i.e. pipetting a suspension drop in a vertical tank to measure the single particle Stokes velocity) using both experiments and simulations.

For the first objective, dynamics of dilute suspensions of polydisperse spheres is studied. Since the suspension is dilute, the particles are far from each other and the hydrodynamic interactions have weak dependence on the particle shape. While for the second objective, we want to study the deformation of a pair of closely positioned flexible particles at the particle scale. To mimic the situation of nanosheets immersed in liquids, we use thin sheets with sizes of centi-meters immersed in glycerol in the experiments so that three-dimensional and time-dependent dynamics of the sheets can be measured and the local flow around the sheets is in the Stokes regime. Specifically, for the second objective, we want to understand:

- What is the threshold above which a flexible sheet will deform in the shear flow? (chapter 6)
- How does this threshold change due to hydrodynamic interactions in the shear flow? (chapter 6)

We address these questions by the combination of experiments and simulations. Experiments are done using Mylar sheets in a shear cell. Simulations are carried out using a simplified boundary integral method.

Outline

The remainder of this thesis is structured as follows. In chapter 2 some fundamentals of microhydrodynamics related to this thesis and the numerical methods used in this thesis are introduced. Chapter 3 presents a theoretical analysis and optimization of the liquid cascade centrifugation. Chapter 4 investigates the hindered settling of log-normally distributed Stokesian suspensions. Chapter 5 presents an analysis of the hydrodynamic interactions which lead to the particle settling velocity enhancement. Chapter 6 investigates the deformation of flexible sheets in the shear flow. Main conclusions of this thesis are summarized and recommendations of future research directions are presented in chapter 7.

REFERENCES

- [1] Konstantin S Novoselov, L Colombo, PR Gellert, MG Schwab, K Kim, et al. “A roadmap for graphene.” In: *Nature* 490.7419 (2012), pp. 192–200.
- [2] Terrance Barkan. “Graphene: the hype versus commercial reality.” In: *Nature Nanotechnology* 14.10 (2019), pp. 904–906.
- [3] Wei Kong, Hyun Kum, Sang-Hoon Bae, Jaewoo Shim, Hyunseok Kim, Ling-ping Kong, Yuan Meng, Kejia Wang, Chansoo Kim, and Jeehwan Kim. “Path towards graphene commercialization from lab to market.” In: *Nature Nanotechnology* 14.10 (2019), pp. 927–938.
- [4] Keith R Paton, Eswaraiah Varrla, Claudia Backes, Ronan J Smith, Umar Khan, Arlene O’Neill, Conor Boland, Mustafa Lotya, Oana M Istrate, Paul King, et al. “Scalable production of large quantities of defect-free few-layer graphene by shear exfoliation in liquids.” In: *Nature Materials* 13.6 (2014), pp. 624–630.
- [5] Simon Gravelle, Catherine Kamal, and Lorenzo Botto. “Liquid exfoliation of multilayer graphene in sheared solvents: A molecular dynamics investigation.” In: *The Journal of Chemical Physics* 152.10 (2020), p. 104701.
- [6] Giulia Salussolia, Ettore Barbieri, Nicola Maria Pugno, and Lorenzo Botto. “Micromechanics of liquid-phase exfoliation of a layered 2D material: a hydrodynamic peeling model.” In: *Journal of the Mechanics and Physics of Solids* 134 (2020), p. 103764.
- [7] Adyant Agrawal, Simon Gravelle, Catherine Kamal, and Lorenzo Botto. “Viscous peeling of a nanosheet.” In: *Soft Matter* (2022).
- [8] Catherine Kamal, Simon Gravelle, and Lorenzo Botto. “Hydrodynamic slip can align thin nanoplatelets in shear flow.” In: *Nature Communications* 11.1 (2020), pp. 1–10.
- [9] Edmund Han, Jaehyung Yu, Emil Annevelink, Jangyup Son, Dongyun A Kang, Kenji Watanabe, Takashi Taniguchi, Elif Ertekin, Pinshane Y Huang, and Arend M van der Zande. “Ultrasoft slip-mediated bending in few-layer graphene.” In: *Nature Materials* 19.3 (2020), pp. 305–309.
- [10] Thales FD Fernandes, Douglas R Miquita, Eder M Soares, Adelina P Santos, Luiz G Cançado, and Bernardo RA Neves. “A semi-automated general statistical treatment of graphene systems.” In: *2D Materials* 7.2 (2020), p. 025045.

- [11] Claudia Backes, Beata M Szydłowska, Andrew Harvey, Shengjun Yuan, Victor Vega-Mayoral, Ben R Davies, Pei-liang Zhao, Damien Hanlon, Elton JG Santos, Mikhail I Katsnelson, et al. “Production of highly monolayer enriched dispersions of liquid-exfoliated nanosheets by liquid cascade centrifugation.” In: *ACS Nano* 10.1 (2016), pp. 1589–1601.
- [12] Kazufumi Hosoda, Tomoaki Matsuura, Hiroaki Suzuki, and Tetsuya Yomo. “Origin of lognormal-like distributions with a common width in a growth and division process.” In: *Physical Review E* 83.3 (2011), p. 031118.
- [13] Ariel Amir. “Cell size regulation in bacteria.” In: *Physical Review Letters* 112.20 (2014), p. 208102.
- [14] Otto G Raabe. “Particle size analysis utilizing grouped data and the log-normal distribution.” In: *Journal of Aerosol Science* 2.3 (1971), pp. 289–303.
- [15] K Von Salzen. “Piecewise log-normal approximation of size distributions for aerosol modelling.” In: *Atmospheric Chemistry and Physics* 6.5 (2006), pp. 1351–1372.
- [16] Denis Bouyer, Alain Liné, and Zdravka Do-Quang. “Experimental analysis of floc size distribution under different hydrodynamics in a mixing tank.” In: *AIChE Journal* 50.9 (2004), pp. 2064–2081.
- [17] Kunpeng Zhao, Bernhard Vowinckel, T-J Hsu, Thomas Köllner, Bofeng Bai, and Eckart Meiburg. “An efficient cellular flow model for cohesive particle flocculation in turbulence.” In: *Journal of Fluid Mechanics* 889 (2020).
- [18] Kunpeng Zhao, Florian Pomes, Bernhard Vowinckel, T-J Hsu, Bofeng Bai, and Eckart Meiburg. “Flocculation of suspended cohesive particles in homogeneous isotropic turbulence.” In: *Journal of Fluid Mechanics* 921 (2021).
- [19] Keiran Clifford, Sean P Ogilvie, Aline Amorim Graf, Hannah J Wood, Anne C Sehnal, Jonathan P Salvage, Peter J Lynch, Matthew J Large, and Alan B Dalton. “Emergent high conductivity in size-selected graphene networks.” In: *Carbon* 218 (2024), p. 118642.
- [20] Peter May, Umar Khan, Arlene O’Neill, and Jonathan N Coleman. “Approaching the theoretical limit for reinforcing polymers with graphene.” In: *Journal of Materials Chemistry* 22.4 (2012), pp. 1278–1282.
- [21] Thomas F Jaramillo, Kristina P Jørgensen, Jacob Bonde, Jane H Nielsen, Sebastian Horch, and Ib Chorkendorff. “Identification of active edge sites for electrochemical H₂ evolution from MoS₂ nanocatalysts.” In: *Science* 317.5834 (2007), pp. 100–102.
- [22] Felice Torrìsi and Jonathan N Coleman. “Electrifying inks with 2D materials.” In: *Nature Nanotechnology* 9.10 (2014), pp. 738–739.

- [23] Umar Khan, Arlene O'Neill, Harshit Porwal, Peter May, Khalid Nawaz, and Jonathan N Coleman. "Size selection of dispersed, exfoliated graphene flakes by controlled centrifugation." In: *Carbon* 50.2 (2012), pp. 470–475.
- [24] Sean P Ogilvie, Matthew J Large, Marcus A O'Mara, Peter J Lynch, Cheuk Long Lee, Alice AK King, Claudia Backes, and Alan B Dalton. "Size selection of liquid-exfoliated 2D nanosheets." In: *2D Materials* 6.3 (2019), p. 031002.
- [25] Francesco Bonaccorso, Mirco Zerbetto, Andrea C Ferrari, and Vincenzo Amendola. "Sorting nanoparticles by centrifugal fields in clean media." In: *The Journal of Physical Chemistry C* 117.25 (2013), pp. 13217–13229.
- [26] Jeffrey A Fagan, Matthew L Becker, Jaehun Chun, Pingting Nie, Barry J Bauer, Jeffrey R Simpson, Angela Hight-Walker, and Erik K Hobbie. "Centrifugal length separation of carbon nanotubes." In: *Langmuir* 24.24 (2008), pp. 13880–13889.
- [27] Ruimin Wang, Yinglu Ji, Xiaochun Wu, Renxiao Liu, Lan Chen, and Guanglu Ge. "Experimental determination and analysis of gold nanorod settlement by differential centrifugal sedimentation." In: *RSC Advances* 6.49 (2016), pp. 43496–43500.
- [28] G Salussolia, C Kamal, Jason Stafford, N Pugno, and L Botto. "Simulation of interacting elastic sheets in shear flow: Insights into buckling, sliding, and reassembly of graphene nanosheets in sheared liquids." In: *Physics of Fluids* 34.5 (2022).
- [29] Niklas Lindahl, Daniel Midtvedt, Johannes Svensson, Oleg A Nerushev, Niclas Lindvall, Andreas Isacson, and Eleanor EB Campbell. "Determination of the bending rigidity of graphene via electrostatic actuation of buckled membranes." In: *Nano Letters* 12.7 (2012), pp. 3526–3531.
- [30] Fanyan Zeng, Yafei Kuang, Gaoqin Liu, Rui Liu, Zhongyuan Huang, Chaopeng Fu, and Haihui Zhou. "Supercapacitors based on high-quality graphene scrolls." In: *Nanoscale* 4.13 (2012), pp. 3997–4001.
- [31] Gyeong Min Choi, Minji Park, Yul Hui Shim, So Youn Kim, and Heon Sang Lee. "Mass production of 2D manifolds of graphene oxide by shear flow." In: *Advanced Functional Materials* 32.1 (2022), p. 2107694.
- [32] Marie Gaumet, Angelica Vargas, Robert Gurny, and Florence Delie. "Nanoparticles for drug delivery: the need for precision in reporting particle size parameters." In: *European Journal of Pharmaceutics and Biopharmaceutics* 69.1 (2008), pp. 1–9.
- [33] Zi Hong Mok. "The effect of particle size on drug bioavailability in various parts of the body." In: *Pharmaceutical Science Advances* (2024), p. 100031.

- [34] Michael J Mitchell, Margaret M Billingsley, Rebecca M Haley, Marissa E Wechsler, Nicholas A Peppas, and Robert Langer. “Engineering precision nanoparticles for drug delivery.” In: *Nature Reviews Drug Discovery* 20.2 (2021), pp. 101–124.
- [35] Maryam Majidian, Claudio Grimaldi, László Forró, and Arnaud Magrez. “Role of the particle size polydispersity in the electrical conductivity of carbon nanotube-epoxy composites.” In: *Scientific Reports* 7.1 (2017), p. 12553.
- [36] Fathie Kundie, Che Husna Azhari, Andanastuti Muchtar, and Zainal Arifin Ahmad. “Effects of filler size on the mechanical properties of polymer-filled dental composites: A review of recent developments.” In: *Journal of Physical Science* 29.1 (2018), pp. 141–165.
- [37] Ich Long Ngo, Chan Byon, and Byeong Jun Lee. “Numerical analysis for the effects of particle distribution and particle size on effective thermal conductivity of hybrid-filler polymer composites.” In: *International Journal of Thermal Sciences* 142 (2019), pp. 42–53.
- [38] Roberto Sommerville, James Shaw-Stewart, Vannessa Goodship, Neil Rowson, and Emma Kendrick. “A review of physical processes used in the safe recycling of lithium ion batteries.” In: *Sustainable Materials and Technologies* 25 (2020), e00197.
- [39] Kim Ragaert, Laurens Delva, and Kevin Van Geem. “Mechanical and chemical recycling of solid plastic waste.” In: *Waste Management* 69 (2017), pp. 24–58.
- [40] Armando Maestro, Wiebke Drenckhan, Emmanuelle Rio, and Reinhard Höhler. “Liquid dispersions under gravity: volume fraction profile and osmotic pressure.” In: *Soft Matter* 9.8 (2013), pp. 2531–2540.
- [41] R Skalak and PI Brånemark. “Deformation of red blood cells in capillaries.” In: *Science* 164.3880 (1969), pp. 717–719.
- [42] Y Lee, WJ Song, and J-Y Sun. “Hydrogel soft robotics.” In: *Materials Today Physics* 15 (2020), p. 100258.
- [43] Julia M Yeomans, Dmitri O Pushkin, and Henry Shum. “An introduction to the hydrodynamics of swimming microorganisms.” In: *The European Physical Journal Special Topics* 223.9 (2014), pp. 1771–1785.
- [44] Kevin S Silmore, Michael S Strano, and James W Swan. “Buckling, crumpling, and tumbling of semiflexible sheets in simple shear flow.” In: *Soft Matter* 17.18 (2021), pp. 4707–4718.
- [45] Ursy Makanga, Mohammadreza Sepahi, Camille Duprat, and Blaise Delmotte. “Obstacle-induced lateral dispersion and nontrivial trapping of flexible fibers settling in a viscous fluid.” In: *Physical Review Fluids* 8.4 (2023), p. 044303.

- [46] Yijiang Yu and Michael D Graham. “Free-space and near-wall dynamics of a flexible sheet sedimenting in Stokes flow.” In: *Physical Review Fluids* 9.5 (2024), p. 054104.

2

FUNDAMENTALS OF MICROHYDRODYNAMICS

Microhydrodynamics describes the particle dynamics in Stokes flow, which covers the topics studied in this thesis. In this chapter, a brief overview of some fundamentals of microhydrodynamics is provided, which lays the foundation of the analysis in the following chapters. The numerical methods used in this thesis including boundary integral method and Stokesian dynamics method are introduced at the end of this chapter.

2.1 Introduction

Microhydrodynamics is a subject which covers the studies of the motions of small objects whose sizes are typically at nano- or micro-meter scales in viscous fluids. For example, sedimentation and rheological properties of colloidal suspensions, swimming of microorganisms like bacteria and algae, and diffusion of macromolecules are its research topics, to name a few. This chapter provides a brief overview of some fundamentals of microhydrodynamics as a foundation for the following chapters. More complete descriptions of theories of microhydrodynamics are referred to the relevant books [1, 2].

Governing equations

Since the flow around the particles happens at a small length scale, the Reynolds number is typically small, and the flow can be described by the Stokes equations:

$$\nabla \cdot \mathbf{u} = 0, \quad (2.1)$$

$$-\nabla p + \mu \nabla^2 \mathbf{u} + \mathbf{f} = \mathbf{0}, \quad (2.2)$$

where \mathbf{u} and p are the velocity and pressure of the flow, respectively, μ is the viscosity, and \mathbf{f} is the force per unit volume on the fluid.

At these microscales, inertia of particles can be neglected. Their motions are governed by the following force balance equation:

$$\mathbf{F}^h + \mathbf{F}^e = \mathbf{0}, \quad (2.3)$$

where \mathbf{F}^h and \mathbf{F}^e are the hydrodynamic and external forces on the particle.

2.2 Point force and other singularities

The primary singularity in Stokes flow is the Stokeslet which describes the flow induced by a point force in an unbounded domain. When $\mathbf{f} = \mathbf{F}\delta(\mathbf{r})$ in equation 2.2, the solutions of the velocity and pressure fields are:

$$\mathbf{u}(\mathbf{r}) = \mathbf{G}(\mathbf{r}) \cdot \mathbf{F} = \left(\frac{\mathbf{I}}{8\pi\mu r} + \frac{\mathbf{r}\mathbf{r}}{8\pi\mu r^3} \right) \cdot \mathbf{F}, \quad (2.4)$$

$$p(\mathbf{r}) = \left(\frac{\mathbf{r}}{4\pi r^3} \right) \cdot \mathbf{F}, \quad (2.5)$$

where \mathbf{F} is the vector of the point force, $\delta(\mathbf{r})$ is the Dirac delta function, $r = |\mathbf{r}|$ is the distance from the point force, and \mathbf{I} is the unity tensor. In equation 2.4, $\mathbf{G}(\mathbf{r})$ is called the Oseen-Burgers tensor representing how the flow decays away from the point force. Note that the flow diverges at the location of the point force ($r = 0$).

To avoid the divergence from the Stokeslet solutions which is problematic in numerical analysis, Cortez [3] proposed the method of regularized Stokeslets. In this method, the point force is smeared over a small blob so that the resulting flow is finite everywhere. The smear of the point force is done by replacing the Dirac delta function with a blob or cutoff function $\phi_\epsilon(\mathbf{r})$ which is radially symmetric and satisfies $\int \phi_\epsilon(\mathbf{r}) d\mathbf{r} = 1$. One of such blob functions is:

$$\phi_\epsilon(\mathbf{r}) = \frac{15\epsilon^4}{8\pi(r^2 + \epsilon^2)^{7/2}}, \quad (2.6)$$

where ϵ is a regularization parameter controlling the spread of the blob function. For $\epsilon \rightarrow 0$, $\phi_\epsilon(\mathbf{r}) \rightarrow \delta(\mathbf{r})$. The flow of this regularized Stokeslet is:

$$\mathbf{u}_\epsilon(\mathbf{r}) = \mathbf{G}_\epsilon(\mathbf{r}) \cdot \mathbf{F} = \left(\frac{\mathbf{I}(r^2 + 2\epsilon^2)}{8\pi\mu(r^2 + \epsilon^2)^{3/2}} + \frac{\mathbf{r}\mathbf{r}}{8\pi\mu(r^2 + \epsilon^2)^{3/2}} \right) \cdot \mathbf{F}, \quad (2.7)$$

$$p_\epsilon(\mathbf{r}) = \left(\frac{\mathbf{r}}{4\pi(r^2 + \epsilon^2)^{3/2}} \right) \cdot \mathbf{F}, \quad (2.8)$$

where $\mathbf{G}_\epsilon(\mathbf{r})$ is the regularized green's function. Examples of the streamlines of a Stokeslet and a regularized Stokeslet are shown in figure 2.1. The streamlines are more smooth at the point force location (i.e. the origin) in the regularized Stokeslet case than those in the Stokeslet case. The idea of spreading a point force over a small region is also used in the force coupling method [4] for simulations of low Reynolds number suspensions.

Since the Stokes equations are linear, other singularity solutions can be derived by differentiating the solution of the Stokeslet. For example, flows caused by force dipoles, quadrupoles and other higher-order force multipoles. A force dipole can be decomposed into a symmetric part named as a stresslet and an antisymmetric part named as a rotlet. A stresslet induces a pure straining flow and a rotlet induces a rotation flow. These singularity solutions can be superposed to construct the solutions of different kinds of Stokes flow problems, which is the principle of the singularity method [5]. The accuracy of this method depends on the choices of the types and the positions of the singularities. The densities of the singularities can be determined by satisfying the boundary conditions. This method has been applied to develop the slender-body theory [6], calculate the flow fields of moving bodies in Stokes flows [5], and model swimmers in fluids [7, 8], for example.

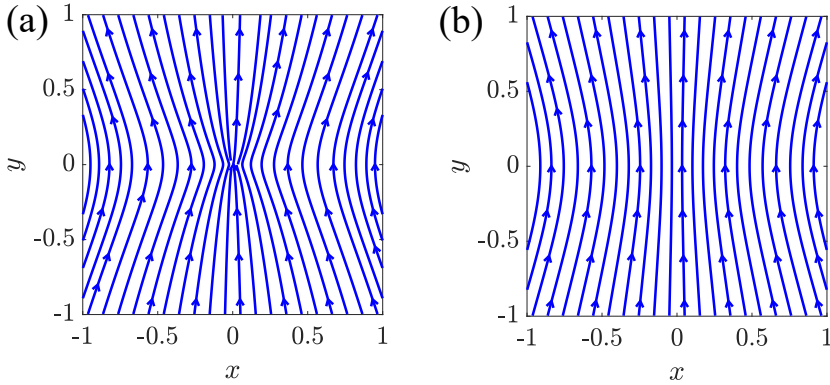


Figure 2.1: Streamlines of (a) a Stokeslet and (b) a regularized Stokeslet with $\epsilon = 0.5$ for a point force as $\mathbf{F} = (0, 1, 0)$.

2.3 Integral representation and multipole expansion

For a rigid particle immersed in a Stokes flow, the disturbance flow induced by this particle can be expressed as:

$$\mathbf{u}(\mathbf{x}) - \mathbf{u}^\infty(\mathbf{x}) = \int_{S_p} \mathbf{G}(\mathbf{x} - \mathbf{y}) \cdot (-\boldsymbol{\sigma} \cdot \mathbf{n})(\mathbf{y}) dS(\mathbf{y}), \quad (2.9)$$

where \mathbf{u}^∞ is the background flow without the particle, \mathbf{x} is a position in the flow, \mathbf{y} is a position on the particle surface S_p , \mathbf{G} is the Oseen-Burgers tensor, $\boldsymbol{\sigma} = -p\mathbf{I} + \mu(\nabla\mathbf{u} + \nabla\mathbf{u}^T)$ is the stress tensor of the fluid, and \mathbf{n} is the outward unit normal vector on the particle surface. This integral representation means that the disturbance flow of a rigid particle is the superposition of flows induced by a collection of point forces distributed over the particle surface with density $-\boldsymbol{\sigma} \cdot \mathbf{n} dS$.

The integral in equation 2.9 is called the single layer potential. It requires the surface force distribution to be known to calculate the velocity field. For deformable particles, there is another integral needed in the integral representation of the flow field, which is called the double layer potential. It requires the surface velocity distribution. When the condition that $\int_{S_p} \mathbf{u}(\mathbf{y}) \cdot \mathbf{n}(\mathbf{y}) dS = 0$ is met, the double layer potential can be neglected. This condition holds for rigid particles, flexible yet inextensible particles with conserved volumes [9], etc. For particles with surface slip velocities, the double layer potential cannot be neglected [10, 11].

The integral representation (equation 2.9) can be expanded with respect to the center of the particle \mathbf{x}_c , which is:

$$\begin{aligned} \mathbf{u}(\mathbf{x}) - \mathbf{u}^\infty(\mathbf{x}) &= \mathbf{G}(\mathbf{x} - \mathbf{x}_c) \cdot \int_{S_p} (-\boldsymbol{\sigma} \cdot \mathbf{n})(\mathbf{y}) dS(\mathbf{y}) \\ &+ \nabla_{\mathbf{y}} \mathbf{G}(\mathbf{x} - \mathbf{y})|_{\mathbf{y}=\mathbf{x}_c} \cdot \int_{S_p} (\mathbf{y} - \mathbf{x}_c)(-\boldsymbol{\sigma} \cdot \mathbf{n})(\mathbf{y}) dS(\mathbf{y}) + \dots \quad (2.10) \\ &= -\mathbf{G}(\mathbf{x} - \mathbf{x}_c) \cdot \mathbf{F} - \nabla_{\mathbf{y}} \mathbf{G}(\mathbf{x} - \mathbf{y})|_{\mathbf{y}=\mathbf{x}_c} \cdot \mathbf{M} + \dots, \end{aligned}$$

where \mathbf{F} is the force exerted on the particle by the fluid (i.e. monopole), and \mathbf{M} is the first moment of the force density on the particle surface (i.e. dipole). Other higher-order force multipoles are omitted here. From equation 2.10, it is also seen that the higher the order of the multipole, the faster the flow it induces decays. Thus more and more multipoles should be included when \mathbf{x} gets closer to the particle surface in equation 2.10. This multipole expansion can be used to approximate the flow field induced by a particle at different levels of accuracy.

2.4 Numerical methods

In this section, the two numerical methods used in this thesis for Stokes flow simulations (i.e. boundary integral method and Stokesian dynamics) are introduced.

Boundary integral method

The boundary integral method exploits the integral representation shown in equation 2.9. For a solid particle immersed in a Stokes flow, the surface of the particle can be discretized into small elements δS . Taking a point \mathbf{x}_i on the particle surface, equation 2.9 can be written as the following discretized form:

$$\mathbf{u}(\mathbf{x}_i) = \mathbf{u}^\infty(\mathbf{x}_i) - \sum_j \mathbf{G}(\mathbf{x}_i - \mathbf{x}_j) \cdot \boldsymbol{\sigma} \cdot \mathbf{n}(\mathbf{x}_j) \delta S_j, \quad (2.11)$$

where \mathbf{x}_j is the position of element δS_j on the particle surface. Here the surface force $\boldsymbol{\sigma} \cdot \mathbf{n}$ is assumed to be constant over each small element.

For a resistance problem where the velocity of the particle is known and the force on the particle needs to be calculated, the left hand side of equation 2.11 is known and the surface force on each element can be calculated. Then, the hydrodynamic force and torque on the particle can be calculated as:

$$\mathbf{F} = \sum_j \boldsymbol{\sigma} \cdot \mathbf{n}(\mathbf{x}_j) \delta S_j, \quad (2.12)$$

and

$$\mathbf{T} = \sum_j (\mathbf{x}_j - \mathbf{x}_c) \times (\boldsymbol{\sigma} \cdot \mathbf{n}(\mathbf{x}_j)) \delta S_j. \quad (2.13)$$

For a mobility problem where the force and torque on the particle are known and the velocity needs to be calculated, another set of equations of the kinematic constraints are needed, which are:

$$\mathbf{u}(\mathbf{x}_i) = \mathbf{U} + \boldsymbol{\omega} \times (\mathbf{x}_i - \mathbf{x}_c), \quad (2.14)$$

for a solid body motion with translational velocity \mathbf{U} and rotational velocity $\boldsymbol{\omega}$ of the particle. By coupling equations 2.11, 2.12, 2.13 and 2.14, the surface force of each element and the velocities of the particle can be calculated.

The advantage of boundary integral method over directly solving the Stokes equations using finite difference or finite volume methods is that only the boundary needs to be meshed instead of the whole domain being discretized, reducing the computation from a three dimensional problem to a two dimensional problem. Boundary integral method has been used for simulations of emulsions [12, 13], droplet interactions [14, 15], suspensions [16], dynamics of micro-swimmers [17, 18], fluid-structure interactions at micro-scales including capsules [19], red blood cells [20], and elastic sheets [21], etc.

Stokesian dynamics

Stokesian dynamics is a discrete particle simulation method to study the suspension dynamics in Stokes flow [22]. Each particle is represented by force multipoles as shown in equation 2.10. Usually only force, torque and stresslet are considered. The linear relation between the velocities of the particles and force multipoles of the particles is:

$$\begin{pmatrix} \mathbf{U} - \mathbf{U}^\infty \\ -\mathbf{E}^\infty \end{pmatrix} = \mathbf{M} \cdot \begin{pmatrix} \mathbf{F} \\ \mathbf{S} \end{pmatrix}, \quad (2.15)$$

where \mathbf{U} is the velocities (including translational and rotational) of all particles, \mathbf{U}^∞ is the velocities of the undisturbed flow at particle centers, \mathbf{E}^∞ is the strain rate of the flow, \mathbf{F} includes the forces and torques on the particles, \mathbf{S} is the stresslets of the particles, and \mathbf{M} is the grand mobility matrix representing the multi-body hydrodynamic interactions. This mobility matrix can be constructed using the Rotne-Prager-Yamakawa formula [23–26], which depends on the relative positions between particles and sizes of particles.

To include near-field lubrication between particles, the resistance formulation should be used, which is:

$$\begin{pmatrix} \mathbf{F} \\ \mathbf{S} \end{pmatrix} = \mathbf{R} \cdot \begin{pmatrix} \mathbf{U} - \mathbf{U}^\infty \\ -\mathbf{E}^\infty \end{pmatrix}, \quad (2.16)$$

where \mathbf{R} is the grand resistance matrix and is formulated as:

$$\mathbf{R} = \mathbf{M}^{-1} + \mathbf{R}_{2b} - \mathbf{R}_{2b}^\infty. \quad (2.17)$$

Here, \mathbf{R}_{2b} is constructed using the exact two-sphere resistance solutions [27, 28], and \mathbf{R}_{2b}^∞ composes of the inverse matrices of the two-sphere mobility matrices. From equation 2.17, it is seen that the grand resistance mobility matrix includes the far-field many-body hydrodynamic interactions (\mathbf{M}^{-1}) and the near-field lubrication ($\mathbf{R}_{2b} - \mathbf{R}_{2b}^\infty$).

More detailed descriptions of Stokesian dynamics can be found in the references [22, 29, 30]. Since its invention, faster versions of Stokesian dynamics have been proposed, like accelerated Stokesian dynamics [31] and fast Stokesian dynamics [32]. Brownian motion can also be easily incorporated into the framework of Stokesian dynamics to study colloidal suspensions [33]. Arbitrarily shaped particles such as macromolecules can also be studied using Stokesian dynamics by modelling the particle as a rigid composite of spherical beads [34].

REFERENCES

- [1] Elisabeth Guazzelli and Jeffrey F Morris. *A physical introduction to suspension dynamics*. Vol. 45. Cambridge University Press, 2011.
- [2] Sangtae Kim and Seppo J Karrila. *Microhydrodynamics: principles and selected applications*. Butterworth-Heinemann, 2013.
- [3] Ricardo Cortez. “The method of regularized Stokeslets.” In: *SIAM Journal on Scientific Computing* 23.4 (2001), pp. 1204–1225.
- [4] Sune Lomholt and Martin R Maxey. “Force-coupling method for particulate two-phase flow: Stokes flow.” In: *Journal of Computational Physics* 184.2 (2003), pp. 381–405.
- [5] Allen T Chwang and T Yao-Tsu Wu. “Hydromechanics of low-Reynolds-number flow. Part 2. Singularity method for Stokes flows.” In: *Journal of Fluid mechanics* 67.4 (1975), pp. 787–815.
- [6] George K Batchelor. “Slender-body theory for particles of arbitrary cross-section in Stokes flow.” In: *Journal of Fluid Mechanics* 44.3 (1970), pp. 419–440.
- [7] Saverio E Spagnolie and Eric Lauga. “Hydrodynamics of self-propulsion near a boundary: predictions and accuracy of far-field approximations.” In: *Journal of Fluid Mechanics* 700 (2012), pp. 105–147.
- [8] Alexander Chamolly and Eric Lauga. “Stokes flow due to point torques and sources in a spherical geometry.” In: *Physical Review Fluids* 5.7 (2020), p. 074202.
- [9] Thomas D Montenegro-Johnson, Lyndon Koens, and Eric Lauga. “Microscale flow dynamics of ribbons and sheets.” In: *Soft Matter* 13.3 (2017), pp. 546–553.
- [10] David J Smith, Meurig T Gallagher, Rudi Schuech, and Thomas D Montenegro-Johnson. “The role of the double-layer potential in regularised stokeslet models of self-propulsion.” In: *Fluids* 6.11 (2021), p. 411.
- [11] Catherine Kamal, Simon Gravelle, and Lorenzo Botto. “Effect of hydrodynamic slip on the rotational dynamics of a thin Brownian platelet in shear flow.” In: *Journal of Fluid Mechanics* 919 (2021), A1.
- [12] M Loewenberg and EJ Hinch. “Numerical simulation of a concentrated emulsion in shear flow.” In: *Journal of Fluid Mechanics* 321 (1996), pp. 395–419.

- [13] Jingtao Wang, Jinxia Liu, Junjie Han, and Jing Guan. “Rheology investigation of the globule of multiple emulsions with complex internal structures through a boundary element method.” In: *Chemical Engineering Science* 96 (2013), pp. 87–97.
- [14] Ivan B Bazhlekov, Patrick D Anderson, and Han EH Meijer. “Nonsingular boundary integral method for deformable drops in viscous flows.” In: *Physics of Fluids* 16.4 (2004), pp. 1064–1081.
- [15] MB Nemer, X Chen, DH Papadopoulos, J Bławdziewicz, and M Loewenberg. “Hindered and enhanced coalescence of drops in Stokes flows.” In: *Physical Review Letters* 92.11 (2004), p. 114501.
- [16] Yuanxun Bao, Manas Rachh, Eric E Keaveny, Leslie Greengard, and Aleksandar Donev. “A fluctuating boundary integral method for Brownian suspensions.” In: *Journal of Computational Physics* 374 (2018), pp. 1094–1119.
- [17] Bin Liu, Kenneth S Breuer, and Thomas R Powers. “Helical swimming in Stokes flow using a novel boundary-element method.” In: *Physics of Fluids* 25.6 (2013).
- [18] Kenta Ishimoto and Eamonn A Gaffney. “Boundary element methods for particles and microswimmers in a linear viscoelastic fluid.” In: *Journal of Fluid Mechanics* 831 (2017), pp. 228–251.
- [19] WR Dodson and P Dimitrakopoulos. “Dynamics of strain-hardening and strain-softening capsules in strong planar extensional flows via an interfacial spectral boundary element algorithm for elastic membranes.” In: *Journal of Fluid Mechanics* 641 (2009), pp. 263–296.
- [20] Hong Zhao, Amir HG Isfahani, Luke N Olson, and Jonathan B Freund. “A spectral boundary integral method for flowing blood cells.” In: *Journal of Computational Physics* 229.10 (2010), pp. 3726–3744.
- [21] Yijiang Yu and Michael D Graham. “Wrinkling and multiplicity in the dynamics of deformable sheets in uniaxial extensional flow.” In: *Physical Review Fluids* 7.2 (2022), p. 023601.
- [22] Louis Durlofsky, John F Brady, and Georges Bossis. “Dynamic simulation of hydrodynamically interacting particles.” In: *Journal of Fluid Mechanics* 180 (1987), pp. 21–49.
- [23] Jens Rotne and Stephen Prager. “Variational treatment of hydrodynamic interaction in polymers.” In: *The Journal of Chemical Physics* 50.11 (1969), pp. 4831–4837.

- [24] Hiromi Yamakawa. “Transport properties of polymer chains in dilute solution: hydrodynamic interaction.” In: *The Journal of Chemical Physics* 53.1 (1970), pp. 436–443.
- [25] Eligiusz Wajnryb, Krzysztof A Mizerski, Pawel J Zuk, and Piotr Szymczak. “Generalization of the Rotne–Prager–Yamakawa mobility and shear disturbance tensors.” In: *Journal of Fluid Mechanics* 731 (2013), R3.
- [26] Pawel J Zuk, E Wajnryb, KA Mizerski, and P Szymczak. “Rotne–Prager–Yamakawa approximation for different-sized particles in application to macromolecular bead models.” In: *Journal of Fluid Mechanics* 741 (2014), R5.
- [27] DJ Jeffrey and Y Onishi. “Calculation of the resistance and mobility functions for two unequal rigid spheres in low-Reynolds-number flow.” In: *Journal of Fluid Mechanics* 139 (1984), pp. 261–290.
- [28] Sangtae Kim and Richard T Mifflin. “The resistance and mobility functions of two equal spheres in low-Reynolds-number flow.” In: *The Physics of fluids* 28.7 (1985), pp. 2033–2045.
- [29] John F Brady, Ronald J Phillips, Julia C Lester, and Georges Bossis. “Dynamic simulation of hydrodynamically interacting suspensions.” In: *Journal of Fluid Mechanics* 195 (1988), pp. 257–280.
- [30] John F Brady, Georges Bossis, et al. “Stokesian dynamics.” In: *Annual Review of Fluid Mechanics* 20.1 (1988), pp. 111–157.
- [31] Asimina Sierou and John F Brady. “Accelerated Stokesian dynamics simulations.” In: *Journal of Fluid Mechanics* 448 (2001), pp. 115–146.
- [32] Andrew M Fiore and James W Swan. “Fast stokesian dynamics.” In: *Journal of Fluid Mechanics* 878 (2019), pp. 544–597.
- [33] Adolfo J Banchio and John F Brady. “Accelerated stokesian dynamics: Brownian motion.” In: *The Journal of Chemical Physics* 118.22 (2003), pp. 10323–10332.
- [34] James W Swan and Gang Wang. “Rapid calculation of hydrodynamic and transport properties in concentrated solutions of colloidal particles and macromolecules.” In: *Physics of Fluids* 28.1 (2016).

3

ANALYSIS AND OPTIMIZATION OF A MULTICASCADE METHOD

In this chapter, a one-dimensional model is used to study the multicascade centrifugation of polydisperse suspensions to isolate certain size range from an initial size distribution. Assuming the suspension to be very dilute, the settling velocity of each size class is calculated by using the corresponding Stokes velocity. An optimized procedure based on a trade-off between the yield and the amount of impurity desired is proposed. Practical applications of the theoretical analysis are demonstrated through the fractionation of spherical metallic nanoparticles and the fractionation of graphene.

This chapter is based on the article:

H. Li et al. "Analysis and optimization of a multicascade method for the size fractionation of poly-dispersed particle systems via sedimentation or centrifugation." In: (*To be submitted*), arXiv:2303.05257.

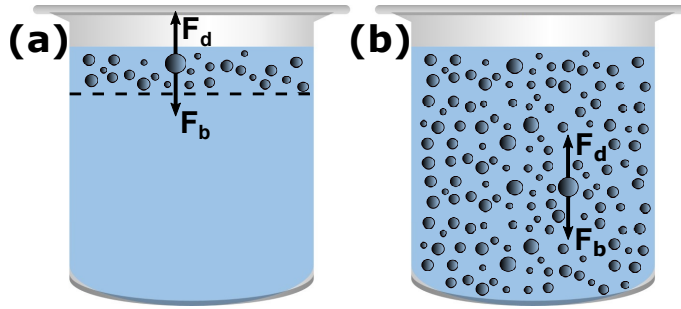


Figure 3.1: Sketches of settling particles under the balance of body force (F_b) and Stokes drag (F_d) in (a) band sedimentation and (b) homogeneous sedimentation.

3.1 Introduction

Dispersed liquid-solid and liquid-liquid systems are liquids containing suspended solid or liquid particles. Examples of such systems are cell broths, protein solutions, nanomaterial suspensions and emulsions [1, 2]. A very common technique to separate the dispersed and continuum phases in these systems is the application of a gravitational or centrifugal field. If the densities of the dispersed and continuous phases are different, the applied field will drive the translation of the dispersed phase with respect to the continuum phase, so that the dispersed phase can be removed from the fluid [3, 4]. Decanters, centrifuges, ultra-centrifuges and gravity settlers, are examples of separation units that work based on this method.

In addition to separate particulate materials from the liquid, sedimentation and centrifugation can also be used to fractionate particles in size classes, or to make the particle size distribution more monodisperse. This is a crucial outcome, as the performance of colloidal materials and nanomaterials is extremely dependent on particle size and obtaining particles with controlled polydispersity has practical and economical advantages. For example, the cost of many nanomaterials depends markedly on how monodispersed the sample is, and in fact for applications demanding high purity fractionation is necessarily applied to samples provided by suppliers. There are of course many methods for particle fractionation, for example field-flow fractionation [5], hydrodynamic chromatography [6] and filtration [7], but centrifugation and sedimentation are unique in their ability to handle large or coarse samples and are quick and easy to apply.

The method through which size fractionation can be obtained by sedimentation or centrifugation is a multistep method called, in the context of centrifugation, differential or multicascade centrifugation. The method consists in removing the sedimented layer from the supernatant after a specified centrifugation time, then the supernatant is centrifuged again. The process is then repeated several times until it is expected, based

on some criteria, that the fractionated sample contains only particles of a given size interval, and no others. The decision for the centrifugation parameters, for instance centrifugation time and speed, is typically based on trial and error, or following literature protocols that are often themselves based on empirical observations. The question that this paper would like to address is whether this choice can be made rationally based on a mathematical model that provides the particle size distributions in the supernatant and sedimented layer at any given time. This mathematical model will furnish also the amount of impurities. When deciding for example the centrifugation times to isolate a certain interval of the initial size distribution, one indeed must account for the fact that there is a link between the centrifugation time and the amount of impurities obtained. For example, for any choice of centrifugation time, some fine particles will sediment at the bottom of the centrifugation vial together with the coarser particles, so the pellet at the bottom will be a mixture of mainly coarse particles with a subset of small particles which we term impurities. Determining the amount of impurities requires information about the initial size distribution and the calculation of how this size distribution evolves in time in the supernatant and in the sedimented layer. The current paper analyses mathematically this evolution for two cases as sketched in Fig.3.1: homogeneous sedimentation, in which the particles are mixed throughout the vial [8, 9], and band sedimentation, in which the particles are initially deposited in a small slab at the top of the clear fluid [10–12]. We will see that band sedimentation holds significant promise for size fractionation. From a mathematical point of view, developing a centrifugation protocol is similar to developing an algorithm, i.e. a step-by-step sequence of instructions to obtain a certain quantifiable outcome. This paper lays the basis for a rational, step-by-step algorithm to size fractionate a dilute polydispersed suspension of particles for the case in which the initial size distribution is known. The idea is that, to isolate a certain interval of this size distribution, we can eliminate the tails of the probability distribution in successive steps (see Fig.3.2 for an illustration of the concept). In reality the “cut” will not be sharp, so it is important to quantify the amount of impurities (error) made in each step.

The main assumption of the paper is that the suspension is dilute. If the suspension is not dilute, the calculation of the time dependence of the particle size distribution can not be done exactly. Furthermore, the dilute case enables to establish a theoretical framework that is useful both for practical initial calculations and for further theoretical work. We further assume the initial particle size distribution follows a log-normal. This assumption is not very restrictive. Log-normal distributions are almost universal when the particle size distribution is the result of repetitive break-up processes [13] (for example, the size of the nanosheets produced by liquid-phase exfoliation follows a log-normal distribution [8, 10]). Log-normal distribution is also widely used to describe particle size because it fits well for the measured distributions of many types of particles [14] (e.g. aerosols [15], ultrafine metal particles [16], soil particles [17])

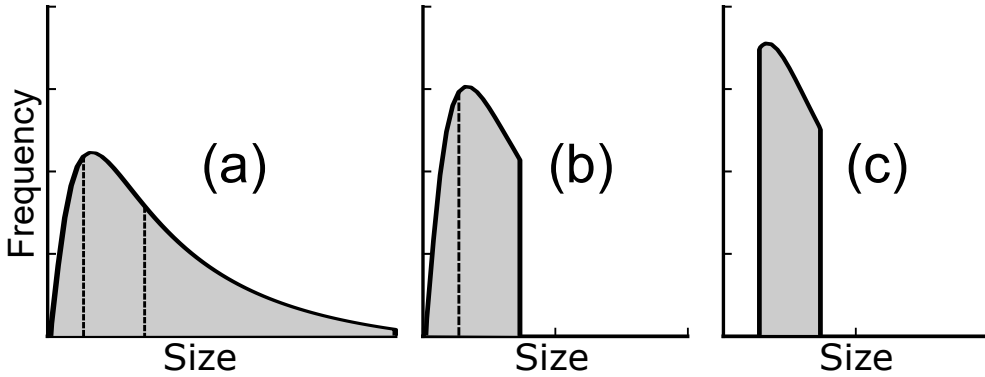


Figure 3.2: Ideal case of the isolation of certain size range by successive steps. Frequency distributions (a) initially, (b) after first step and (c) after second step.

and the number, weight and area distributions of the particles are all log-normal with same standard deviation [18].

A review of mathematical models of centrifugation is given in the following section, where key elements of novelty of the current analysis are highlighted. The mathematical model used in the current investigation is described in Sec.3.3, and results discussing solutions of this model for homogeneous or band sedimentation are discussed in Sec.5.4. To illustrate the practical application of the theory, in Sec. 3.5 we describe two applied cases, fractionation of spherical metallic nanoparticles and fractionation of graphene platelets. We chose graphene because the development of a protocol to fractionate graphene would enable to overcome one of the biggest bottlenecks in large-scale graphene production, namely the large polydispersity in lateral size and thickness of the platelets produced [19]. Finally, conclusions are drawn in Sec.3.6.

3.2 Overview of mathematical models of sedimentation/centrifugation

The evolution of the particle size distribution following the application of a constant body force to a particulate system can be modeled via a set of one-dimensional transport equations, each governing the particle number density (or volume fraction) corresponding to each size class. Kynch [20] analysed a monodisperse particulate system via one such model, excluding particle diffusion. Kynch's model could capture the discontinuity in the volume fraction profile in correspondence to the liquid-suspension and suspension-sediment interfaces observed in experiments. By extending Kynch's theory by adding a diffusive term to the transport equation, Davis and Russel [21] analysed the diffusive broadening of the concentration fronts due to Brownian motion. Blanchette and Bush [22] studied the evolution of particle volume fraction during sedimentation of monodisperse particles in a density stratified medium. Antonopoulou et

al. [23] developed a one-dimensional continuum model for sedimentation of monodisperse colloidal particles in centrifugation. To account for the fact that the sediment layer grows in size when it is sufficiently packed, they incorporated into the model an effective maximum volume fraction, derived by considering the minimum separation between two spherical colloids.

Theoretical studies on systems of 2 or 3 size classes are available [24–26], whereas theoretical studies on sedimentation of widely polydispersed systems (i.e. number of classes significantly larger than 3) are scarce. Esipov [27] analysed a theoretical model for polydispersed suspensions. The settling velocity of each class was closed in terms of a weighted average of the volume fraction of each particle class, leading to a set of coupled Burgers equations. The initial Gaussian particle size distribution was discretized with 26 particle classes. Xue and Sun [28] compared experimental results with the solution of a one-dimensional convection equation (Brownian motion and hydrodynamic diffusion were neglected), considering 35 size classes. A similar model was used by Abeynaïke et al. [3], with up to 8 size classes.

In contrast to the works above, we consider a fine discretization of the particle size distribution with 1000 size classes, to predict the evolution of a continuous log-normal size distribution with specified mean and variance values. A further key difference with previous works is that, we focus on the time evolution of the particle size distribution in the supernatant vs. that in the sedimented layer, while previous works focused on the time evolution of concentration profiles for each particle class. A key novelty of the current paper is that the work published so far considered single-step sedimentation, meaning that starting from a mixed suspension the simulations ended when all the particles reached the bottom of the container. In contrast, we consider multi-step sedimentation in which the sediment is removed after a given time and the remaining suspension is subjected to a further sedimentation step.

3.3 Mathematical model of this chapter

We consider a dispersed system contained in a straight vial of height H . The body force acting on the dispersed phase (which is equal to the gravity force in sedimentation and to the centrifugal force in centrifugation) is assumed to be constant along the vial and directed parallel to the side walls of the vial (see Fig.3.1). We seek to describe the number density $N(x, t, q)$ of particles at position x and time t having settling velocity q , with $x = 0$ corresponding to the free surface of the liquid (the axis x is directed towards the bottom of the vial). We focus initially on particle velocity, and not on particle size, because calculating the time evolution of the size distribution requires stipulating a relation between size and velocity, and this relation depends on the specific shape of the particles, hence it is not universal. Once the problem is un-

derstood and modeled in the velocity space, the results can be translated in terms of size (see Sec. 3.5).

The time evolution of $N(x, t, q)$ is governed by a convection-diffusion equation [29]:

$$\frac{\partial}{\partial t} N(x, t, q) + \frac{\partial}{\partial x} (qN(x, t, q)) = \frac{\partial F_D}{\partial x}. \quad (3.1)$$

Here F_D is a diffusive flux accounting for the diffusive transport of the particles in the x direction (by either Brownian motion or hydrodynamic diffusion). The second term on the left-hand side represents the convection of the dispersed phase by the body force. The settling velocity q is in general a function of the particle size, particle density, effective density of the suspension, concentration of the particles with velocity q , and concentration of the particles with velocity different from q [29, 30]. The diffusive flux also depends on full size distribution. Many papers considered the problem of closing the hindered settling function for polydispersed systems [30–34]. Because of the complexity of the multi-step situation and to produce a theoretical baseline for future work, in our simulation we do not consider hindered settling effects. We assume that the suspension is extremely dilute, i.e. the total volume fraction of the dispersed phase $\varphi_T \ll 1$, so that hydrodynamic and contact interactions between the dispersed phase elements can be neglected. In this case, q becomes independent of N and can be taken out of the differentiation. Furthermore, if hydrodynamic and contact interactions are negligible, the diffusive flux is also negligible. With the further assumption that Brownian motion is negligible (high Péclet number), Eq.3.1 simplifies to the following linear convective equation:

$$\frac{\partial}{\partial t} N(x, t, q) + q \frac{\partial}{\partial x} N(x, t, q) = 0. \quad (3.2)$$

The characteristic time scale for convection over a length H is H/q . The ratio of the diffusive time scale H^2/D to the convective time scale is the Péclet number $Pe = Hq/D$, where D is the diffusion coefficient of the particle [1]. For spherical particles, the condition for particle radius a of negligible diffusion in centrifugation ($Pe > 1$) corresponds to $a^3 > 3k_B T/4\pi H(\rho_p - \rho_l)g_e$, where $k_B T$ is the characteristic thermal energy, ρ_p and ρ_l as densities of particles and solvent respectively, g_e as the centrifugal acceleration, and the relation of a and g_e making $Pe = 1$ is plotted in Fig.3.3 assuming $H = 1\text{cm}$, $(\rho_p - \rho_l) = 1000\text{kg/m}^3$, and at room temperature.

We solve equation 3.2 numerically and analytically for the initial condition:

$$N(x, t = 0, q) = N_0(x, q), \quad (3.3)$$

where $N_0(x, q)$ is the initial particle number density of particles with velocity q at position x . We consider two situations: the particles are homogeneously distributed

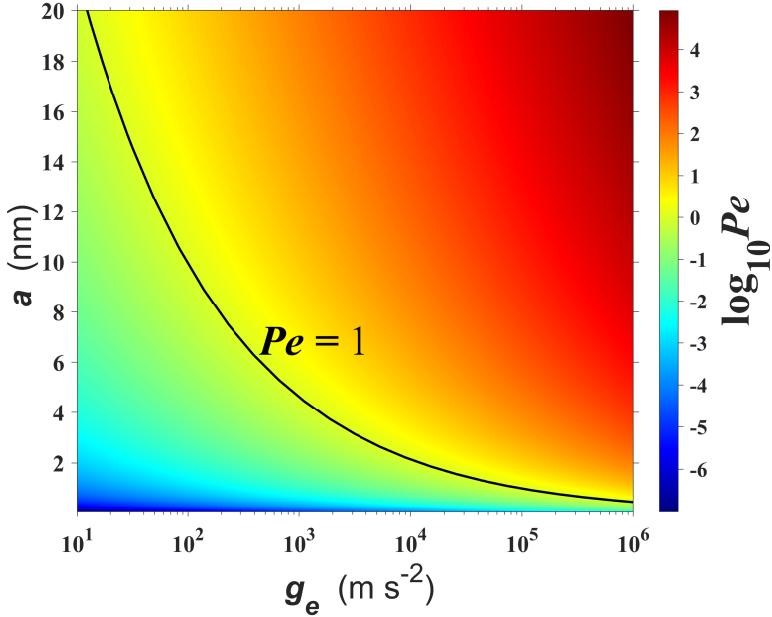


Figure 3.3: Color map of logarithm value of Péclet number of spherical particles in the (a, g_e) space. The black line is $Pe = 1$.

in a slab of height $h < H$ near the top of the vial (case 1, band sedimentation); or the particles are homogeneously distributed in $x \in [0, H]$ (case 2, homogeneous sedimentation). The model equation is solved in a half-bounded region $x \in [0, \infty)$, where $x = 0$ corresponds to the free interface at the top of the vial. The particles are considered to be sedimented when they reach $x = H$.

In the dilute limit, the settling velocity is only a function of the particle geometry. The settling velocity q of an isotropic (spherical) particle (Eq.3.9) or an anisotropic (disk) particle (Eq.3.10) is given in Sec.3.5. We consider an initial log-normal distribution of q as an illustration of the application of the theory (note that for disks the settling velocity is log-normally distributed if lateral size d and thickness L are both log-normally distributed and independent [35]).

For n_q discrete size species Eq.3.2 becomes

$$\frac{\partial}{\partial t} N_i(x, t; q_i) + q_i \frac{\partial}{\partial x} N_i(x, t; q_i) = 0, \quad i = 1, 2, \dots, n_q, \quad (3.4)$$

where $N_i(x, t; q_i)$ is the number density of species i with settling velocity q_i . The initial condition for species i is

$$N_i(x, 0; q_i) = f_0(q_i) n_0(x), \quad (3.5)$$

where $n_0(x)$ is the initial total particle number density including all the species at position x , and $f_0(q_i)$ is the frequency of species i in the original sample. For case 1 (band sedimentation), we specify

$$n_0^*(x^*) = \begin{cases} 1 & \text{for } 0 \leq x^* \leq 0.1 \\ 0 & \text{for } 0.1 < x^* \leq 1 \end{cases} \quad (3.6)$$

For case 2 (homogeneous sedimentation), we specify

$$n_0^*(x^*) = 1, \quad 0 \leq x^* \leq 1. \quad (3.7)$$

Here variables with superscript (*) are dimensionless, and $x^* = x/H$, $n_0^* = n_0/m$ where m is the initial number density value everywhere in the particle-laden region.

The numerical procedure to solve Eq.3.4 proceeds as follows. From the probability distribution function (p.d.f.) of q , $p(q)$, a discrete frequency distribution $f(q_i)$ can be calculated for $i = 1, \dots, n_q$, dividing the range $[0, Q]$ into n_q slabs of size $\Delta q = Q/n_q$. Here Q is an assigned maximum value of q at which the upper tail of the p.d.f. is cut. The value of $f(q_i)$ gives the percentage fraction of particles with velocities between q_i and $q_i + \Delta q$, and is calculated as $f(q_i) = p(q_i) / \sum_{i=1}^{n_q} p(q_i)$. In our discretization, the nodes are centered at each slab, so $q_i = (i - 0.5)\Delta q$. The frequency distribution at time $t = 0$ is denoted as $f_0(q_i)$. Eq.3.4 is then solved by a finite difference method in which spatial derivative is discretized by a first-order upwind scheme and time is integrated by a first-order Euler scheme.

The solution of Eq.3.4 gives the probability of having particles of a given class q_i for any position x at time t . In a multistep sedimentation process, the interest is in characterizing how the particle distribution in the supernatant differs from that in the sedimented layer. The number of particles of size q_i in the supernatant, denoted as $n^s(q_i)$ is calculated by integrating over the entire length of the vial, assuming that the particles which have crossed the boundary $x = H$ as the sedimented layer: $n^s(q_i) = \int_0^H N(t, x; q_i) dx$. The number of particles in the sedimented layer is $n^b(q_i) = \int_H^\infty N(t, x; q_i) dx$. The corresponding frequencies are $f^s(q_i) = n^s(q_i) / \sum n^s(q_i)$ and $f^b(q_i) = n^b(q_i) / \sum n^b(q_i)$. The sum n^t of the number of particles in the supernatant and in the sedimented layer is evidently equal to the initial number of particles: $n^t = n^s + n^b = \int_0^H n_0(x) dx$.

3.4 Results and discussion

3.4.1 Time evolution of the frequency distribution: supernatant v.s. sediment layer

A log-normal p.d.f. $p(q)$ with mean value of q as 0.1 and variance of q as 0.01 is shown in Fig.3.4(a). Note that the settling velocity q is non-dimensionalized by a

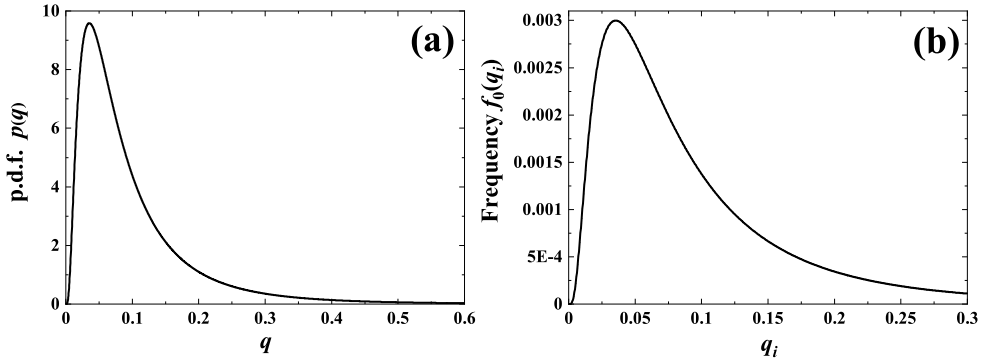


Figure 3.4: (a) p.d.f. of a log-normal distribution with mean value 0.1 and variance 0.01. (b) Discretized frequency distribution for 1000 species corresponding to (a).

characteristic velocity (e.g. the settling velocity of a particle with certain size). It is seen that for these parameters most of the distribution falls within $q \in (0, 0.3)$, so we choose the maximum size $Q = 0.3$. By choosing $Q = 0.3$ and $n_q = 1000$, the interval from $q = 0$ to 0.3 is discretized into 1000 slabs of increment $\Delta q = 0.0003$. The corresponding frequency distribution $f_0(q_i)$ is shown in Fig.3.4(b).

Time evolutions of the frequency distributions in the supernatant and in the sediment layer are shown in Fig.3.5 and Fig.3.6, respectively, for both case 1 (band sedimentation) and case 2 (homogeneous sedimentation). From Fig.3.5, it is seen that there are fewer size classes in the supernatant as time goes by because the larger particles sediment on the bottom quicker. The largest size classes in the supernatant are the same for band and homogeneous sedimentation at the same time. However, the moving front of the frequency distribution curve of the supernatant in band sedimentation is sharper than that in homogeneous sedimentation. From Fig.3.6, it is seen that the sediment layer in homogeneous sedimentation always contains all the size classes, whereas in band sedimentation the smaller size classes come to the sediment layer at later times. In Fig.3.7, the frequency distributions in the supernatant and in the sediment layer at the same time $t = 10$ are plotted together for both band and homogeneous sedimentation. It is seen that the curves overlap slightly in band sedimentation, which means there is clear distinction between the size classes in the supernatant and the size classes in the sediment layer. However, all the size classes in the supernatant appear in the sediment layer for homogeneous sedimentation.

3.4.2 Particle fractions in the supernatant and in the sediment layer

Fig.3.8 shows the time evolution of particle fractions in the supernatant and in the sedimented layer, respectively, for both band and homogeneous sedimentation. Due

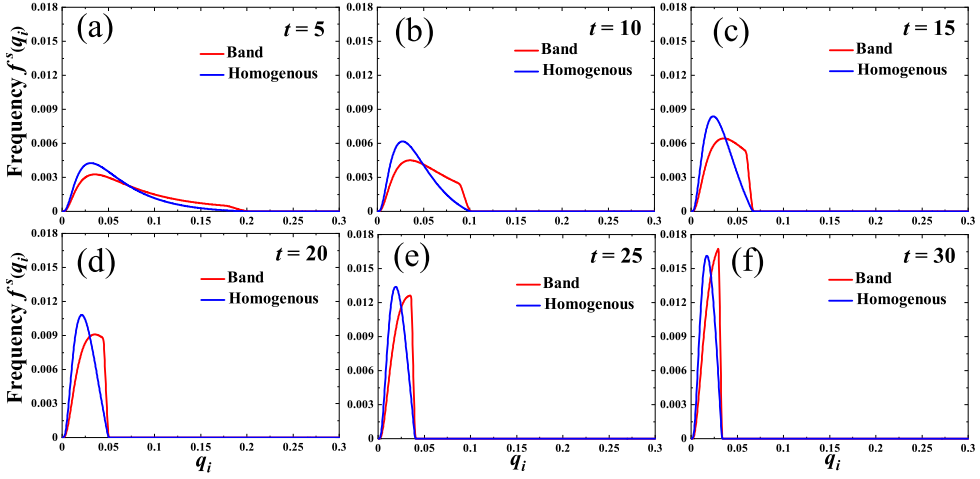


Figure 3.5: Time evolution of the frequency distributions in the supernatant for case 1 (red lines) and case 2 (blue lines).

to the existence of clear fluid under the particle-laden layer in band sedimentation, the decreasing of particle fraction in the supernatant is delayed, whereas the particle fraction in the supernatant starts to decrease from the beginning in homogeneous sedimentation. Moreover, it is seen that particle fraction in the supernatant decays faster in homogeneous sedimentation than that in band sedimentation by comparing the slopes of the curves of the two cases.

In both band and homogeneous sedimentation the initial frequency distribution is “cut” by a front that moves to the left with a certain velocity (see Fig.3.5). This velocity can well be characterized as the velocity of q_{\max}^s , the largest particle size in the supernatant. Because the transport equation Eq.3.4 is linear, $N_i(x, t; q_i)$ can be easily calculated analytically. From the value of $N_i(x, t; q_i)$, particle number of species q_i in the supernatant at time t , which is $n^s(q_i, t)$, can be calculated by integration. Setting $n^s(q_i, t) = 0$ provides the following relationship between q_{\max}^s and t (see Appendix A.1 for details):

$$q_{\max}^s = \begin{cases} H/t & \text{for } t > H/Q \\ Q & \text{for } t \leq H/Q \end{cases}, \quad (3.8)$$

where H is the length from the free interface to the bottom of the vial, and Q is the largest value of q of the original sample. The validity of this expression is demonstrated in Fig.3.9, where the simulated values of q_{\max}^s with varying time are plotted.

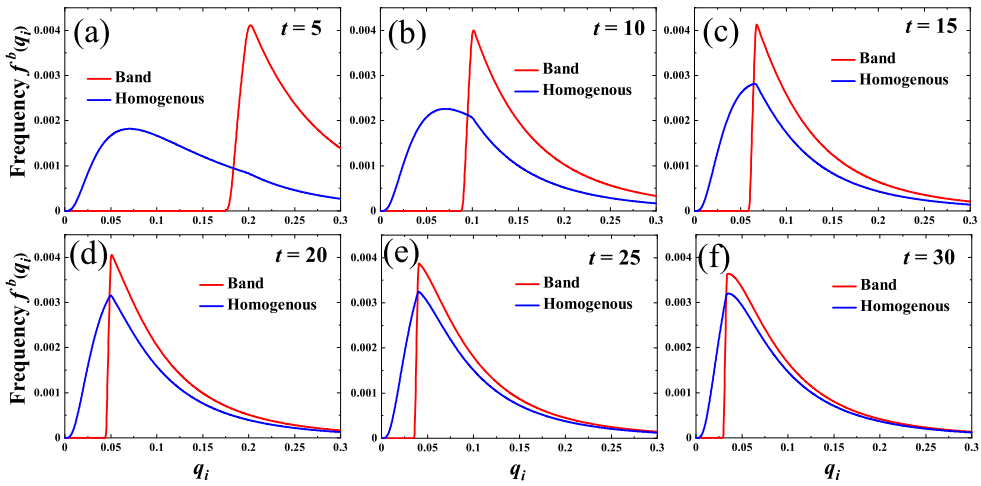


Figure 3.6: Time evolution of the frequency distributions in the sediment layer for case 1 (red lines) and case 2 (blue lines).

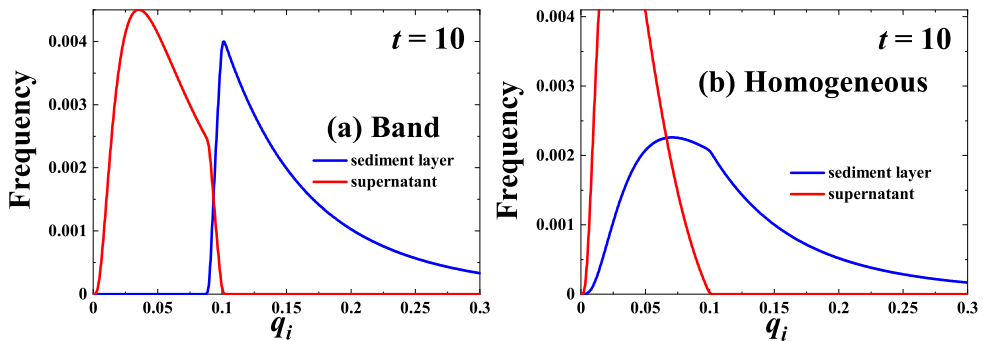


Figure 3.7: Frequency distributions of particles in the supernatant (red lines) v.s. in the sediment layer (blue lines) at $t = 10$ for (a) case 1 band sedimentation, and (b) case 2 homogeneous sedimentation.

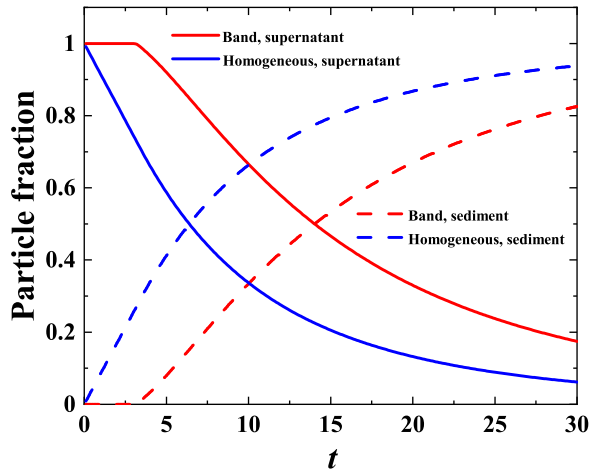


Figure 3.8: Time evolution of particle fractions in the supernatant and in the sedimented layer for both band and homogeneous sedimentation.

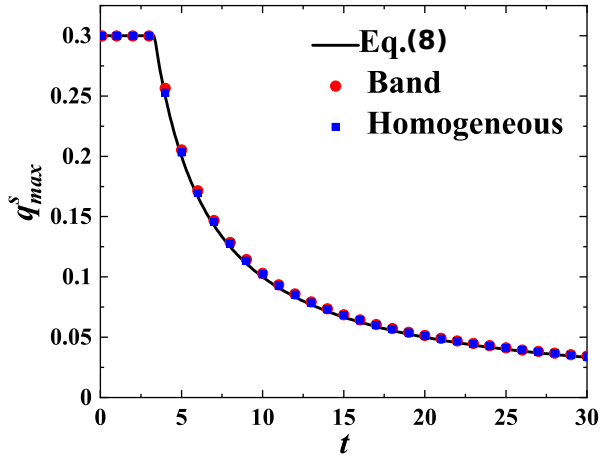


Figure 3.9: The value of q_{max}^s versus time t . Eq.(8), band and homogeneous sedimentation are shown by the solid line, circular and square symbols, respectively.

3.4.3 Minimisation of impurities

The presence of a front that moves with velocity given by Eq.3.8 suggests a protocol to isolate a certain interval of the frequency distribution. Suppose we would like to separate particles with $q \in (q_{\min}, q_{\max})$ from all the other particles, where q_{\min} and q_{\max} are somewhere in the middle of the frequency distribution. An intuitive protocol is to centrifuge the suspension for a certain time and discard the sediment. This would give in the supernatant a suspension containing only particles with velocities less than a certain threshold. Then we could take the supernatant, centrifuge it again and in this case remove the supernatant. In the sedimented layer, we would have particles having an intermediate range of velocities larger than a minimum threshold and smaller than a maximum threshold. The sequence could be repeated again, with different centrifugation times assigned to each step. The problem is to predict how the *observed* thresholds depend on the *assigned* q_{\min} and q_{\max} for a given sequence of centrifugation times. Solving this problem requires choosing the centrifugation time rationally so that the amount of impurities is minimized. We have found in the previous section that the initial size distribution cannot be cut sharply into two parts (i.e. the frequency curves in the supernatant and in the sediment layer overlap at each time), and a certain amount of small velocity (finer) particles will always reach the bottom.

An insight from the previous section is that the time scale of motion of the front is given by the ratio of the vial height H and the front velocity. This suggests that the centrifugation times should be chosen based on the ratio of H with q_{\max} and q_{\min} . We therefore propose the following algorithm, whose convergence and error we aim to characterize (in the same way as done for algorithms implementing numerical methods in scientific computing):

Step 0: Calculate centrifugation times $t_{\min} = H/q_{\max}$ and $t_{\max} = H/q_{\min}$, and set $\Delta t = (t_{\max} - t_{\min})/(\mathcal{N} - 1)$ based on the total centrifugation steps \mathcal{N} .

Step 1: Centrifuge the suspension, using a constant body force, for a time $t_1 = t_{\min}$. Move the supernatant to another test tube which is to be centrifuged in the next step. Discard the sediment.

Step 2: Centrifuge the supernatant from the previous step 1 for a time $t_2 = t_1 + \Delta t$. Move the supernatant to another test tube for the next step centrifugation. Collect the sediment as part of the separated sample.

Step 3: Centrifuge the supernatant from the previous step 2 for time $t_3 = t_2 + \Delta t$. Move the supernatant to another test tube for the next step centrifugation. Collect the sediment as part of the separated sample.

...

Step $\mathcal{N} - 1$: Centrifuge the supernatant from the previous step $\mathcal{N} - 2$ for time $t_{\mathcal{N}-1} = t_{\mathcal{N}-2} + \Delta t$. Move the supernatant to another test tube for the next step centrifugation. Collect the sediment as part of the separated sample.

Step \mathcal{N} : Centrifuge the supernatant from the previous step $\mathcal{N} - 1$ for time $t_{\mathcal{N}} = t_{\max}$. Discard the supernatant. Collect the sediment as part of the separated sample.

Step $\mathcal{N} + 1$: Assemble all the collected sediment from Steps 2, 3, \dots , $\mathcal{N} - 1$ and \mathcal{N} as the separated sample.

According to Eq.3.8, the largest value of q in the supernatant at the end of Step 1 is q_{\max} . This means that all the particles with $q > q_{\max}$ in the original sample have settled at the bottom wall in Step 1, and therefore the sediment should be completely discarded in Step 1 as according to the prediction it does not contain useful particles. On the other hand, according to the prediction at the end of Step \mathcal{N} , the largest value of q in the supernatant is q_{\min} , which means the supernatant contains particles smaller than the desired ones. Hence the supernatant at the end of step \mathcal{N} should be discarded. The model predicts that particles with $q \in (q_{\min}, q_{\max})$ have settled on the bottom wall gradually from Step 2 to Step \mathcal{N} . That is why the sediment layers from steps 2 \dots \mathcal{N} should be collected and mixed together, and the collected sample has a distribution whose shape depends on the number of total centrifugation steps \mathcal{N} .

Effect of the number of steps

An example is given in the current subsection to show how the multi-step approach works and how the number of centrifugation steps may be chosen. Suppose particles with $q \in (0.025, 0.045)$ from the log-normally distributed system shown in Fig.3.4(b) are desired. This interval is chosen because it contains the value of q corresponding to the peak of the initial frequency distribution, $q = 0.035$. The calculated values of t_{\min} and t_{\max} are 22.2 and 40, respectively (step 0). We need to devise \mathcal{N} steps of successive centrifugation, for which $t_1 = 22.2$ in Step 1 and $t_{\mathcal{N}} = 40$ in Step \mathcal{N} . We would like to know how the purity of the sample depends on \mathcal{N} .

Because we know that band sedimentation gives a sharper division of the initial frequency distribution, we anticipate that the level of purity given by band sedimentation is larger than that by homogeneous sedimentation. Hence, we consider two cases: in case A, the initial condition for each step of centrifugation is that the particles are uniformly dispersed within a top layer of length 0.1 as band sedimentation; in case B, the initial condition of each centrifugation step is that the particles are uniformly dispersed in the whole solvent of length 1 as homogeneous sedimentation.

The frequency distributions of the particles in the supernatant and in the sediment layer after Step 1 of centrifugation are shown in Fig.3.10. In agreement with the prediction, Fig.3.10(a) shows that all the particles remaining in the supernatant are of q smaller than 0.045. The sediment layer at the end of Step 1 contains, as expected, particles larger than the desired ones, and also a fraction of the desired ones from the original sample as indicated by the frequency distributions between $q = 0.025$ and

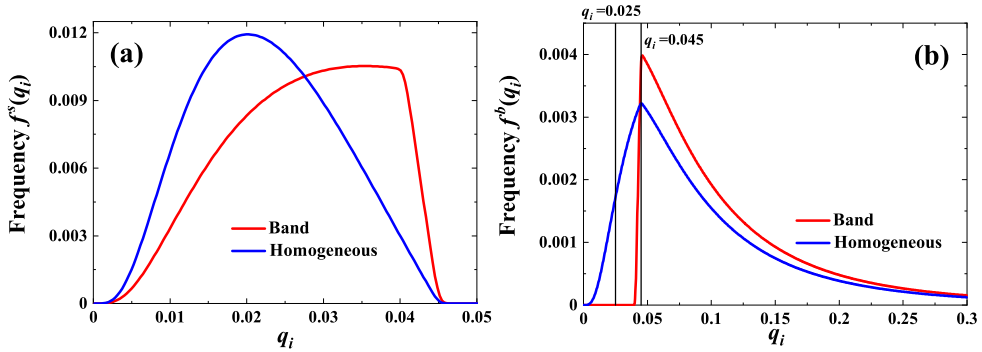


Figure 3.10: Frequency distributions after Step 1 of centrifugation for particles (a) in the supernatant and (b) in the sedimented layer. (Band sedimentation is shown as red lines, and homogeneous sedimentation as blue lines. The two vertical thin lines in (b) mark q equals 0.025 and 0.045, respectively.)

$q = 0.045$ (marked by two thin vertical lines in Fig.3.10(b)). This fraction, i.e. the ratio of the numbers of particles with $q \in (0.025, 0.045)$ in the sedimented layer after Step 1 and in the original sample, is 13.6% for case A and 78.4% for case B, respectively. This means the yield will be much higher in band sedimentation than that in homogeneous sedimentation.

We now analyze how the shape of the frequency distribution of the separated sample changes with \mathcal{N} . This will give us insights into how to choose the number of centrifugation steps in the separation algorithm. Fig.3.11 shows the frequency distributions of the separated sample as \mathcal{N} equals 2, 3, 4 and 5, respectively. For comparison, the frequency distribution of particles with $q \in (0.025, 0.045)$ in the original sample is also shown in Fig.3.11. It is seen that in case A (band sedimentation) the frequency distribution curve nearly remains the same as \mathcal{N} increases, thus the separation algorithm converges fast and using $\mathcal{N} = 2$ gives predictions that are no worse than those obtained for $\mathcal{N} = 3$. There are differences with the “desired” size distribution, shown in black. In particular, while the maximum value of q is 0.045 as desired, the fraction of particles with velocities close to 0.045 is smaller than that in the original distribution (there is an evident drop in frequency for q larger than about 0.042). In case B (homogeneous sedimentation), the separation algorithm instead does not converge. The curve becomes smoother as \mathcal{N} increases, assuming an approximate bell shape, and the peak value shifts to the left (smaller values of q) as \mathcal{N} increases. The shape of the frequency distribution is quite different from the desired one, although the range of q covers the desired range.

To characterize the convergence properties more synthetically, Fig.3.12(a) shows the mean value and standard deviation of q of the separated sample for \mathcal{N} equals 2,

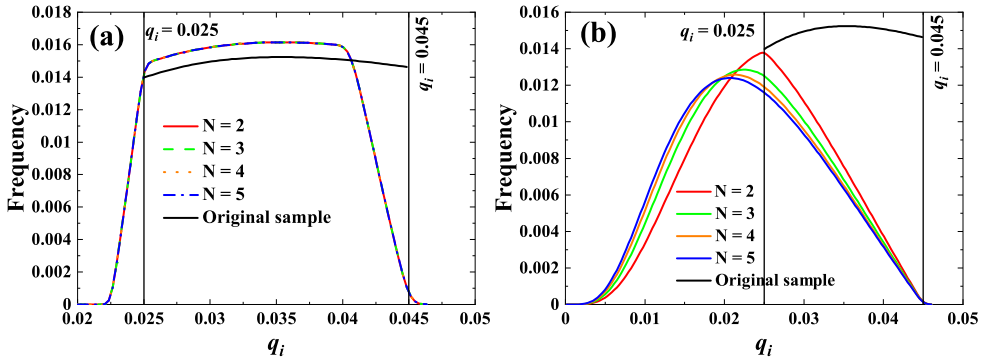


Figure 3.11: Frequency distributions of the separated sample as the total number of centrifugation steps N equals 2, 3, 4 and 5 for (a) case A (band sedimentation) and (b) case B (homogeneous sedimentation), together with that of particles within the desired range in the original sample. (The two vertical lines mark q as 0.025 and 0.045 in both (a) and (b).)

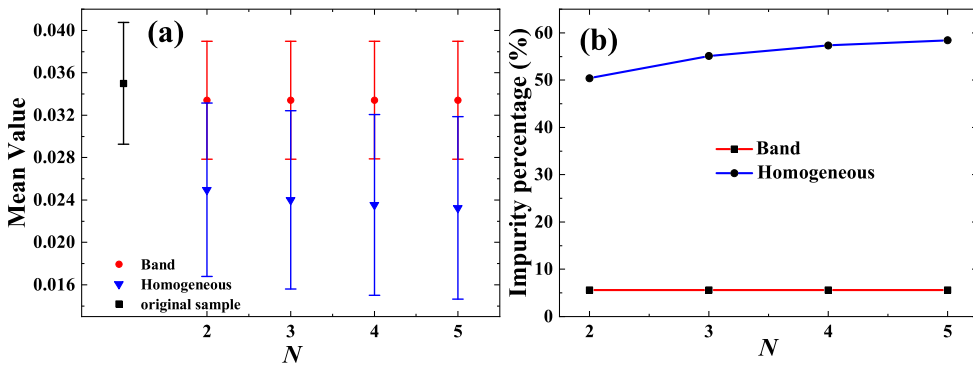


Figure 3.12: (a) Mean value and standard deviation of q and (b) the impurity percentage of the separated sample for different N values for both band and homogeneous sedimentation. The corresponding values of the desired particles in original sample are also shown in (a).

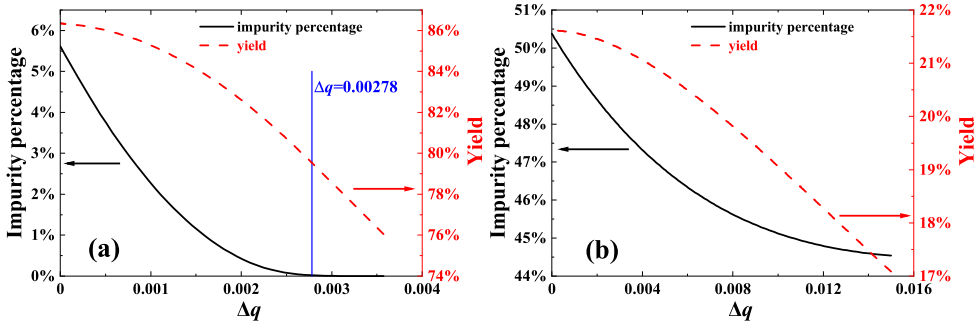


Figure 3.13: The impurity percentage and yield as Δq increases for (a) case A and (b) case B, respectively. The vertical line in (a) marks Δq equals 0.00278.

3, 4 and 5. It is seen that the mean value in case B (homogeneous sedimentation) is smaller than that in case A (band sedimentation), and standard deviation in case B is larger than that in case A. The impurity percentage of the separated sample, defined as the ratio of the number of particles with q outside $(0.025, 0.045)$ to the total particle number of the sample, is shown in Fig.3.12(b). In case A the statistics converge fast and the impurity level is always below 10%. In case B, the impurity level is around 50% for \mathcal{N} equals 2 and increases as the number of steps increases.

An improved fractionation protocol

Based on the results from the last subsection, it is inferred that choosing $\mathcal{N} = 2$ minimizes the impurity percentage. This suggests that a simple two-step approach, as follows, is practical and beneficial for the fractionation of a given range (q_{\min}, q_{\max}) :
Step 1: Centrifuge the suspension for time t_1 , keep the supernatant for the next step centrifugation and discard the sediment.

Step 2: Centrifuge the supernatant from Step 1 for time t_2 , then collect the sediment as the separated sample and discard the supernatant.

There is clearly an arbitrariness in the choice of t_1 and t_2 . The previous subsection suggests that the time scales should be $t_1 = H/q_{\max}$ and $t_2 = H/q_{\min}$, but choosing values that are close, but not identical, to these two limits may give better result. The impurities in the separated sample are particles with q smaller than q_{\min} . Thus, the time t_2 could be decreased to let fewer smaller particles sediment on the bottom wall and decrease the impurity percentage. To explore this possibility, we set $t_2 = H/(q_{\min} + \Delta q)$ and study the fractionation efficiency as a function of the parameter Δq ($0 < \Delta q < (q_{\max} - q_{\min})$). Apart from the impurity percentage, the other quantity of interest is the yield, defined as:

$$\text{yield} = \frac{\text{number of particles with } q \in (q_{\min}, q_{\max}) \text{ in the separated sample}}{\text{number of particles with } q \in (q_{\min}, q_{\max}) \text{ in the original sample}}.$$

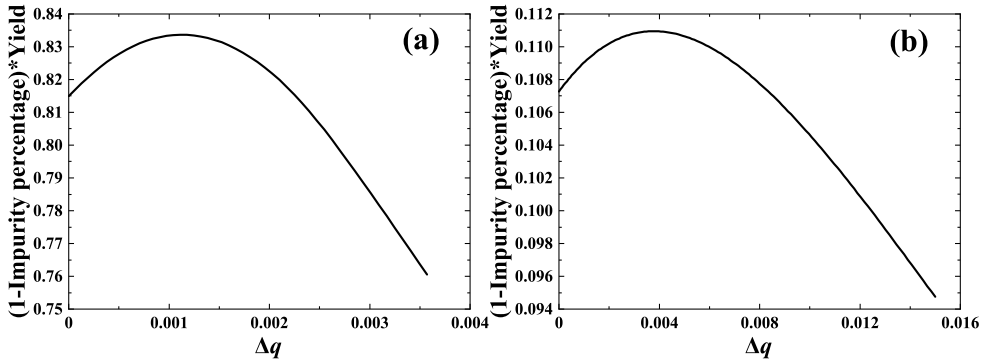


Figure 3.14: The value of $(1 - \text{impurity percentage}) \times \text{yield}$ as Δq increases for (a) case A and (b) case B, respectively.

By increasing Δq , we expect a decrease in impurity level but also a decrease in yield. To see the effect of increasing Δq , cases A and B in the last subsection are considered here following the modified two-step approach described above. The simulation results, shown in Fig.3.13, confirm that the impurity percentage and yield both decrease as Δq increases. An optimised algorithm would have a comparatively large yield and a large purity. Therefore we use an objective function, $(1 - \text{impurity percentage}) \times \text{yield}$, to indicate the balance between yield and purity, as shown in Fig.3.14. This objective function has a peak value, which corresponds to $\Delta q \simeq 0.001$ and $\Delta q \simeq 0.004$, for cases A and B respectively. The fact that $\Delta q \ll (q_{\max} - q_{\min})$ means that our original choice of $\Delta q = 0$ was actually quite close to the optimal. Looking at Fig.3.13, however, one can see that while the yield does not decrease much by choosing the optimal value instead of $\Delta q = 0$, the impurity percentage drops substantially in case A (from 5.5% to about 1.5%) because the slope of the impurity percentage curve is large when Δq is small. This example illustrates that a finely tuned algorithm, or fractionation protocol, can have substantial effects on the purity level. Another interesting modification is to replace $t_2 = H/q_{\min}$ with $t_2 = (H - h)/q_{\min}$ in case A, where h is the initial length of the particle-laden region, and this is equivalent to choose $\Delta q = q_{\min}(h/(H - h))$. With this choice the predicted impurity percentage is 0 in case A. As indicated by Fig.3.13(a), the impurity percentage is 0 when $\Delta q = 0.025 \times 0.1 / (1 - 0.1) = 0.00278$.

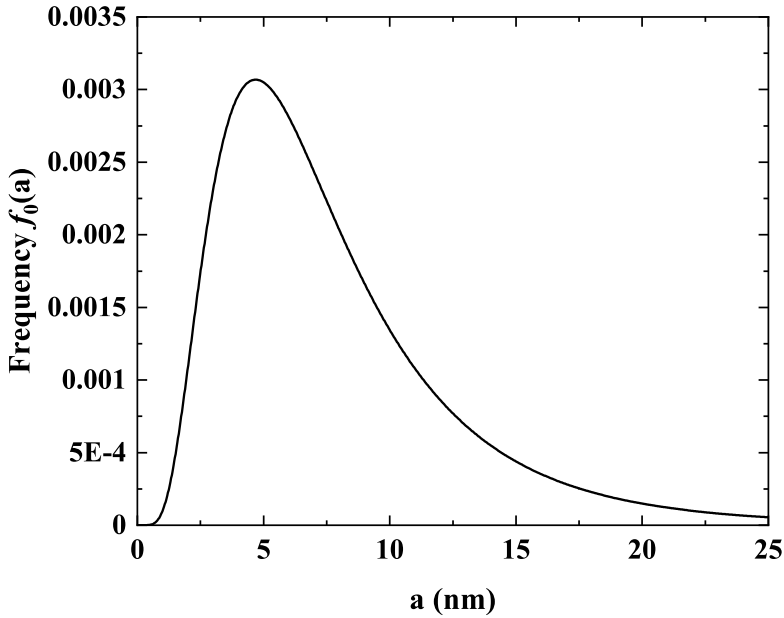


Figure 3.15: Radius frequency distribution of the chosen AuNP sample.

3.5 Practical applications of the theory

3.5.1 Fractionation of nearly spherical metallic nanoparticles (isotropic particles)

Nominally spherical metallic nanoparticles with well-controlled size range are important for many applications, ranging from drug delivery [36], medical diagnostics and sensors [37], electrochemical applications [38] to catalytic applications [39]. For spherical particle of radius a in Stokes flow, the single-particle settling velocity is [40]

$$q = \frac{2}{9} \frac{(\rho_p - \rho_l)}{\mu} g_e a^2. \quad (3.9)$$

Here ρ_p and ρ_l are densities of the particle and medium liquid, respectively, μ is the dynamic viscosity of the liquid, and g_e is the equivalent g -force of the centrifugation $g_e = R\omega^2$ where R is the rotor radius and ω is the rotational speed of the rotor.

To illustrate how to predict the impurity percentage and yield during a centrifugation process and to design an optimal two-step procedure aiming at lower impurity percentage, we take an example from ref.[41] where Au nanoparticles (AuNPs) are fractionated by centrifugation. We consider the AuNP sample has a log-normal radius distribution with mean value 7.9 nm and standard deviation 5.1 nm (see Table 1 and Figure 2a in ref.[41], note that in ref.[41] size was characterized using diameter

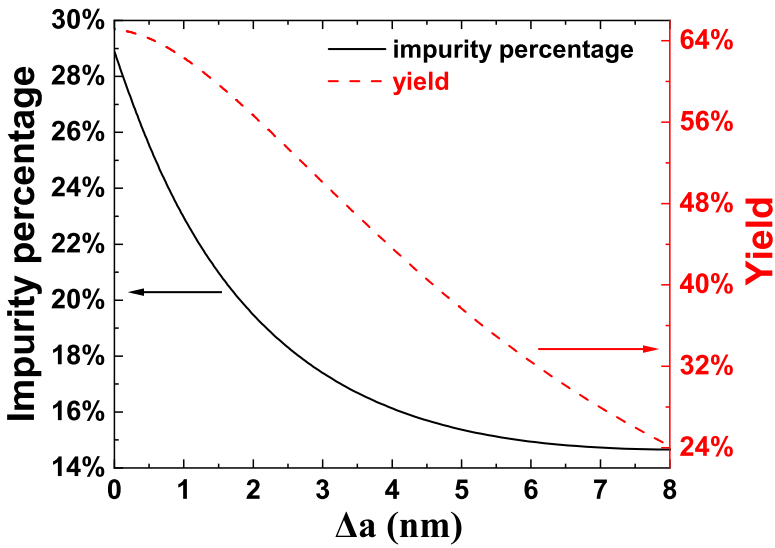


Figure 3.16: Effect of the offset value on impurity percentage and yield for homogeneous centrifugation.

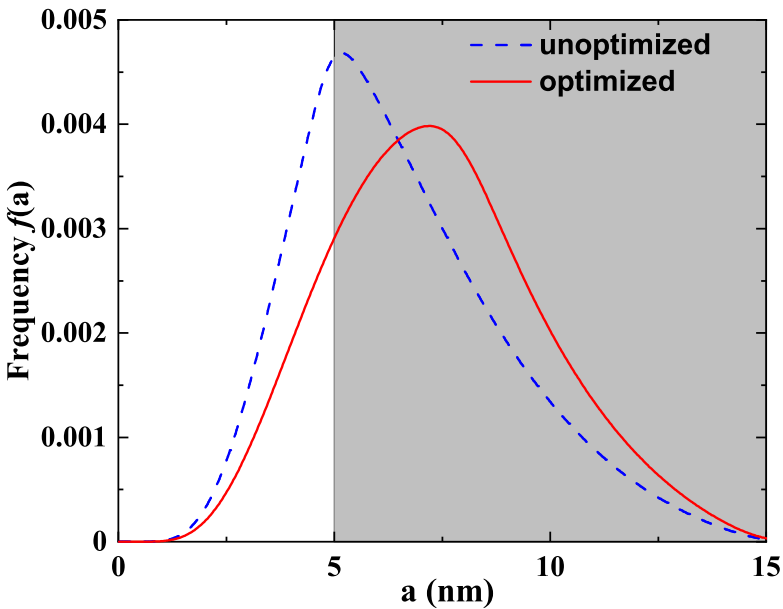


Figure 3.17: Size frequency distributions of the fractionated AuNPs by the unoptimized or optimized (choosing Δa as 3 nm) two-step procedures, shaded region is the desired size range (5-15 nm).

whereas it's radius here). The frequency distribution of the radius is shown in Fig.3.15 with a cut at 25 nm. The desired radius range is 5-15 nm. As shown in Sec.3.4.3, a two-step protocol can be adopted. In the first step, the centrifugation parameters (time or rpm) should be calculated using the largest desired size (i.e. 15 nm). In the second step, the unoptimized way is to calculate the centrifugation parameters using the smallest desired size (i.e. 5 nm). However, as shown in Sec.3.4.3, adding an offset value ($\Delta\alpha$) to the smallest desired size to calculate the centrifugation parameters can lead to lower impurity percentage (optimized way). Note that the possible value of $\Delta\alpha$ in this case is between 0 to 10 nm. By numerically solving the set of linear convective equations Eq.3.4, the effect of adding an offset value $\Delta\alpha$ on impurity percentage and yield is shown in Fig.3.16. Note that Fig.3.16 is constructed assuming an homogeneous solution before each step of the procedure (i.e. homogeneous centrifugation), as this is more easy and practical for multicascade centrifugation. From this reference map, we can see that by choosing $\Delta\alpha$ as 3 nm the impurity percentage drops from 29% to 17% whereas the yield (defined in Sec.3.4.3) drops from 65% to 50%. The size frequency distributions of the fractionated sample by unoptimized or optimized (choosing $\Delta\alpha$ as 3 nm) two-step procedures are shown in Fig.3.17. From Fig.3.17, it is seen that the distribution from the optimized procedure has a larger fraction in the desired range than that from the unoptimized procedure, which means the fractionated sample from the optimized procedure has lower impurity percentage. The mean values of the distributions shown in Fig.3.17 are 7.40 nm for optimized procedure and 6.57 nm for unoptimized procedure. The standard deviations are 2.46 nm for optimized procedure and 2.43 nm for unoptimized procedure.

3.5.2 Fractionation of graphene (anisotropic particles)

Liquid-phase exfoliation (LPE) is a promising method [42, 43] to produce 2D nanomaterials, such as graphene [44–46], MoS₂ [47, 48] or BN [49, 50]. The flakes produced with LPE tend to be polydispersed in lateral size and thickness [51, 52], with both variables following approximately log-normal distributions [52, 53]. Fractionation of 2D nanomaterials by centrifugation is very common [8–10, 41, 54].

In the following we refer to graphene, but the results are equally applicable to other 2D nanomaterials. Modelling a graphene flake as a disk-like particle of diameter d and thickness L , the settling velocity is (see Appendix A.2 for derivation)

$$q = \frac{\pi}{27.48\mu} (\rho_p - \rho_l) g_e dL. \quad (3.10)$$

The settling velocity q of a disk is proportional to the product of lateral size d and thickness L . If both d and L are log-normally distributed, q also follows log-normal distribution assuming d and L are independent. However, statistical analysis of large

amount nanoflakes produced by LPE shows that the average values of lateral size and thickness are correlated by a power law $\langle d \rangle \sim \langle L \rangle^r$, with the exponent r depending on the type of the material and the exfoliation procedure [51, 52]. Based on this relationship, Ogilvie et al. [51] proposed the following expression for the average settling velocity of 2D nanosheets:

$$\langle q \rangle = \frac{(\rho_p - \rho_l)k^2 \langle \mathcal{L} \rangle^m g_e}{6\pi\mu}. \quad (3.11)$$

In Eq.3.11, $\langle \mathcal{L} \rangle$ is the average layer number of the nanosheets, and k is a shape factor related to the aspect ratios of the nanosheets with the dimension of length. An average and idealised value for the exponent m is 2.5, covering a broad initial distributions of $\langle \mathcal{L} \rangle$ of different 2D materials. The values of k and m can be determined by a calibration experiment [51]. Then, Eq.3.11 can be utilized to calculate the parameters needed for centrifugation (i.e. equivalent g -force and centrifugation time).

We will now explain how to use the one-dimensional model (Eq.3.4) to predict the outcome of the fractionation of nanosheets by centrifugation. Suppose nanosheets with layer number between \mathcal{L}_1 and \mathcal{L}_2 ($\mathcal{L}_1 < \mathcal{L}_2$) are desired. First, a calibration experiment can be done to acquire the values of k and m in Eq.3.11. The frequency distribution of layer number of the nanosheets (\mathcal{L}) can be obtained by atomic force microscopy (AFM). Second, the frequency distribution of the settling velocity can be obtained once the physical properties of the nanosheets (i.e. density) and solvent (i.e. density and viscosity) and the equivalent g -force used in the centrifugation are known, according to Eq.3.11. The two settling velocities q_1 and q_2 of nanosheets with layer number \mathcal{L}_1 and \mathcal{L}_2 , respectively, can be calculated. Third, the centrifugation times used in the two steps can be chosen as $t_1 = H/q_2$ and $t_2 = H/q_1$, respectively, and H is the filling height of the dispersion in the vial. After centrifuging for the duration of t_1 , the sediment can be discarded and the supernatant can be centrifuged again for t_2 , and the sediment from the second step can be collected as the fractionated sample. By solving the one-dimensional model (Eq.3.4) with corresponding parameters (i.e. the centrifugation times) and initial conditions (i.e. band or homogeneous sedimentation, initial frequency distribution), the frequency distribution of the fractionated sample can be obtained. Based on this distribution, the full statistics of the fractionated sample (e.g. range, mean value and standard deviation of the layer number) can be predicted. Finally, to increase the purity of the fractionated sample, the centrifugation time in the second step can be lowered to $t_2 = H/(q_1 + \Delta q)$. By solving the one-dimensional model, a reference map like Fig.3.16 of the impurity percentage and yield when choosing different Δq can be constructed. Then, the appropriate value of Δq to be used in the centrifugation process can be chosen based on the desired purity and yield.

Similarly, the model and corresponding experimental protocol can be used to fractionate nanosheets by lateral size. Suppose a sample of nanosheets with approximately the same thickness whereas the lateral size is log-normally distributed with mean as $0.1 \mu\text{m}$ and standard deviation as $0.1 \mu\text{m}$, to be fractionated by lateral size, and the desired range of lateral size is from $0.025 \mu\text{m}$ to $0.045 \mu\text{m}$. Since the nanosheets have the same thickness, $q \sim d$ according to Eq.3.10. Therefore q also follows log-normal distribution. Take the settling velocity of a nanosheet whose lateral size is $1 \mu\text{m}$ as characteristic velocity to non-dimensionalize q , the system is converted to the one studied in Sec.5.4. If the two-step approach shown in Sec.3.4.3 is adopted to fractionate the sample, and the centrifugation time in the second step (t_2) is based on the settling velocity of the nanosheet whose lateral size is $0.025 \mu\text{m}$, the impurity percentage of the final product would be about 5% using band sedimentation (assuming initially the height of particle-laden layer is 10% of the vial height), and would be about 50% using homogeneous sedimentation, according to Fig.3.12(b). To lower the impurity percentage, t_2 could be lowered. For example, the impurity percentage would be 0 ideally in band sedimentation if t_2 is based on the settling velocity of the nanosheet whose lateral size is $0.02778 \mu\text{m}$, and would be about 45% in homogeneous sedimentation if t_2 is based on the settling velocity of the nanosheet whose lateral size is $0.035 \mu\text{m}$, according to Fig.3.13. In the meantime, the yield would decrease from 86% to 80% in band sedimentation, and would decrease from 21.5% to 19% in homogeneous sedimentation.

3.6 Conclusions

In this chapter, a mathematical model is used to study the multicascade (multistep) sedimentation or centrifugation of polydisperse particle systems with an initial log-normal size distribution, under the main assumption that the suspension is dilute. Two cases are considered: band sedimentation, where the particles are initially deposited in a small slab at the top of the clear fluid, and homogeneous sedimentation, where the particles are evenly dispersed in the vial initially. The model enables to predict the time evolution of the size frequency distributions in the supernatant and in the sediment layer, and the conditions for optimal sorting of an initial size distribution in distinct particle size classes. Fractionation of metallic nanoparticles and fractionation of graphene nanosheets are taken as examples to illustrate the practical application of the theory. The main conclusions of our analysis are as follows.

In band sedimentation, the frequency distribution curves in the supernatant and in the sediment layer overlap only slightly at each time (see Fig.3.7(a)), meaning there is a clear distinction between the size classes in the supernatant and in the sediment layer. Therefore, in the absence of convective or diffusive mixing, band sedimentation

is preferable over homogeneous sedimentation to fractionate particles by size. In applications where the purity of the sample is paramount, therefore, band sedimentation could offer significant advantages. The main drawback of band sedimentation is the lower yield and the fact that, in practice, it is more difficult to controllably place a layer of particle-rich fluid over the clear fluid without incurring in gravitational instabilities that lead to fluid mixing. Methods to overcome this practical issue are using solvent with density gradient [55] and adding a buffer layer liquid between the suspension and clear fluid [56]. Given the significant advantages of band sedimentation in terms of purity, new methods to prevent mixing when using band sedimentation should be investigated in the future.

To answer the research question proposed in chapter 1, we have proposed and analyzed a rational protocol to isolate a certain particle size range. The protocol, described in Sec. 3.4.3, involves two characteristic centrifugation or sedimentation times: $t_{\min} = H/q_{\max}$ and $t_{\max} = H/q_{\min}$, where H is the height of the free surface of the liquid with respect to the bottom of the vial, q_{\max} is the velocity of the largest (fastest) particles and q_{\min} is the velocity of the smallest (slowest) particles. The protocol involves sedimenting or centrifuging for time $t_{\min} = H/q_{\max}$, transferring the supernatant to a new vial and centrifuging for a longer time. Then the process is repeated a number of steps. In analyzing this method we have found that, surprisingly, a two-step method is not worse than a multi-step method when the objective is to isolate a given particle size range (see Fig.3.12). Therefore, to isolate a size range that lies in the middle of the size distribution, only 2 steps could be used. Furthermore, we have found that shifting the time by a small amount can lead to an even more precise selection of the size class, i.e. the attainment of a sample with reduced amount of “impurities” (particles that are selected but are not in the desired particle class). In both the initial protocol and in the improved one there is, in general, a trade-off between yield and amount of impurities.

The advantage of the methods we propose is that they are based on the equations of motion of the particles in the fluid, and therefore using the parameters of the paper will lead to exact predictions in the very dilute limit in which the sedimentation velocity of one particle does not depend on the presence of the other particles. The analysis can be used as a theoretical guideline to design or modify sedimentation and centrifugation protocols for more realistic situations where the suspension is not truly dilute. For instance, we envision application in the fractionation of graphene particles, and have provided practical guidelines for this case (see Sec. 3.5.2).

The digitalisation of laboratory procedures means that exact algorithms will be required to replace choices based on empiricism, so the availability of exact formulas and accurate quantitative predictions for centrifugation/sedimentation will become increasingly useful, both in analytical laboratories and in plant operations. In the future, we will investigate with the help of high-resolution, particle-resolved simulations how

well the dilute theory is able to describe the evolution of the size distribution when the suspension is not so dilute that hydrodynamic interactions can be neglected and the flow microphysics leading to convective mixing in band sedimentation/centrifugation.

REFERENCES

- [1] Jan Mewis and Norman J Wagner. *Colloidal Suspension Rheology*. Cambridge University Press, 2012.
- [2] Jungin Lee and Tayfun Babadagli. “Comprehensive review on heavy-oil emulsions: Colloid science and practical applications.” In: *Chemical Engineering Science* (2020), p. 115962.
- [3] A Abeynaike, AJ Sederman, Y Khan, ML Johns, JF Davidson, and MR Mackley. “The experimental measurement and modelling of sedimentation and creaming for glycerol/biodiesel droplet dispersions.” In: *Chemical Engineering Science* 79 (2012), pp. 125–137.
- [4] Stephen Olaribigbe Majekodunmi. “A review on centrifugation in the pharmaceutical industry.” In: *American Journal of Biomedical Engineering* 5.2 (2015), pp. 67–78.
- [5] Martin E Schimpf, Karin Caldwell, and J Calvin Giddings. *Field-flow fractionation handbook*. John Wiley & Sons, 2000.
- [6] André M Striegel and Amandaa K Brewer. “Hydrodynamic chromatography.” In: *Annual Review of Analytical Chemistry* 5 (2012), pp. 15–34.
- [7] Ji Chen, Yingru Li, Liang Huang, Naer Jia, Chun Li, and Gaoquan Shi. “Size fractionation of graphene oxide sheets via filtration through track-etched membranes.” In: *Advanced Materials* 27.24 (2015), pp. 3654–3660.
- [8] Umar Khan, Arlene O’Neill, Harshit Porwal, Peter May, Khalid Nawaz, and Jonathan N Coleman. “Size selection of dispersed, exfoliated graphene flakes by controlled centrifugation.” In: *Carbon* 50.2 (2012), pp. 470–475.
- [9] Claudia Backes, Beata M Szydłowska, Andrew Harvey, Shengjun Yuan, Victor Vega-Mayoral, Ben R Davies, Pei-liang Zhao, Damien Hanlon, Elton JG Santos, Mikhail I Katsnelson, et al. “Production of highly monolayer enriched dispersions of liquid-exfoliated nanosheets by liquid cascade centrifugation.” In: *ACS Nano* 10.1 (2016), pp. 1589–1601.
- [10] Claudia Backes, Ronan J Smith, Niall McEvoy, Nina C Berner, David McCloskey, Hannah C Nerl, Arlene O’Neill, Paul J King, Tom Higgins, Damien Hanlon, et al. “Edge and confinement effects allow in situ measurement of size and thickness of liquid-exfoliated nanosheets.” In: *Nature Communications* 5.1 (2014), pp. 1–10.

- [11] Dalal Fadil, Ridwan F Hossain, Gustavo A Saenz, and Anupama B Kaul. “On the chemically-assisted excitonic enhancement in environmentally-friendly solution dispersions of two-dimensional MoS₂ and WS₂.” In: *Journal of Materials Chemistry C* 5.22 (2017), pp. 5323–5333.
- [12] Wei Gao, Yan Zhao, and Hong Yin. “Lateral size selection of liquid exfoliated hexagonal boron nitride nanosheets.” In: *RSC Advances* 8.11 (2018), pp. 5976–5983.
- [13] Kazufumi Hosoda, Tomoaki Matsuura, Hiroaki Suzuki, and Tetsuya Yomo. “Origin of lognormal-like distributions with a common width in a growth and division process.” In: *Physical Review E* 83.3 (2011), p. 031118.
- [14] John C Thomas. “The determination of log normal particle size distributions by dynamic light scattering.” In: *Journal of Colloid and Interface Science* 117.1 (1987), pp. 187–192.
- [15] Jost Heintzenberg. “Properties of the log-normal particle size distribution.” In: *Aerosol Science and Technology* 21.1 (1994), pp. 46–48.
- [16] CG Granqvist and RA Buhrman. “Log-normal size distributions of ultrafine metal particles.” In: *Solid State Communications* 18.1 (1976), pp. 123–126.
- [17] AR Dexter and DW Tanner. “Packing densities of mixtures of spheres with log-normal size distributions.” In: *Nature Physical Science* 238.80 (1972), pp. 31–32.
- [18] Terence Allen. *Particle size measurement*. Springer, 2013.
- [19] Claudia Backes, Amr M Abdelkader, Concepción Alonso, Amandine Andrieux-Ledier, Raul Arenal, Jon Azpeitia, Nilanthy Balakrishnan, Luca Banszerus, Julien Barjon, Ruben Bartali, et al. “Production and processing of graphene and related materials.” In: *2D Materials* 7.2 (2020), p. 022001.
- [20] George J Kynch. “A theory of sedimentation.” In: *Transactions of the Faraday Society* 48 (1952), pp. 166–176.
- [21] KE Davis and W Bo Russel. “An asymptotic description of transient settling and ultrafiltration of colloidal dispersions.” In: *Physics of Fluids A: Fluid Dynamics* 1.1 (1989), pp. 82–100.
- [22] François Blanchette and John WM Bush. “Particle concentration evolution and sedimentation-induced instabilities in a stably stratified environment.” In: *Physics of Fluids* 17.7 (2005), p. 073302.
- [23] Evangelia Antonopoulou, Connor F Rohmann-Shaw, Thomas C Sykes, Olivier J Cayre, Timothy N Hunter, and Peter K Jimack. “Numerical and experimental analysis of the sedimentation of spherical colloidal suspensions under centrifugal force.” In: *Physics of Fluids* 30.3 (2018), p. 030702.

- [24] MA Al-Naafa and M Sami Selim. “Sedimentation of monodisperse and bidisperse hard-sphere colloidal suspensions.” In: *AIChE Journal* 38.10 (1992), pp. 1618–1630.
- [25] Andrew D Watson, Gary C Barker, and Margaret M Robins. “Sedimentation in bidisperse and polydisperse colloids.” In: *Journal of Colloid and Interface Science* 286.1 (2005), pp. 176–186.
- [26] Robert Dorrell and Andrew J Hogg. “Sedimentation of bidisperse suspensions.” In: *International Journal of Multiphase Flow* 36.6 (2010), pp. 481–490.
- [27] Sergei E Esipov. “Coupled Burgers equations: a model of polydisperse sedimentation.” In: *Physical Review E* 52.4 (1995), p. 3711.
- [28] Bo Xue and Yan Sun. “Modeling of sedimentation of polydisperse spherical beads with a broad size distribution.” In: *Chemical Engineering Science* 58.8 (2003), pp. 1531–1543.
- [29] Stefano Buzzaccaro, Antonio Tripodi, Roberto Rusconi, Daniele Vigolo, and Roberto Piazza. “Kinetics of sedimentation in colloidal suspensions.” In: *Journal of Physics: Condensed Matter* 20.49 (2008), p. 494219.
- [30] GK Batchelor. “Sedimentation in a dilute polydisperse system of interacting spheres. Part 1. General theory.” In: *Journal of Fluid Mechanics* 119 (1982), pp. 379–408.
- [31] MJ Uttinger, D Jung, N Dao, H Canziani, C Lübbert, N Vogel, W Peukert, J Harting, and J Walter. “Probing sedimentation non-ideality of particulate systems using analytical centrifugation.” In: *Soft Matter* 17.10 (2021), pp. 2803–2814.
- [32] Robert H Davis and Hatice Gecol. “Hindered settling function with no empirical parameters for polydisperse suspensions.” In: *AIChE Journal* 40.3 (1994), pp. 570–575.
- [33] Sanjeev Kumar, Theodore W Pirog, and Doraiswami Ramkrishna. “A new method for estimating hindered creaming/settling velocity of particles in Polydisperse Systems.” In: *Chemical Engineering Science* 55.10 (2000), pp. 1893–1904.
- [34] Micheline Abbas, Eric Climent, Olivier Simonin, and Martin R Maxey. “Dynamics of bidisperse suspensions under Stokes flows: Linear shear flow and sedimentation.” In: *Physics of Fluids* 18.12 (2006).
- [35] Richard J Larsen and Morris L Marx. *An introduction to mathematical statistics*. Prentice Hall, 2005.

- [36] Quentin A Pankhurst, J Connolly, Stephen K Jones, and JJJopDAP Dobson. “Applications of magnetic nanoparticles in biomedicine.” In: *Journal of Physics D: Applied physics* 36.13 (2003), R167.
- [37] Fars K Alanazi, Awwad A Radwan, and Ibrahim A Alsarra. “Biopharmaceutical applications of nanogold.” In: *Saudi Pharmaceutical Journal* 18.4 (2010), pp. 179–193.
- [38] José M Pingarrón, Paloma Yañez-Sedeño, and Araceli González-Cortés. “Gold nanoparticle-based electrochemical biosensors.” In: *Electrochimica Acta* 53.19 (2008), pp. 5848–5866.
- [39] Tom Hennebel, Simon De Corte, Willy Verstraete, and Nico Boon. “Microbial production and environmental applications of Pd nanoparticles for treatment of halogenated compounds.” In: *Current Opinion in Biotechnology* 23.4 (2012), pp. 555–561.
- [40] Elisabeth Guazzelli and John Hinch. “Fluctuations and instability in sedimentation.” In: *Annual Review of Fluid Mechanics* 43 (2011), pp. 97–116.
- [41] Francesco Bonaccorso, Mirco Zerbetto, Andrea C Ferrari, and Vincenzo Amendola. “Sorting nanoparticles by centrifugal fields in clean media.” In: *The Journal of Physical Chemistry C* 117.25 (2013), pp. 13217–13229.
- [42] Jonathan N Coleman, Mustafa Lotya, Arlene O’Neill, Shane D Bergin, Paul J King, Umar Khan, Karen Young, Alexandre Gaucher, Sukanta De, Ronan J Smith, et al. “Two-dimensional nanosheets produced by liquid exfoliation of layered materials.” In: *Science* 331.6017 (2011), pp. 568–571.
- [43] Min Yi and Zhigang Shen. “A review on mechanical exfoliation for the scalable production of graphene.” In: *Journal of Materials Chemistry A* 3.22 (2015), pp. 11700–11715.
- [44] Yenny Hernandez, Valeria Nicolosi, Mustafa Lotya, Fiona M Blighe, Zhenyu Sun, Sukanta De, IT McGovern, Brendan Holland, Michele Byrne, Yurii K Gun’Ko, et al. “High-yield production of graphene by liquid-phase exfoliation of graphite.” In: *Nature Nanotechnology* 3.9 (2008), pp. 563–568.
- [45] Umar Khan, Arlene O’Neill, Mustafa Lotya, Sukanta De, and Jonathan N Coleman. “High-concentration solvent exfoliation of graphene.” In: *Small* 6.7 (2010), pp. 864–871.
- [46] Zheling Li, Robert J Young, Claudia Backes, Wen Zhao, Xun Zhang, Alexander A Zhukov, Evan Tillotson, Aidan P Conlan, Feng Ding, Sarah J Haigh, et al. “Mechanisms of liquid-phase exfoliation for the production of graphene.” In: *ACS Nano* 14.9 (2020), pp. 10976–10985.

- [47] Arlene O'Neill, Umar Khan, and Jonathan N Coleman. "Preparation of high concentration dispersions of exfoliated MoS₂ with increased flake size." In: *Chemistry of Materials* 24.12 (2012), pp. 2414–2421.
- [48] Gyeong Sook Bang, Kwan Woo Nam, Jong Yun Kim, Jongwoo Shin, Jang Wook Choi, and Sung-Yool Choi. "Effective liquid-phase exfoliation and sodium ion battery application of MoS₂ nanosheets." In: *ACS Applied Materials & Interfaces* 6.10 (2014), pp. 7084–7089.
- [49] Titas Kumar Mukhopadhyay and Ayan Datta. "Deciphering the role of solvents in the liquid phase exfoliation of hexagonal boron nitride: A molecular dynamics simulation study." In: *The Journal of Physical Chemistry C* 121.1 (2017), pp. 811–822.
- [50] Shufen Wang, Bohan Tao, Songyue Yu, Chunxiang Wei, Tao Zhou, Xuan Chen, Chenliang Han, and Chao Wang. "Insight into the liquid-phase exfoliation to prepare BN nanosheets." In: *Materials Letters* 269 (2020), p. 127644.
- [51] Sean P Ogilvie, Matthew J Large, Marcus A O'Mara, Peter J Lynch, Cheuk Long Lee, Alice AK King, Claudia Backes, and Alan B Dalton. "Size selection of liquid-exfoliated 2D nanosheets." In: *2D Materials* 6.3 (2019), p. 031002.
- [52] Helio Chacham, Joyce CC Santos, Flavia G Pacheco, Diego L Silva, Rozana M Martins, Jessica P Del'Boccio, Eder M Soares, Rodrigo Altoé, Clascidia A Furtado, Flavio Plentz, et al. "Controlling the morphology of nanoflakes obtained by liquid-phase exfoliation: implications for the mass production of 2D materials." In: *ACS Applied Nano Materials* 3.12 (2020), pp. 12095–12105.
- [53] Konstantinos Kouroupis-Agalou, Andrea Liscio, Emanuele Treossi, Luca Ortolani, Vittorio Morandi, Nicola Maria Pugno, and Vincenzo Palermo. "Fragmentation and exfoliation of 2-dimensional materials: a statistical approach." In: *Nanoscale* 6.11 (2014), pp. 5926–5933.
- [54] Xiaoming Sun, Dachao Luo, Junfeng Liu, and David G Evans. "Monodisperse chemically modified graphene obtained by density gradient ultracentrifugal rate separation." In: *ACS Nano* 4.6 (2010), pp. 3381–3389.
- [55] Darrell Velegol, Shailesh Shori, and Charles E Snyder. "Rayleigh-Bérnard Instability in Sedimentation." In: *Industrial & Engineering Chemistry Research* 48.5 (2009), pp. 2414–2421.
- [56] Hans Coll and Charles G Searles. "Use of density gradients in a disk centrifuge." In: *Journal of Colloid and Interface Science* 110.1 (1986), pp. 65–72.

4

HINDERED SETTLING OF A LOG-NORMALLY DISTRIBUTED STOKESIAN SUSPENSION

In the previous chapter, the hydrodynamic interactions between particles are neglected. To quantify the effects of hydrodynamic interactions on the average and fluctuating particle settling velocities, settling velocity statistics for dilute suspensions of polydisperse spheres having a log-normal size distribution are generated from Stokesian dynamics simulations in this chapter. Meanwhile, a thorough comparison between our numerical results and predictions of existing models of the hindered settling function of each size class is made.

This chapter is based on the article:

H. Li and L. Botto. "Hindered settling of a log-normally distributed Stokesian suspension." In: *J. Fluid Mech.* 1001 (2024), A30.

4.1 Introduction

Prediction of the settling velocity of polydisperse suspensions is crucially important in applications ranging from wastewater treatment [1] to nanoparticle sorting [2], particle size characterisation [3], and sediment transport modelling [4]. Despite decades of research on the settling of polydispersed suspensions this field still offers interesting scientific problems. A central challenge that this chapter aims to address is the quantification of the settling velocity of each particle class in a suspension that is truly polydisperse, meaning that the number of classes exceeds the two or three classes that simulations [5–8] and experiments [9–11] have so far focused on. To quantify such velocity with high accuracy we perform Stokesian Dynamics simulations, in the relatively dilute regime (solid volume fraction ϕ less than 0.1) for which phenomena of particle segregation and clustering are not expected to be very important; for $\phi \ll 1$, the theory of Batchelor [12] for polydispersed suspensions should be sufficiently accurate and can be used to provide a framework for the analysis, hence the focus on the dilute regime. Furthermore, in addition to validating Batchelor’s model for non-negligible volume fractions, this chapter aims to demonstrate the accuracy of the three most used one-dimensional models for the settling velocity of each class - the Davis & Gecol model, the Masliyah-Lockett-Bassoon (MLB) model, and the polydisperse Richardson-Zaki model - in predicting the simulated settling velocity data as the particle concentration increases (these models are reviewed in Sec. 4.2). There are claims in the literature that semi-empirical models that do not take into account the full particle size distribution, such as the MLB and the polydisperse Richardson-Zaki models, are able to capture accurately the sedimentation of the suspension. However, these models have not in fact been rigorously validated; only the ability to roughly capture concentration profiles for selected parameters has been checked. Therefore it seems important to validate these models which are routinely used in practical settings [4, 13]. If such models do predict the settling velocity of some particle classes, we would like to know for which particle range they provide accurate predictions and with what error.

The particle size distributions is assumed to be a log-normal. Log-normal particle size distributions are ubiquitous in particulate systems, and the accurate prediction of the class-averaged particle velocity for log-normally distributed particles has recently become important because of the need for accurate size fractionation of micro and nanoparticles [2, 14].

Despite recent interest in the modelling of suspensions of wide and continuous size distributions [15–19], data on the settling of polydisperse suspensions with many size classes is surprisingly scarce. Physical experiments have been mostly carried out for bidisperse or tridisperse suspensions [9–11, 20, 21]. The largest size ratio between two size classes considered in these experiments was about 4, and only the velocity of

the largest size class was, in some experiments, measured (strictly speaking, in these experiments the velocity of the interface between different quasi-homogeneous particulate regions was measured, not the actual particle velocity). Numerical simulations have been carried out for bidisperse suspensions using Stokesian dynamics [5, 6, 8] and the force coupling method [7], with size ratios up to 4. In these simulations the velocity of each particle class was measured and compared with model predictions. Simulations of sedimentation of suspensions with a continuous log-normal distribution have been carried out by Vowinckel et al. [22] in a domain bounded by top and bottom walls, but in this study the velocity of each size class was not quantified.

Particle velocity statistics in the current chapter are calculated for polydisperse suspensions of non-Brownian, inertialess, low-Reynolds-number spheres of uniform mass density, having discrete particle size classes that are fitted to continuous log-normal distributions for different values of the polydispersity parameter α (see figure 4.4), defined as the ratio between the standard deviation and the mean value of the particle size distribution. The size distribution is chosen to be a log-normal, because of the recurring presence of this distribution in polydispersed particle systems [22–24]. The log-normal size distribution is discretised into up to 9 classes, with the largest size ratio between two classes being 5 (see figure 4.4). We vary the volume fraction ϕ from 0.01 to 0.1 and α in the range of 0.1 – 0.4. As a base case we include in Sec. 4.4 data for mono and bi-disperse suspensions, for which some literature information is available. In addition to mean particle velocities, the corresponding standard deviations and the shape of the particle velocity distributions are reported. This information provides a quantitative characterisation of the spread of the particle velocity around the mean as the polydispersity in particle size is increased.

To be able to compare against theoretical models, producing smooth data not affected by large statistical error is essential. This constraint has required us to average the velocity data over hundreds of simulations. To keep the simulation cost manageable while allowing us to explore a range of relevant parameters of solid concentration and polydispersity, following other authors [5–8], we produce converged particle velocity statistics by generating a large number of random particle configurations inside a triply periodic box, and ensemble-averaging over all such configurations. Despite limitations, which are discussed in Sec. 4.6, this established approach has in the past enabled fundamental insights into the relation between particle concentration and settling rate (for example, see Wang and Brady [8]). In Sec. 4.6 we compare, for selected parameters, random array simulations to dynamic simulations in which the particle microstructure is allowed to evolve in time. Differences between the two simulation approaches have been found not so large to affect the main conclusions of the chapter.

4.2 Overview of one-dimensional models for the class-averaged settling velocity

For a Stokesian suspension of polydisperse spheres grouped into m distinct particle classes, the average settling velocity of the i -th class can be written as $\langle u_i \rangle = u_{\text{St},i} h_i(\boldsymbol{\phi})$, where $u_{\text{St},i} = \frac{2}{9\mu} a_i^2 (\rho_p - \rho_f) g$ is the single-particle Stokes velocity of the i -th class, $h_i(\boldsymbol{\phi})$ is the hindered settling function of that class, and $\boldsymbol{\phi} = (\phi_1, \phi_2, \dots, \phi_m)$ is the vector of volume fractions [25]; a_i is the particle radius, μ is the fluid viscosity, and $\rho_p - \rho_f$ is the density difference between the particles and the fluid.

The literature reports several models for $h_i(\boldsymbol{\phi})$, as reviewed by Berres, Bürger, and Tory [13]. The only model that is completely based on first principles is the model of Batchelor [12], which was developed as an extension of the former theory of Batchelor for monodisperse suspensions [26]. Batchelor's formula reads

$$h_i(\boldsymbol{\phi}) = 1 + \sum_{j=1}^m S_{ij} \phi_j, \quad (4.1)$$

where S_{ij} are scalar sedimentation coefficients that are functions of the size ratio a_i/a_j for spheres of identical mass density [27] (an explicit expression for S_{ij} is given in Sec. 4.5.2). Batchelor's model is accurate to first-order in the total volume fraction $\phi = \sum_j \phi_j$ and is, therefore, in principle only valid for negligibly small values of ϕ . A semi-empirical extension of Batchelor's formula was proposed by Davis and Gecol [10] to improve the predictive capability in the regime of relatively high volume fractions. Their formula reads

$$h_i(\boldsymbol{\phi}) = (1 - \phi)^{-S_{ii}} \left(1 + \sum_{j=1}^m (S_{ij} - S_{ii}) \phi_j \right), \quad (4.2)$$

where $\phi = \sum \phi_j$ is the total volume fraction, and the coefficients S_{ij} are defined as in equation (4.1). The model is essentially an interpolation formula between an exact result (for $\phi \rightarrow 0$, equation (4.2) recovers (4.1)) and an approximate result (in the dense limit, for $m = 1$ equation (4.2) reduces to a power-law form, where the exponent $-S_{ii} = 6.55$ is numerically close to the exponent $\simeq 5$ of the well-known Richardson-Zaki's formula). The models of Batchelor and Davis & Gecol have been tested in experiments and simulations of bidisperse suspensions [7–9, 11, 21]. In experiments, the descending velocities of the interfaces separating different regions were measured. In simulations, settling velocities of the two classes were calculated. It was shown that Batchelor's model works reasonably well for dilute suspensions with ϕ within 5%, and Davis & Gecol's model can be used for also dense suspensions.

Models (4.1) and (4.2) are rarely used in practice because they contain a large number of coefficients. Simpler expressions have therefore been developed for practical predictions of the hindered settling of polydisperse suspensions. The most popular is the Masliyah-Lockett-Bassoon (MLB) model [20, 28]. The MLB model has been partially validated by comparison of predicted and experimentally measured concentration profiles following settling, starting at the initial time from a homogeneous suspension with a Gaussian particle size distribution [13, 29]. This validation is not complete, because the particle concentration at a given point in space is the sum of the concentrations of the different particle classes. Therefore, if a range of the particle size distribution makes a dominant contribution to the concentration, then an acceptably accurate prediction of the concentration profile may hide errors in the prediction of the velocity of certain particle classes. Furthermore, validation of the settling rates predicted by the MLB model for more than three size classes has not been published.

The MLB model reads

$$h_i(\boldsymbol{\phi}) = (1 - \phi)^{n-1} \left(1 - \sum_{j=1}^m \left(\frac{a_j}{a_i} \right)^2 \phi_j \right), \quad (4.3)$$

where a_j/a_i is the ratio of the radii of the j -th and the i -th species. Appendix B contains details of the derivation of the MLB model, so that the model assumptions can be evaluated. The function $\left(1 - \sum_{j=1}^m \left(\frac{a_j}{a_i} \right)^2 \phi_j \right)$ is the hindered settling function obtained by including the effect of volume fraction on the fluid-solid slip velocity (a continuity effect), and neglecting the effect of hydrodynamic interactions on the drag force experienced by each particle. The prefactor $(1 - \phi)^{n-1}$ incorporates the effect of hydrodynamic interactions.

An even simpler model, which has been adopted by some authors [11, 22, 30, 31], is based on the model of Richardson and Zaki [32] for monodisperse suspensions. It reads

$$h_i(\boldsymbol{\phi}) = (1 - \phi)^n, \quad (4.4)$$

where $n \approx 5$ [33]. This model predicts different velocities for different particle radii a_i , because h_i contains the single-particle Stokes formula at denominator. In the current chapter, this hindered settling formula will be referred to as Richardson-Zaki's model for polydispersed suspensions.

4.3 Numerical approach and validation

Consider a polydisperse suspension of N spheres having the same density but different radii. The N spheres are divided into m size classes. The radius of size class

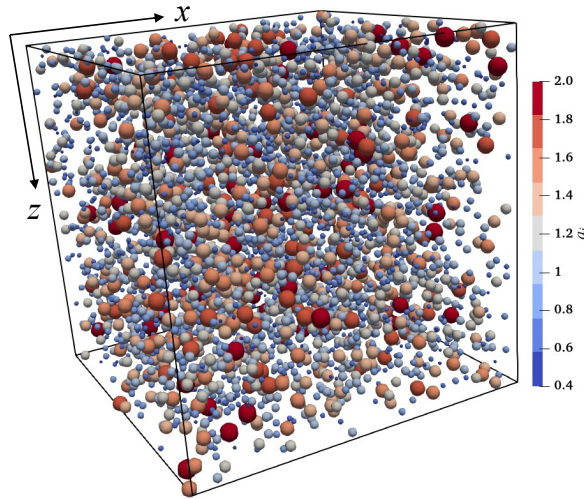


Figure 4.1: A configuration for volume fraction $\phi = 0.05$ and polydispersity parameter $\alpha = 0.4$. The spheres are coloured according to their radii.

i is α_i . Each sphere in class i is subjected to a force $\mathbf{F}_i = \frac{4}{3}\pi\alpha_i^3(\rho_p - \rho_f)\mathbf{g}$, which includes the particle weight and buoyancy; ρ_p and ρ_f are the densities of the spheres and the fluid, respectively, and \mathbf{g} is the gravitational acceleration. The single-particle Stokes velocity corresponding to each class is $\mathbf{u}_{St,i} = \frac{2}{9\mu}\alpha_i^2(\rho_p - \rho_f)\mathbf{g}$, where μ is the dynamic viscosity of the fluid. In the current work, the particle velocity statistics are calculated from instantaneous random configuration of the spheres by first averaging over the particles in the computational domain and then ensemble-averaging over statistically identical configurations. Each configuration is generated by randomly placing the spheres one by one inside the computational domain, ensuring that each placement gives no overlap between the spheres [5, 8, 34] (we note that a simulation of settling under gravity of a random particle configurations is different from a simulation of uniform flow past fixed random arrays, because in the former case different particles have different velocities, while in the latter the relative velocity between the particles and the undisturbed fluid is uniform). An example of a random array configuration is shown in figure 4.1. In our coordinate system, gravity is aligned in the z direction, also referred to as vertical direction in the following. The horizontal direction corresponds to the x and y coordinates.

To calculate the velocities of individual particles, a basic version of the Stokesian Dynamics method is adopted [35, 36]. While modern grid-based particle-resolved methods could be used [37–39], the Stokesian Dynamics method is perfectly suitable for the objectives of the current chapter: it is accurate in the relevant range of particle concentrations, it allows fast simulations, and (unlike grid-based methods) it can

simulate large ratios between the largest and smallest particle radii without numerical difficulties - a feature we would like to maintain for future highly-polydisperse simulations. In the Stokesian Dynamics method, the velocities of the spheres are calculated by solving the mobility problem

$$\mathbf{U} - \langle \mathbf{u} \rangle = \mathbf{M}\mathbf{F}, \quad (4.5)$$

where \mathbf{U} is the $3N$ vector containing the velocities of the spheres, \mathbf{F} is the $3N$ vector containing the gravitational forces acting on the spheres (these forces include the particle weight and the buoyancy force), and \mathbf{M} is the $3N \times 3N$ mobility matrix [40]. In equation (4.5), $\langle \mathbf{u} \rangle$ is the average translational velocity of the suspension. In our simulations $\langle \mathbf{u} \rangle = \mathbf{0}$ because of the zero volume flux condition of batch sedimentation [13]. Note that in the current work only velocity-force coupling is considered, i.e. the stresslet and other force moments are not considered. Brady and Durlofsky [41] showed that in a sedimenting suspension the inclusion of the stresslet changes the settling rate negligibly. Because we work in the relatively dilute limit, short-range lubrication are also neglected.

The mobility matrix \mathbf{M} depends on the positions and radii of the spheres. We used the Rotne-Prager approximation for this term [42, 43]. This approximation has been shown to give accurate predictions of the sedimentation velocities of suspensions from dilute to relatively dense [41]. Triply periodic boundary conditions are applied to the simulation box. The mobility matrix is constructed using the Ewald summation technique by splitting the mobility matrix into a real-space part and a wave-space part [44]. Explicit formulae for the mobility matrix for a polydisperse suspension can be found in Beenakker [44] and Hase and Powell [45]. As characteristic length and velocity scales, we choose the mean particle radius $\langle a \rangle$ and the single particle Stokes velocity corresponding to $\langle a \rangle$. To make forces non-dimensional we use the effective weight of the mean particle, $\frac{4}{3}\pi\langle a \rangle^3(\rho_p - \rho_f)g$.

In figure 4.2, numerical predictions for a single sphere in a triply periodic cubic box are plotted against Hasimoto's analytical solution [46] and the simulation results of Brady et al. [35]. The volume fraction of the simple cubic array is varied by varying the size of the box. Based on the point-force assumption, Hasimoto [46] derived $u/u_{St} = 1 - 1.7601\phi^{1/3}$ for $\phi \ll 1$, where u_{St} is the Stokes velocity of the sphere. Brady et al. [35] used Stokesian Dynamics with different approximations for the mobility matrix. The results of Brady et al. [35] shown in figure 4.2 correspond to simulations in the Rotne-Prager approximation. As seen from figure 4.2, our results match exactly those of Brady et al. [35] and converge to Hasimoto's solution for $\phi \rightarrow 0$. This test validates our implementation of the Ewald summation for the periodic boundary conditions.

In figure 4.3, the normalized relative settling velocity is shown as a function of the normalized centre-to-centre distance between two unequal spheres with size ratio 2 and 5, respectively. In our simulations, the radius of the large sphere is fixed to $a_l = 2$.

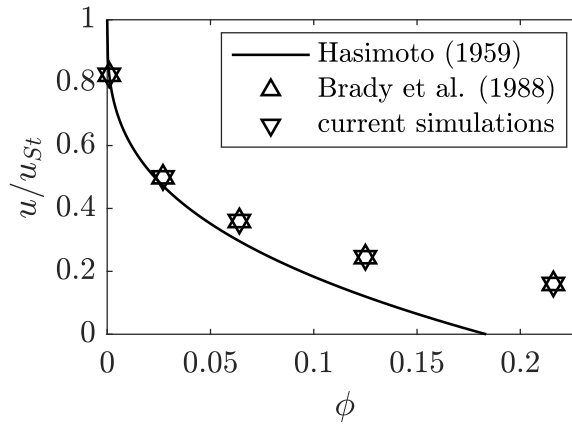


Figure 4.2: Normalized settling velocity vs. volume fraction for a simple cubic array of monodisperse spheres. The line is the point-force solution of Hasimoto [46]. Upward triangles are the numerical results of Brady et al. [35].

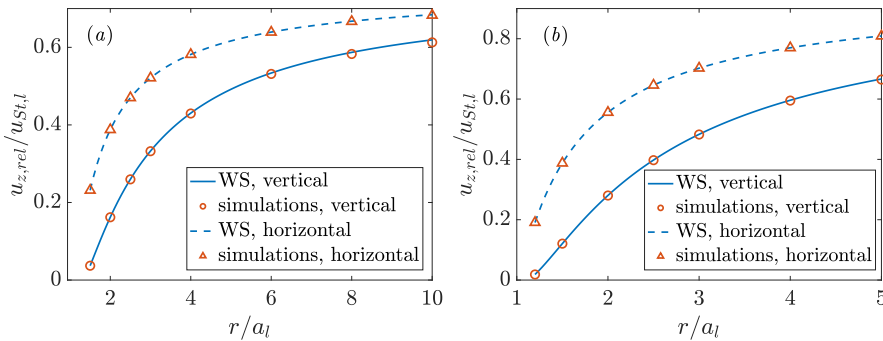


Figure 4.3: Normalized relative settling velocity for a pair of spheres as a function of the centre-to-centre distance for (a) size ratio 2 and (b) size ratio 5. Results of current simulations are shown as symbols, and analytical results of Wacholder and Sather [47] are shown as lines.

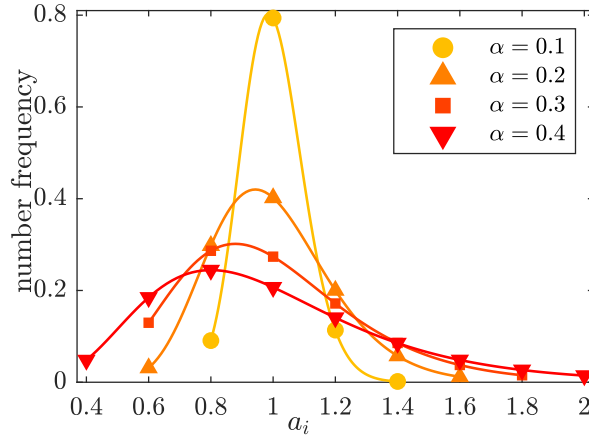


Figure 4.4: Discrete frequency distributions of particle size for different values of the polydispersity parameter (symbols). Lines indicate the continuous log-normal distributions that fit the discrete frequency histograms.

The radius of the small sphere is $a_s = 1$ and 0.4 for size ratio 2 and 5 , respectively (these values are chosen because the largest radius is 2 and the largest size ratio is 5 in the polydisperse simulations analysed in this chapter). The relative settling velocity between the two spheres is normalized by the Stokes velocity of the large sphere. The centre-to-centre distance is normalized by the radius of the large sphere. In figure 4.3, symbols are results from our simulations, and lines correspond to the asymptotic solution of Wacholder and Sather [47], in which only far-field hydrodynamic interactions were considered. It can be seen that our results match the analytical solution for both vertically and horizontally aligned pairs.

The current chapter discusses results for bidisperse suspensions and polydisperse suspensions with more than two classes, also comparing with the monodisperse case. For the monodisperse case, the radius of the spheres is $a = 1$. For the bidisperse case, two size ratios are considered: $a_2/a_1 = 2$ and 5 . The radii of the small size classes are $a_1 = 0.8$ and 0.4 for these two size ratios, respectively. The volume fraction of the small size class is $\phi_1 = \frac{3}{11}\phi$ for size ratio 2 , and $\phi_1 = \frac{1}{76}\phi$ for size ratio 5 . These volume fraction ratios are chosen so that the average radius of the spheres is equal to 1.0 for each system.

For the simulations with several size classes, the particle size distribution follows $p(a) = \frac{1}{a\sigma\sqrt{2\pi}}e^{-(\ln a - \mu)^2/2\sigma^2}$, where the mean value of the size distribution is $\langle a \rangle = e^{\mu + \sigma^2/2}$ and the standard deviation is $\Delta a = \sqrt{(e^{\sigma^2} - 1)e^{2\mu + \sigma^2}}$. We define the *polydispersity parameter* as $\alpha = \Delta a / \langle a \rangle$. Four size distributions are considered, with $\langle a \rangle = 1$ and $\alpha = 0.1, 0.2, 0.3$ or 0.4 . Each distribution is cut at the two ends, resulting in a range $a_{\min} \leq a \leq a_{\max}$, where a_{\min} and a_{\max} are chosen so that

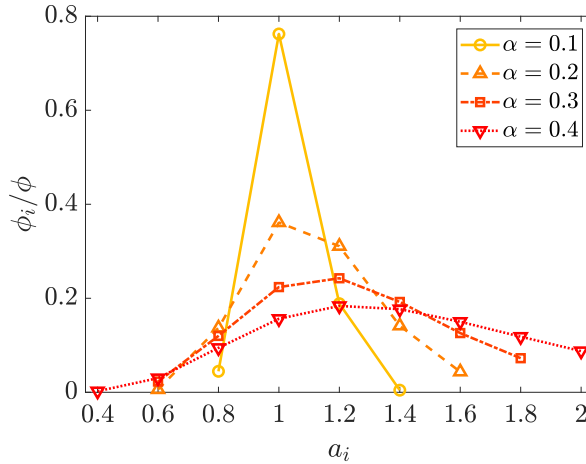


Figure 4.5: Volume fraction distributions for different values of α .

at least 95% of the original distribution falls within this range. The largest size ratio between two spheres is 5. Each radius range is discretized into between 4 and 9 size classes, with a difference of 0.2 between the radii of two adjacent size classes.

The discrete number frequency distributions are overlaid on the corresponding continuous distributions in figure 4.4. The frequency of size class i is calculated as $\frac{p(a_i)}{\sum_{j=1}^m p(a_j)}$. The corresponding volume fraction distributions are shown in figure 4.5. For each value of α , the volume fraction ϕ ranges from 0.01 to 0.10. For each simulated case, corresponding to a combination of α and ϕ , a fixed box size $L = 80$ is used and 500 random particle configurations are generated. The total number of spheres in each case varies from 925 to 12223. We have verified that increasing the size of the computational domain beyond $L = 80$ does not change the magnitude of the results significantly. As an example, in figure 4.6 we show the velocities of three size classes (for $\phi = 0.03$ and $\alpha = 0.4$) as a function of L .

The average velocity of class i is calculated by ensemble-averaging over M configurations as

$$\langle \bar{u}_{\xi,i} \rangle = \frac{\sum_{k=1}^M \bar{u}_{\xi,i}^k}{M}, \quad (4.6)$$

where $\xi = 1, 2, 3$ correspond to the three Cartesian coordinates, $\bar{u}_{\xi,i}$ is the intrinsic volume average of the velocity component $u_{\xi,i}$ within one configuration, and $\langle \cdot \rangle$ is the ensemble-averaging operator. The intrinsic volume average within class i over configuration k is $\bar{u}_{\xi,i}^k = \frac{\sum_{l=1}^{N_i} u_{\xi,i,l}^k}{N_i}$, where N_i is the number of particles in class i . The standard deviation of a certain velocity component within one realisation is calculated as $(u'_{\xi,i})^k = \sqrt{\frac{\sum_{l=1}^{N_i} (u_{\xi,i,l}^k - \bar{u}_{\xi,i}^k)^2}{N_i - 1}}$. Averaging over many realisations gives

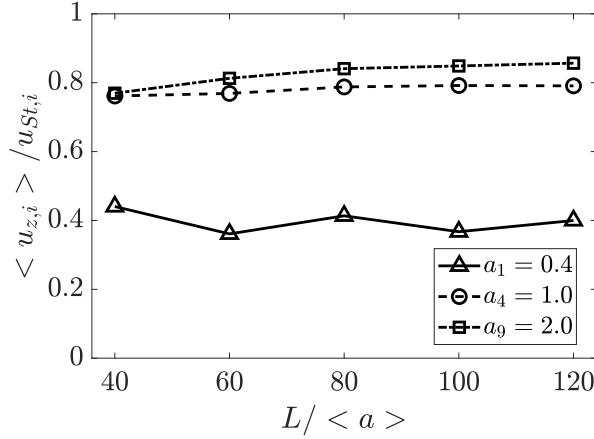


Figure 4.6: Normalized average settling velocity versus domain size for three selected size classes ($\phi = 0.03$ and $\alpha = 0.4$).

an improved estimate of the class-averaged standard deviation. In the bulk of the chapter we indicate averages by the bracket symbol, distinguishing between volume and ensemble average when necessary.

4.3.1 Relation between the mobility formulation and Batchelor's formula

In this section we show the connection between the mobility formulation, equation (4.5), and Batchelor's formula, equation (4.1). For simplicity of notation, let us consider a specific size class. Without loss of generality we consider class 1. According to (4.5) the velocity of the α -th sphere in the 1-st size class is

$$\mathbf{u}_{\alpha,1} = \sum_{i=1}^m \sum_{\beta=1}^{N_i} M_{\alpha 1, \beta i} \mathbf{F}_i, \quad (4.7)$$

where N_i is the number of spheres in the i -th class, and $M_{\alpha 1, \beta i}$ is the 3×3 mobility matrix representing the hydrodynamic interaction between the α -th sphere in the 1-st class and the β -th sphere in the i -th class [40]. Because $M_{\alpha 1, \alpha 1} = (6\pi\mu a_1)^{-1}$, (4.7) can be written as

$$\mathbf{u}_{\alpha,1} = \mathbf{u}_{St,1} + \sum_{\beta \neq \alpha} M_{\alpha 1, \beta 1} \mathbf{F}_1 + \sum_{i \neq 1} \sum_{\beta=1}^{N_i} M_{\alpha 1, \beta i} \mathbf{F}_i. \quad (4.8)$$

The average velocity of the 1-st class in this configuration is

$$\bar{\mathbf{u}}_1 = \mathbf{u}_{St,1} + \frac{1}{N_1} \left(\sum_{\alpha} \sum_{\beta \neq \alpha} M_{\alpha 1, \beta 1} \mathbf{F}_1 + \sum_{\alpha} \sum_{i \neq 1} \sum_{\beta=1}^{N_i} M_{\alpha 1, \beta i} \mathbf{F}_i \right), \quad (4.9)$$

but because \mathbf{F}_i is constant within the same size class we can also write

$$\bar{\mathbf{u}}_1 = \mathbf{u}_{\text{St},1} + s_{11}\mathbf{F}_1 + \sum_{i \neq 1} s_{1i}\mathbf{F}_i, \quad (4.10)$$

where s_{11} and s_{1i} describe the intra-class hydrodynamic interactions (within the 1-st class) and the inter-class hydrodynamic interactions (between the 1-st and the i -th classes), respectively. These two matrices can be written as $s_{11} = (N_1 - 1)\bar{M}_{11}$ and $s_{1i} = N_i\bar{M}_{1i}$, where \bar{M}_{11} and \bar{M}_{1i} are the average two-sphere mobility matrices. Upon ensemble-averaging, the average velocity of the 1-st size class can be written as

$$\langle \bar{\mathbf{u}}_1 \rangle = \mathbf{u}_{\text{St},1} + \langle s_{11} \rangle \mathbf{F}_1 + \sum_{i \neq 1} \langle s_{1i} \rangle \mathbf{F}_i. \quad (4.11)$$

The average velocity component in the gravity direction can be written as

$$\frac{\langle u_1 \rangle}{u_{\text{St},1}} = 1 + \frac{\mathcal{G}\mu\langle s_{11} \rangle}{2a_1^2 n_1} \phi_1 + \sum_{i \neq 1} \frac{\mathcal{G}\mu\langle s_{1i} \rangle}{2a_1^2 n_i} \phi_i, \quad (4.12)$$

where the formula for the single-particle Stokes velocity is used and n_i is the number density of class i . The scalar $\langle s_{1i} \rangle$ is the component of $\langle s_{1i} \rangle$ for the velocity-force coupling in the gravity direction.

Extending equation (4.12) to a generic class i yields

$$\frac{\langle u_i \rangle}{u_{\text{St},i}} = 1 + B_{ii}(\boldsymbol{\phi})\phi_i + \sum_{j \neq i} B_{ij} \left(\boldsymbol{\phi}, \frac{a_j}{a_i} \right) \phi_j. \quad (4.13)$$

The dependence of B_{ii} and B_{ij} on the volume fraction vector $\boldsymbol{\phi}$ comes from the fact that $\langle s_{ij} \rangle$ depends on the pair distribution functions, and the pair distribution functions in turn depend on the volume fraction of each class. The dependence of B_{ij} on a_j/a_i comes from the dependence of the two-sphere mobility matrix on the size ratio. For $\phi \rightarrow 0$, B_{ii} is a constant and $B_{ij} = S_{ij}$ is only a function of a_j/a_i . In this limit, equation (4.13) recovers Batchelor's expression (4.1).

4.4 Hindered settling of monodisperse and bidisperse suspensions

To build confidence in the ability of the numerical method to predict settling data in more complex situations, we compare our simulations against settling models for monodisperse and bidisperse suspensions. For the monodisperse case, the comparison also provides a validation of our numerical approach. Indeed, the empirical or semi-analytical models are well established in their regime of validity: the Richardson-Zaki

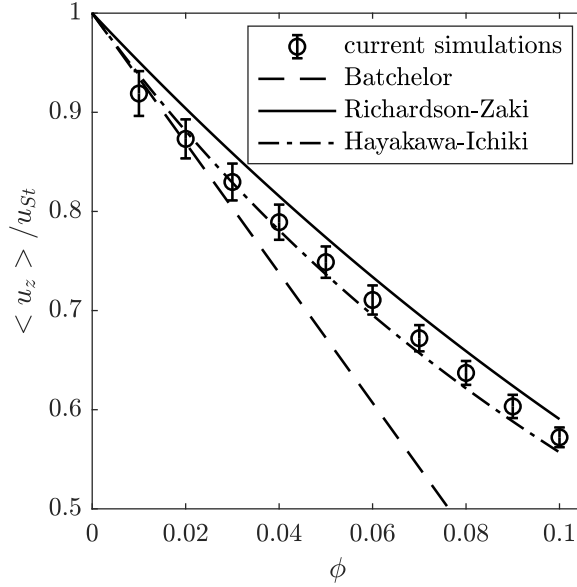


Figure 4.7: Monodisperse case: average settling velocity, normalized by the single-particle Stokes velocity, versus volume fraction

correlation summarises experimental data obtained by these authors, and its validity has been confirmed in numerical simulations [6, 7] and independent experiments [48]; the analytical model of Batchelor for monodispersed suspensions is exact for $\phi \ll 1$ [25]; Hayakawa-Ichiki's model has been favourably compared against monodisperse simulations for a wide range of volume fractions [49].

The normalised average settling velocity $\langle u_z \rangle / u_{St}$ for the monodisperse suspension is plotted in figure 4.7 as a function of ϕ . We include in the plot the Richardson-Zaki correlation $(1 - \phi)^n$ [32] for $n = 5$, the Batchelor model $1 + S\phi$ [26] assuming $S = -6.55$ and the Hayakawa-Ichiki model $\frac{(1-\phi)^3}{1+2\phi+1.429\phi(1-\phi)^3}$ [50]. The values chosen for the exponent n and the coefficient S here are typically for non-Brownian particles interacting only hydrodynamically [49, 51].

Our simulation results agree with Batchelor's model for ϕ approximately smaller than 0.03. For larger volume fractions, the simulation gives larger values than Batchelor's model. A similar range of validity for Batchelor's model was also found by Abbas et al. [7] using a force-coupling method. Our results also agree well with the Hayakawa-Ichiki model for $\phi \leq 0.05$ and they lie between the predictions of Richardson-Zaki's correlation and Hayakawa-Ichiki's model for $\phi \geq 0.06$. The simulation data for $\phi = 0.01$ is smaller than the values predicted by the three models. This is expected because of the use of triply-periodic boundary conditions in a domain of finite size [52].

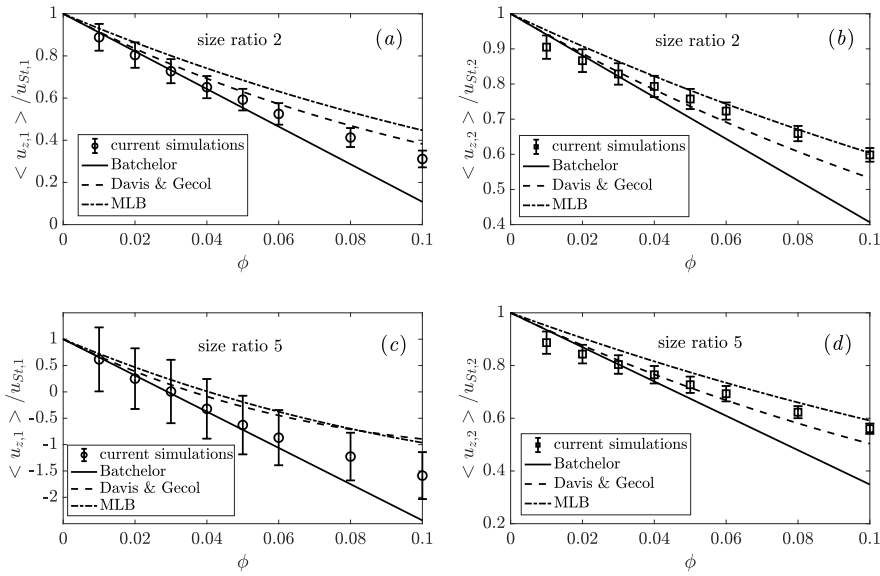


Figure 4.8: Bidisperse case: average settling velocity normalized by the single-particle Stokes velocities for the small (left panels) and large (right panels) particles. Panels (a) and (b) are for size ratio 2. Panels (c) and (d) are for size ratio 5.

Normalised average settling velocities for the small and the large particles in the bidisperse case are plotted as symbols in figure 4.8 for two size ratios. The predictions of Batchelor's model (equation (4.1)), Davis & Gecol's model (equation (4.2)) and the MLB model (equation (4.3)) are indicated by lines. It is seen from figure 4.8 (a) and (c) that our results for the small particles agree with the predictions of Batchelor's model for $\phi \leq 0.05$, and lie between the predictions from Batchelor's model and Davis & Gecol's models for $\phi \geq 0.06$. For the large particles, our results agree with predictions from Batchelor's model for $\phi \leq 0.03$ and lie between the predictions from Davis & Gecol's and MLB models for $\phi \geq 0.04$. Stokesian dynamics calculations by Wang and Brady [8] that include stresslet and lubrication contributions also predicted for ϕ larger than around 0.05 hindered settling velocities smaller and larger than those of Davis & Gecol's for the small and the large particles, respectively. Our results of the bidisperse case are therefore in line in term of trends with those of Wang and Brady [8].

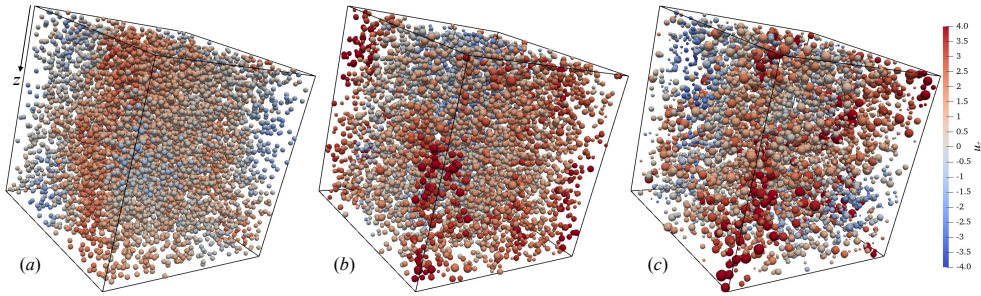


Figure 4.9: Configuration for different polydispersity parameters and $\phi=0.05$, with the spheres coloured according to their settling velocity; (a) $\alpha=0$, (b) $\alpha=0.2$, and (c) $\alpha=0.4$.

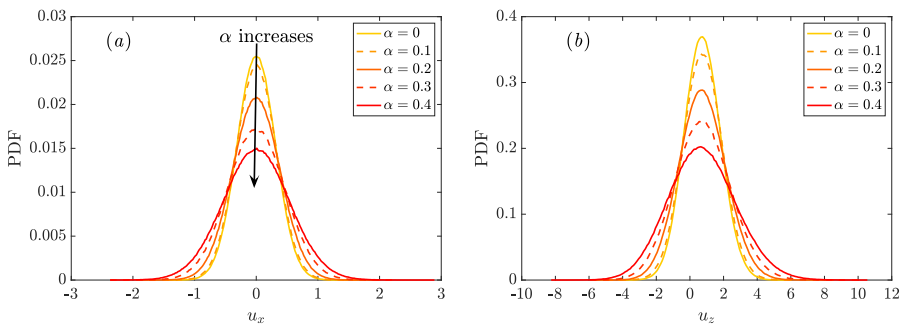


Figure 4.10: Probability distribution functions of (a) horizontal and (b) vertical velocities for different polydispersity parameters and $\phi=0.05$.

4.5 Polydisperse suspensions

4.5.1 Velocity statistics

Before delving into the analysis of the mean settling velocity, we analyse the probability distribution of particle velocities in the polydisperse particle simulations. This information enables a characterisation of the statistical representativeness of the mean values. To illustrate the spatial distribution of particle velocities, in figure 4.9 we show snapshots of the simulations with each sphere coloured according to its settling velocity. Spheres coloured in red have settling velocities in the direction of gravity whereas spheres coloured in blue have settling velocities opposite to gravity. Figure 4.9 (c) shows that the smaller particles can move against gravity, and have negative velocities comparable in magnitude to the positive settling velocity of the largest particles.

Probability distribution functions (PDFs) of horizontal and vertical velocities, shown in figure 4.10 for different values of α , are approximately Gaussian, with a variance that increases as α increases. These PDFs are constructed by considering all

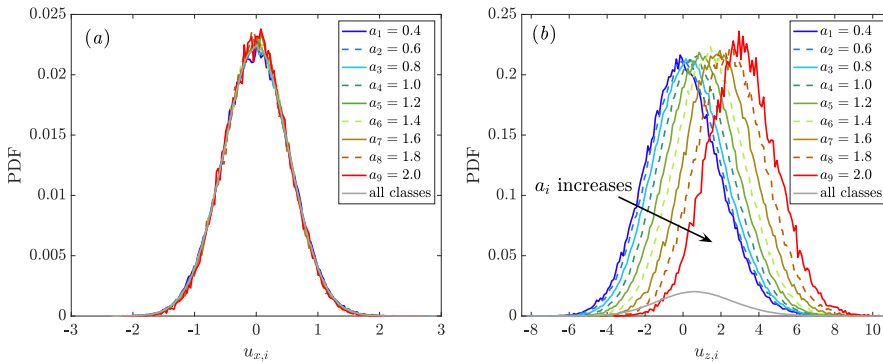


Figure 4.11: Probability distribution functions of (a) horizontal and (b) vertical velocities for $\alpha=0.4$ at $\phi=0.05$. In contrast to Fig. 4.10, here the PDFs are calculated based on the distribution of velocities within each size class.

the particles in the simulation domain. However, spheres belonging to the same size class also have a distribution of settling velocities. Therefore, in figure 4.11, we show the PDFs of the horizontal and the vertical velocities of spheres in each size class for $\alpha=0.4$. For comparison, the PDFs of the velocities of all the spheres are included in this plot as grey lines. Again, the PDFs are approximately Gaussian (simulations by Cheng and Wachs [34] of uniform flow past fixed polydisperse random arrays indicate also a Gaussian distribution for the hydrodynamic forces of a given size class). Surprisingly, the PDFs of the horizontal velocities for different size classes collapse onto a single curve (figure 4.11 (a)). From the PDFs of the vertical velocities in 4.11 (b), it is seen that the mean velocity increases as the size of the particle increases, and different size classes have comparable variances.

The average vertical settling velocity of each size class normalized by the corresponding single-particle Stokes velocity is shown in figure 4.12 for different values of α . The inset shows a zoom in the range $0.8 \leq \alpha_i \leq 2$. Because now the settling velocity is normalised by the single-particle settling velocity, the information in this plot complements the data of figure 4.11 (b). We see that for fixed α the normalized average settling velocity increases as the particle size increases. This means that the velocities of small particles are more hindered than the velocities of large particles. For a given size class, the normalized average settling velocity decreases as α increases, and decreases faster for small particles than for large particles. The standard deviation around the mean seems to decrease with α_i , except for values near $\alpha_i = 1.4$ (we have examined the velocity probability distributions of several configurations and found no probability distributions with atypical behaviour of the $\alpha_i = 1.4$ class; no simple explanation was found for this anomalous data point).

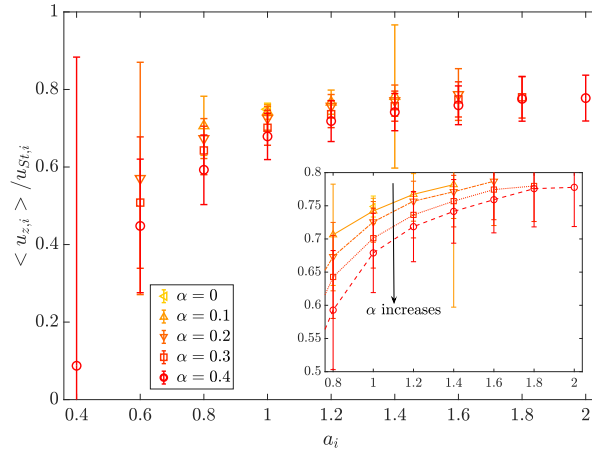


Figure 4.12: Normalized average settling velocity of each size class for different polydispersity parameters and $\phi=0.05$. The inset is a zoom in the range $0.8 \leq a_i \leq 2$. The lines are guides for the eyes.

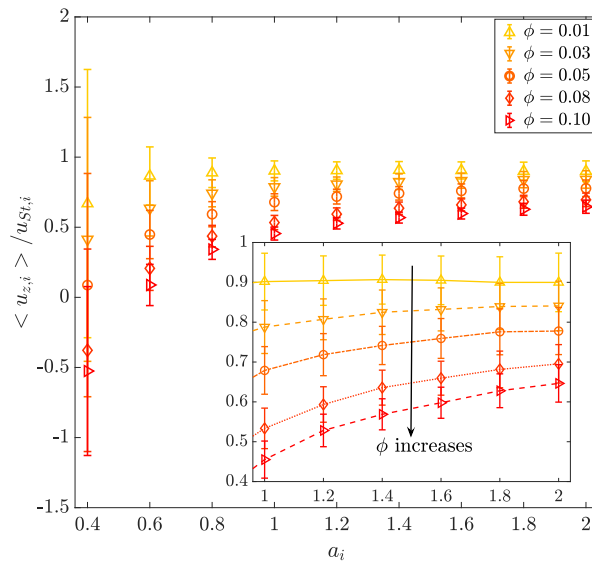


Figure 4.13: Normalized average settling velocities of each size class, for $\alpha=0.4$ and different volume fractions. The inset shows a zoom in the range $1 \leq a_i \leq 2$.

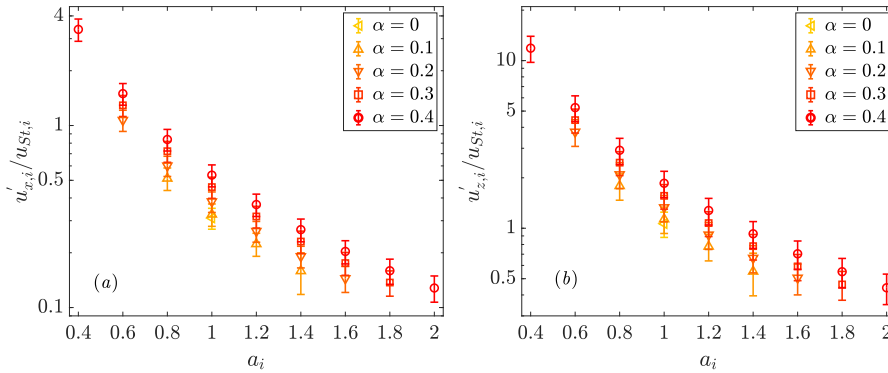


Figure 4.14: Normalized (a) horizontal and (b) vertical velocity fluctuations for different α and $\phi=0.05$.

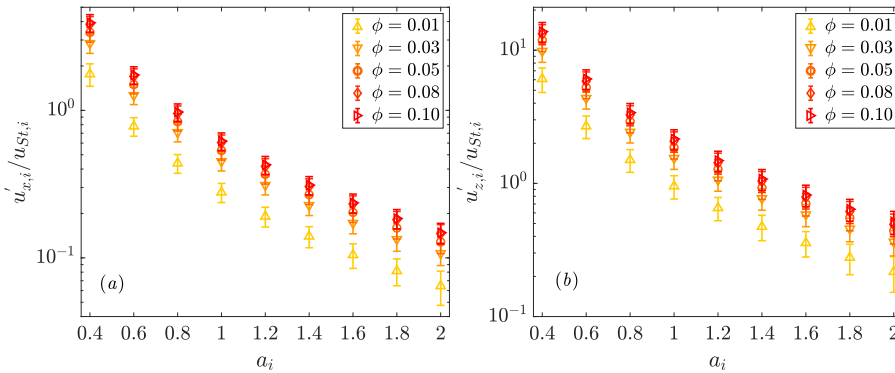


Figure 4.15: Normalized (a) horizontal and (b) vertical velocity fluctuations for different ϕ and $\alpha=0.4$.

In the previous figures, the total volume fraction was fixed, and α was changed. In figure 4.13, we instead change ϕ for fixed $\alpha=0.4$. This plot confirms the trend seen in figure 4.12: for a given volume fraction, the normalized average settling velocity decreases as the particle size decreases. The normalized average settling velocity decreases faster with increasing ϕ for small size particles.

To summarise, the smaller particles are more hindered and more affected by polydispersity than the large ones.

Statistical deviations with respect to the mean particle velocity, as measured by the root-mean square of the velocity fluctuation, increase as α or ϕ increase (see figures 4.14 and 4.15). The normalized horizontal and vertical velocity fluctuations of each size class are shown for $\alpha = 0.2$ and 0.4 with fixed $\phi = 0.05$ in figure 4.16. For a fixed

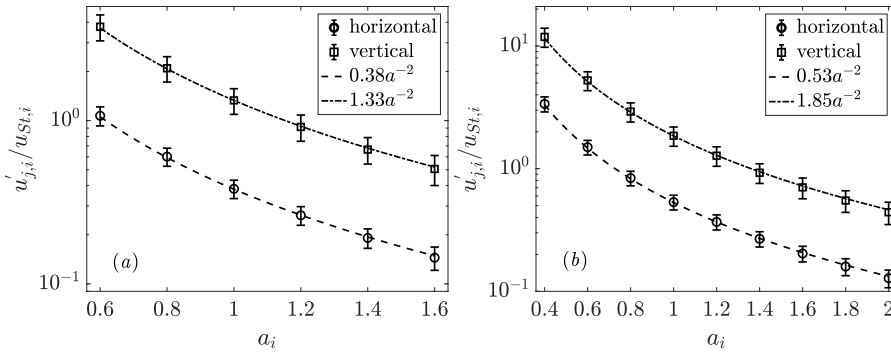


Figure 4.16: Normalized velocity fluctuations of each size class at $\phi = 0.05$ for (a) $\alpha = 0.2$ and (b) $\alpha = 0.4$.

α	horizontal direction	vertical direction
0.1	0.32	1.13
0.2	0.38	1.33
0.3	0.46	1.56
0.4	0.53	1.85

Table 4.1: Approximate values of the prefactor c in the scalings of the horizontal and the vertical normalized velocity fluctuations for each α at $\phi = 0.05$.

α , the normalized velocity fluctuations decrease as the particle size increases. Figure 4.11 seems to suggest that the velocity fluctuations are approximately independent of the particle radius a_i . Because the Stokes velocity scales as a_i^2 , it is expected that the velocity fluctuations normalized by the Stokes velocity scale as $\sim a_i^{-2}$. Our data confirm this scaling (see lines in figure 4.16): $u'_{j,i}/u_{St,i} = ca_i^{-2}$ fits the data for all the values of α and ϕ simulated, as shown in tables 4.1 and 4.2. This scaling is also observed in our simulations of bidisperse suspensions: the ratio of velocity fluctuations between the two classes in these simulations is close to 1. Peysson and Guazzelli [53] measured experimentally the velocity fluctuations of small and large particles in a dilute bidisperse suspension with size ratio 2. They found that the ratio of velocity fluctuations between the small and the large size classes were around 0.85 and 0.75 in the vertical and horizontal directions, respectively, yielding a ratio roughly close to ours.

ϕ	horizontal direction	vertical direction
0.01	0.28	0.95
0.03	0.45	1.54
0.05	0.53	1.85
0.08	0.61	2.08
0.10	0.62	2.15

Table 4.2: Same as table 4.1 but for different ϕ at $\alpha = 0.4$.

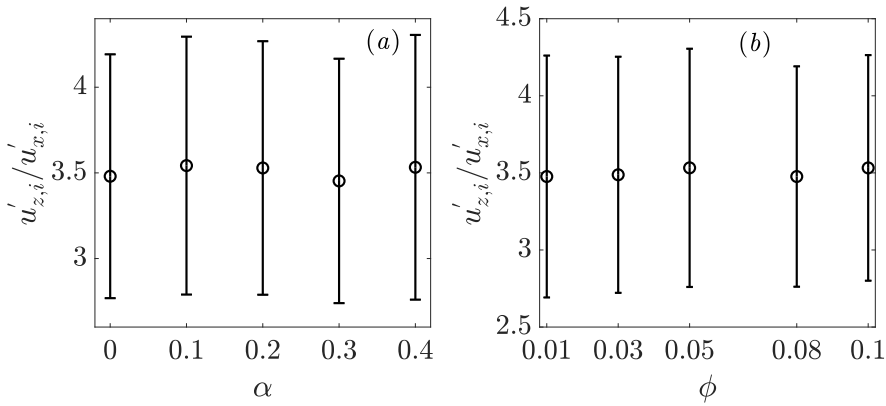


Figure 4.17: Ratio between vertical and horizontal velocity fluctuation magnitudes for $a_i = 1$ and (a) different α at $\phi = 0.05$, or (b) different ϕ at $\alpha = 0.4$.

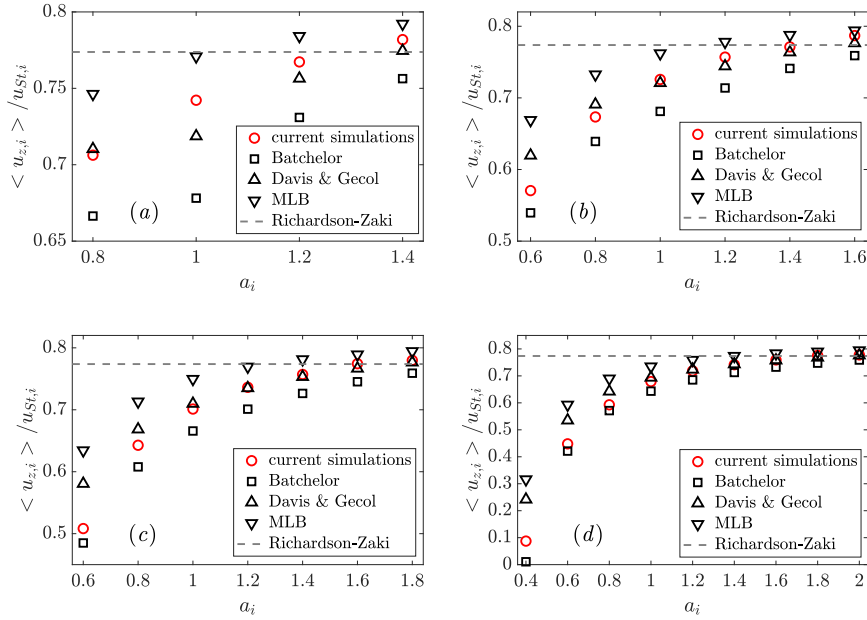


Figure 4.18: Comparison between the current simulation results and the predictions of hindered settling function models for the average velocity of different size classes, for $\phi=0.05$ and different polydispersity parameters: (a) $\alpha=0.1$, (b) $\alpha=0.2$, (c) $\alpha=0.3$ and (d) $\alpha=0.4$.

The anisotropy ratio between the vertical and the horizontal velocity fluctuations, plotted in figure 4.17, is around 3.5 regardless of the values of α or ϕ . This value was also observed in the monodisperse and bidisperse simulations.

4.5.2 Comparison with hindered settling models

In this subsection, current simulations are compared with predictions from Batchelor's (see equation (4.1)), Davis & Gecol's (see equation (4.2)) and MLB (see equation (4.3)) models. The accuracy of Richardson-Zaki correlation (see equation (4.4)) for polydisperse suspensions is also checked. The values of the coefficients S_{ij} in Batchelor's and Davis & Gecol's models are calculated from $S_{ij} = -3.50 - 1.10\lambda - 1.02\lambda^2 - 0.002\lambda^3$ where $\lambda = a_j/a_i$ [10]. The value of the exponent n in the MLB model and the Richardson-Zaki correlation is 5.

Hindered settling functions corresponding to different size classes for fixed $\phi=0.05$ and different α are compared against different theoretical models in figure 4.18. The Richardson-Zaki correlation largely overestimates the hindered settling functions of smaller particles, whereas it gives reasonable values for larger particles. The discrep-

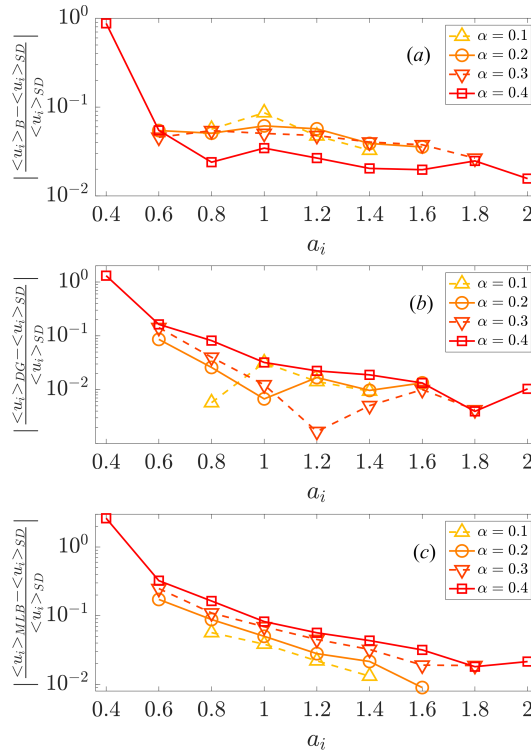


Figure 4.19: Relative differences between the average settling velocities from different models and from the current simulations for fixed $\phi = 0.05$: (a) Batchelor's model; (b) Davis & Gecol model; (c) MLB model.

ancy between the Richardson-Zaki correlation and the computed hindered settling functions of smaller particles increases as α increases. For each α , the predictions from the other three models show a consistent trend for each size class. The MLB model gives the largest settling velocities, Batchelor's model gives the smallest settling velocities, and Davis & Gecol's model gives intermediate values. The differences between the predictions from these three models get smaller as the particle size increases.

Figure 4.19 shows the normalized relative differences between the computed and predicted average settling velocities. The Batchelor model and the Davis & Gecol model predict the average settling velocity of each size class quite well for all α considered here, with relative errors smaller than 10%, except for the smallest size class $a_i=0.4$ for $\alpha=0.4$ for which the simulation gives a very small settling velocity. From figure 4.19 (c), it is seen that the relative difference between the predictions from the

MLB model and the current simulations decreases as α_i increases, or α decreases. For $\alpha_i \geq 1$, the MLB model predicts the average settling velocities quite well, with the relative difference within 10%. For $\alpha_i \leq 0.8$, the MLB model starts failing.

Hindered settling function data for fixed $\alpha=0.4$ and different ϕ are compared with the predictions from different models in figure 4.20. Also, Richardson-Zaki's correlation predicts the hindered settling functions of smaller particles poorly. For the other three models, a similar trend in the predicted values is observed as the one in the case of varying α . The predictions from the MLB model and the Davis & Gecol model are quite close to each other for all size classes at each volume fraction, and they are also quite close to the values from current simulations for larger particles. However, the Davis & Gecol model slightly underestimates the hindered settling functions of the larger particles when $\phi > 0.06$. For smaller particles, the predictions from the MLB model and the Davis & Gecol model are larger than the values from the simulations, and the discrepancies between the predictions from these two models and the values from current simulations get larger as ϕ increases. The predictions of Batchelor's model are close to the simulated values for ϕ approximately less than 0.05. As ϕ increases, Batchelor's model underestimates the hindered settling functions of all size classes systematically compared to the results of current simulations.

For fixed $\alpha=0.4$, the relative differences between the average settling velocities predicted by different models and calculated by current simulations of each size class for different volume fractions are shown in figure 4.21. For each size class, the relative difference between the prediction from the Batchelor model and the current simulations increases as the volume fraction increases, and it is within 10% when $\phi \leq 0.05$, except for the smallest size class $\alpha_i = 0.4$. From figure 4.21 (b) and (c), it is seen that the relative differences are quite close for the Davis & Gecol and the MLB models, with those of the MLB model slightly larger. For larger size classes ($\alpha_i \geq 1$), both these two models give quite accurate predictions for all volume fractions considered, with the relative differences within 10% compared to the results of current simulations. For smaller size classes ($\alpha_i \leq 0.8$), both these two models give predictions with large relative differences compared to the results of current simulations, and in general the relative difference gets larger as volume fraction increases or as size of the class decreases.

4.5.3 Velocity slip

We saw that the MLB model, despite its simplicity, gives relatively good agreement for the large particles. However, it fails for the small particles. The MLB model is based on a closure relation for the particle-fluid velocity difference (see Appendix

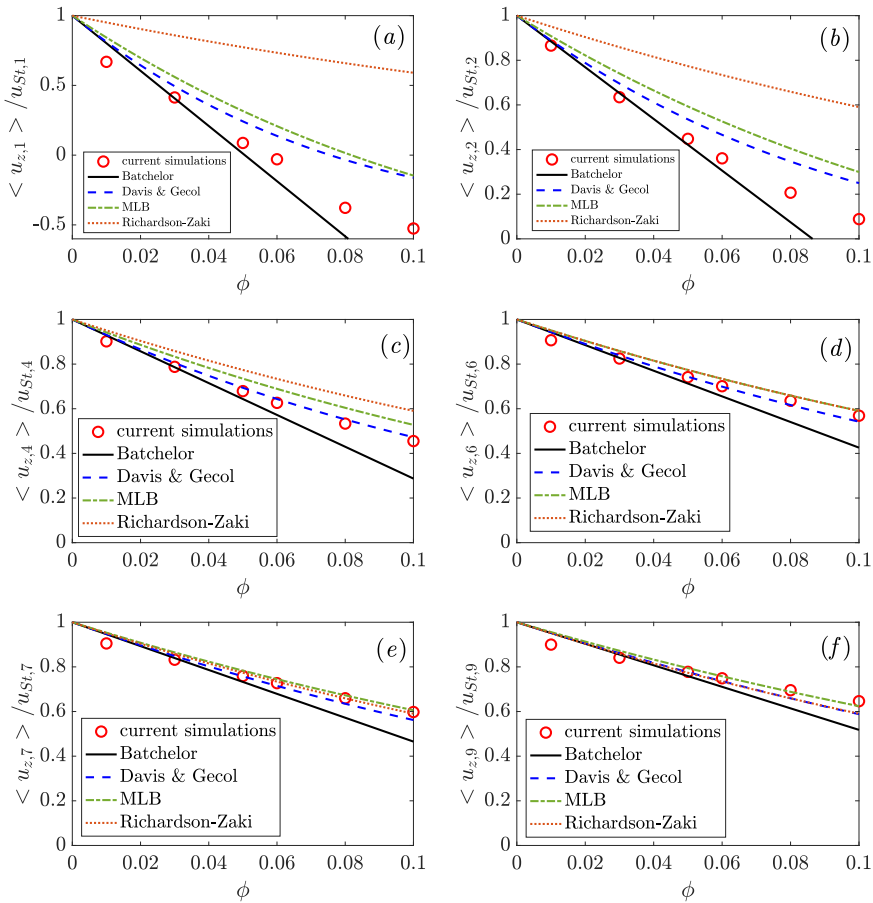


Figure 4.20: Comparison between the current numerical results and the predictions of different models. The comparison is here evaluated as a function of ϕ for fixed $\alpha=0.4$. (a) to (f) correspond to size classes a_1, a_2, a_4, a_6, a_7 and a_9 , respectively.

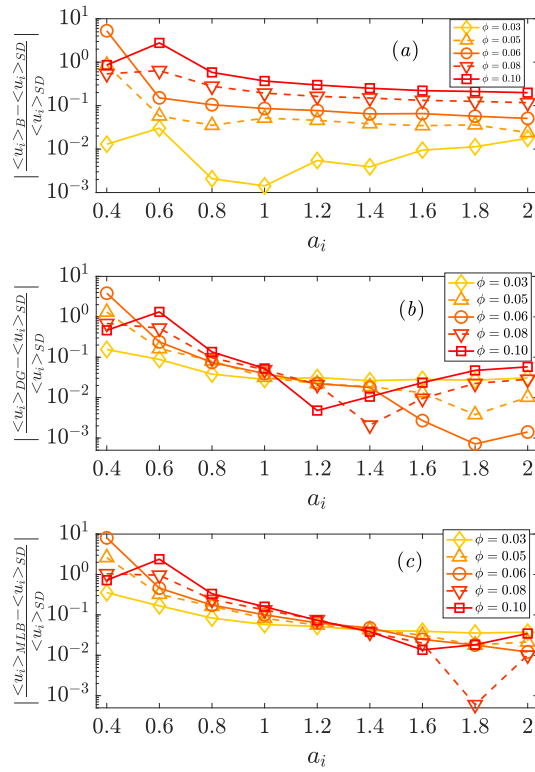


Figure 4.21: Same as in Fig. 4.19, but for different volume fractions and fixed $\alpha = 0.4$.

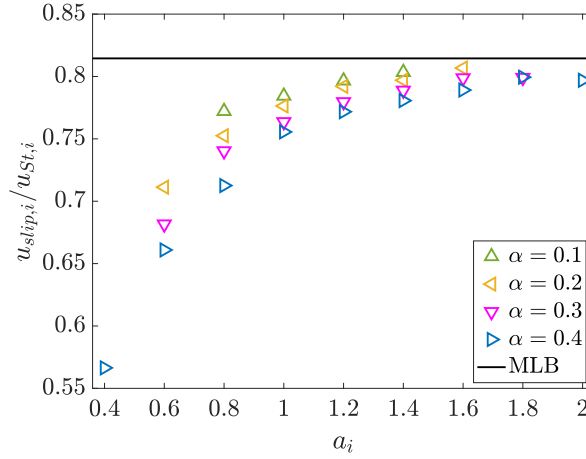


Figure 4.22: Normalized slip velocity for each size class for $\phi=0.05$ and different α . The line shows the prediction of the MLB model.

B). Therefore, to understand the limits of validity of the model, we compute the slip velocity from the simulation data and compare against the MLB model prediction.

Slip velocities for each size class normalized by the corresponding Stokes velocities are plotted in figure 4.22 for $\phi=0.05$ and different α . The slip velocity for size class i is defined as the difference between the average settling velocity of class i and the average velocity of the fluid phase,

$$\mathbf{u}_{slip,i} = \langle \mathbf{u}_{z,i} \rangle - \langle \mathbf{u}_f \rangle. \quad (4.14)$$

The value of $\langle \mathbf{u}_f \rangle$ is obtained from the zero volume-flux condition $\sum \phi_j \langle \mathbf{u}_{z,j} \rangle + (1 - \phi) \langle \mathbf{u}_f \rangle = 0$. The slip velocity predicted by the MLB model is calculated from (see Appendix B)

$$\mathbf{u}_{slip,i} = \mathbf{u}_{St,i} (1 - \phi)^{n-1}. \quad (4.15)$$

It is seen that the MLB model does not predict accurately the slip velocities of the smaller particles. The discrepancy between the MLB model prediction and the simulation data increases as α increases. The slip velocities of relatively large particles are reasonably well captured. As the particle size increases, the simulation data tends to converge to the MLB model prediction.

The normalized slip velocities for each size class for fixed $\alpha=0.4$ and varying ϕ are plotted in figure 4.23. It is seen that the prediction of the MLB model gets increasingly worse as the volume fraction increases for the small size classes. Predictions for the largest particles are instead acceptable regardless of the volume fraction.

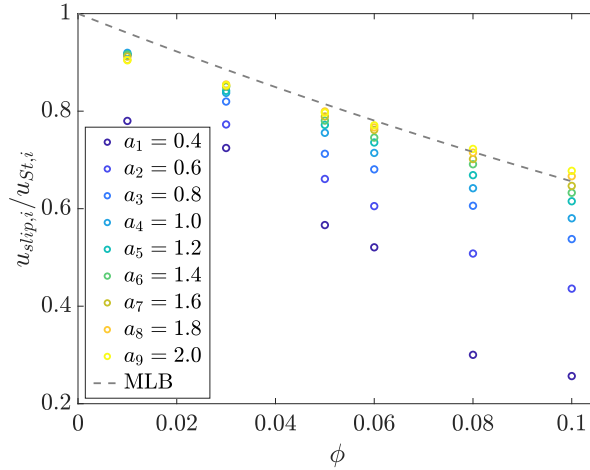


Figure 4.23: Normalized slip velocity for each size class for $\alpha=0.4$ and different values of ϕ . The dashed line is the prediction of the MLB model.

4.6 Comparison with dynamic simulations

In our simulations, we ensemble-average over random particle configurations. This approach has been used by several authors, leading to quantitative predictions such as the average sedimentation velocities and velocity fluctuations of the particles in monodisperse and bi-disperse suspensions [5–8]. Phenomena of particle clustering or segregation could in principle be important in our simulations. Regarding segregation, Batchelor and Janse Van Rensburg [54] have proven that in settling polydisperse suspensions of spheres having the same density but different radii, particle class segregation (i.e. the tendency of particles of the same class to accumulate in specific locations) does in general not occur (the polydisperse suspension is practically homogeneous). Furthermore, in our range of parameters the suspension is dilute and phenomena of particle clustering (regardless of the class the particles belong to) are expected not to be dominant features.

To assess the validity of our simulation approach, we have carried out selected dynamic simulations. For these simulations, we chose a domain size $L = 56$, a volume fraction 0.05 and $\alpha = 0.4$. Initially the particles are randomly distributed. In the dynamic simulations, at each time step the particle velocities are calculated from equation (4.5) and the particle positions are updated by a two-step, explicit method. The settling velocity of the suspension is shown as a function of time in figure 4.24.

The normalized average settling velocities of each size class from dynamic simulations and random arrays are plotted in figure 4.25 (instantaneous results from dynamic simulations are time-averaged over $500 \leq t \leq 1000$). Differences between the hin-

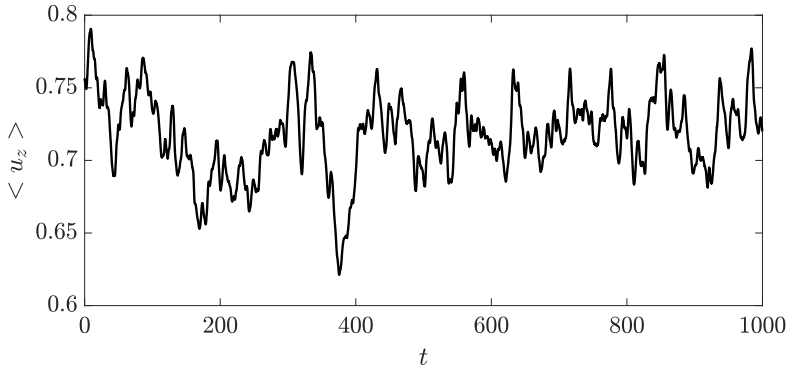


Figure 4.24: Dynamic simulation: settling velocity of the suspension, averaged over all the particles, as a function of time.

dered setting functions in the dynamic simulation and random arrays are visible. The particle velocity is seen to be slightly smaller in dynamic simulations than that in the random array simulations, except for the two size classes $\alpha_i = 0.6$ and $\alpha_i = 0.8$ where the reverse is true. However, the differences are comparatively small and the trends of the dynamic and static simulations are identical. The PDFs of the horizontal velocities of spheres in each size class from the dynamic simulation are shown in figure 4.26. Most of the PDFs collapse onto each other, as in the random array case, except the PDFs of larger size classes which show some relatively minor deviations. In figure 4.27, the pair distribution functions between the smallest and the largest size classes are plotted for both dynamic simulations and the random array simulations. Despite the statistical noise (which is more severe in polydisperse simulations than in monodisperse simulations due to the smaller number of particles per size class), the two pair distributions appear quantitatively similar. Strong clustering in the dynamic simulations would lead to pair distribution function values significantly larger than 1 for close interparticle distances. Instead, the values of the pair distribution functions at close separations are similar in range to those of the static simulations, and do not exceed 1.05. The results of the current section suggest that in our range of parameters phenomena of clustering, if present, are not sufficiently strong to affect the results presented in the current chapter.

4.7 Summary and discussion

The hindered settling function for non-Brownian, inertialess, dilute suspensions of polydisperse spheres with a log-normal size distribution was quantified via Stokesian Dynamics simulations, considering the effects of the polydispersity parameter α and

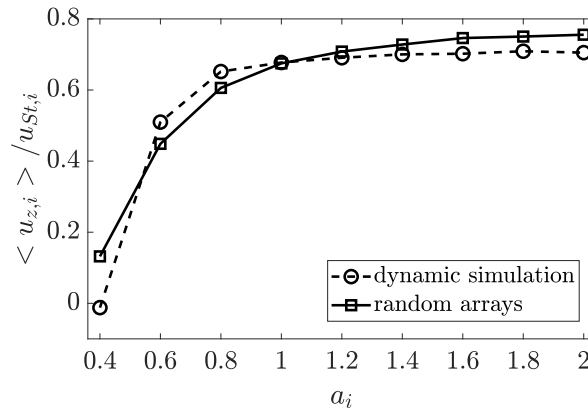


Figure 4.25: Normalized average settling velocity of each size class comparing the dynamic and the “random array” simulations.

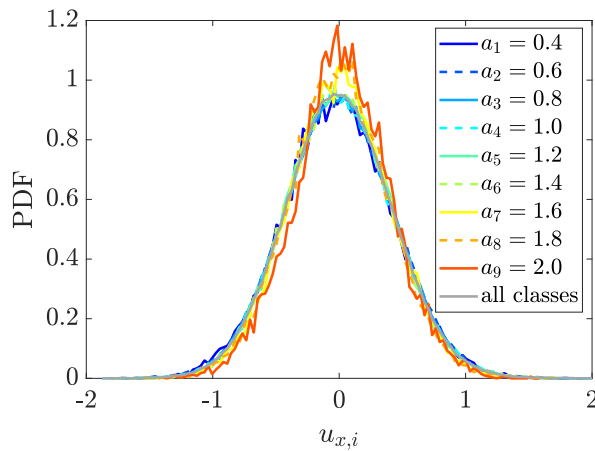


Figure 4.26: Probability distribution functions of horizontal velocities of spheres in each size class from the dynamic simulations.

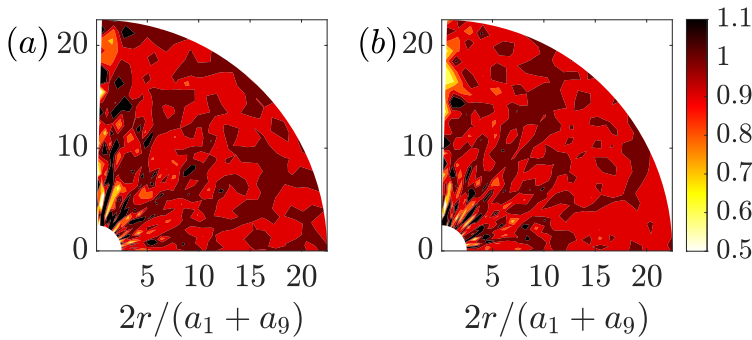


Figure 4.27: Pair distribution functions of particle positions (between the smallest and the largest size classes) for (a) “random array” and (b) dynamic simulations.

the volume fraction ϕ . This is the first work that reports the velocity of each particle class for a log-normally distributed system with number of classes larger than 3. The class-averaged settling velocity $\langle u_{z,i} \rangle$ of each particle size class was found to decrease for increasing α . The strongest dependence on the parameters was found in the range of small particles: $\langle u_{z,i} \rangle$ decays, with increasing ϕ or increasing α , faster for the smaller particles than for the largest particles, indicating a larger effect of hydrodynamic interactions on the lower tail of the particle size distribution.

The probability distribution functions of horizontal and vertical velocities of each size class tend to follow approximately a Gaussian distribution. The magnitude of the horizontal and vertical velocity fluctuations for each size class increases as ϕ or α increases, and appear to follow the approximate scaling $u'_i \sim u_{st,i}(\alpha_i/\langle \alpha \rangle)^{-2}$. Our simulations for the log-normally dispersed system suggest a value of about 3.5 for the anisotropy ratio between the vertical and the horizontal velocity fluctuations. This value is comparable to the one observed in our simulations for monodisperse or bidisperse suspensions.

A detailed comparison with available theoretical model has been proposed. The accuracy of Richardson-Zaki’s correlation for polydispersed suspensions was found to be unacceptable: for $\alpha=0.4$ and $\phi=0.05$, the value predicted by Richardson-Zaki’s formula for the smallest particles can be up to seven times larger than the simulated value! On the other hand, the MLB model works surprisingly well for predicting the settling velocity of the upper tail of the particle size distribution, but not the lower tail. Our simulations confirm that Batchelor’s model gives quite accurate predictions for all size classes when $\phi \leq 0.05$, yielding discrepancies of the settling velocities that are within 10% of the numerical results. The Davis & Gecol model and the MLB model give comparable predictions in our range of volume fractions. Both these models tend to overestimate the hindered settling function of the smaller particles. The discrepancy

between the models and the simulation data increases as α or ϕ increases, suggesting that future studies should focus on moderately dense suspensions with a wide size ratio.

Although both models overestimate the settling velocity of the smaller particles, the MLB model gives much more accurate predictions than the Richardson-Zaki's correlation. MLB is also based on Richardson-Zaki's formula, but in the MLB model the formula is used to estimate the particle-fluid slip velocity, not the absolute settling velocity. For applications where the focus is predicting the sedimentation of the larger particles (e.g., separation of large particles from a polydisperse mixture), using the MLB model could be sufficient. For applications where the stratification in different layers needs to be predicted (e.g. in sedimentology [4]), using the MLB model will overestimate the fraction of the smaller particles in the sediment region. In particle size fractionation by centrifugation or sedimentation [2, 14]), using the MLB model could give a wrong prediction of the region where most of the small particles are located, jeopardising the entire size fractionation procedure.

Looking at the main assumptions of the MLB model, re-derived in the Appendix B, we can see that the model rests on the assumption that the Stokes drag correction for each size class only depends on the total volume fraction of the suspension. This assumption cannot hold in general, and thus this is the main area of model improvement. Despite our efforts, we have not been able to propose, based on rigorous fluid mechanics arguments, an improvement of the MLB model in which the effect of polydispersity is accounted for in the closure of the fluid-particle velocity slip. Perhaps data for the drag force on polydisperse fixed arrays subject to a uniform flow [34, 55–57] could be used to suggest improved models. However, one should take into account that uniform flow past a fixed polydisperse array and the average velocity of a polydisperse array subject to known external forces are two different problems. Given the difficulty of coming up with a closure relation valid for all particle sizes, machine learning techniques such as symbolic regression [58–61] could be used to incorporate into the MLB model information about the moments of the particle size distribution.

The good comparison between Batchelor's model and the simulation data for sufficiently small ϕ enables us to use this analytical model to illustrate why the prediction of the velocity of the small particles is highly dependent on the full particle size distribution, while that of the large particles is not. Equation (4.1) can be rewritten as

$$h_i = 1 + S_{ii}\phi + \sum_{j=1}^m (S_{ij} - S_{ii})\phi_j, \quad (4.16)$$

where $S_{ii} = -6.55$ and ϕ is the total volume fraction. The direct influence of the size of particle class j on the hindered settling of particle class i is negligible if $|(S_{ij} - S_{ii})\phi_j| \ll |S_{ii}\phi|$. For $\phi = 0.05$, the magnitude of the intra-class interaction term

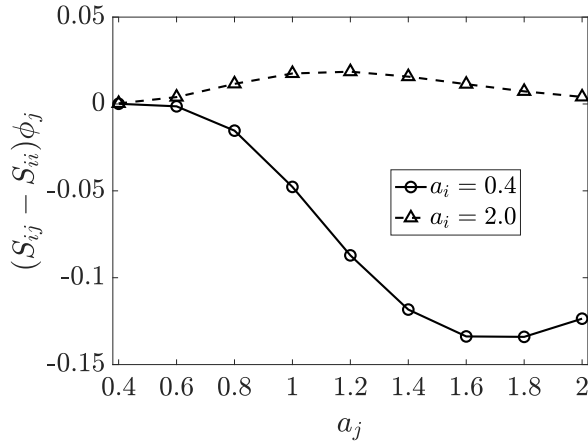


Figure 4.28: Inter-class interaction term appearing on the right hand side of equation (4.16) for $a_i = 0.4$ (“small” particles) and $a_i = 2$ (“large” particles). The particle size distribution corresponds to $\alpha = 0.4$ and $\phi = 0.05$.

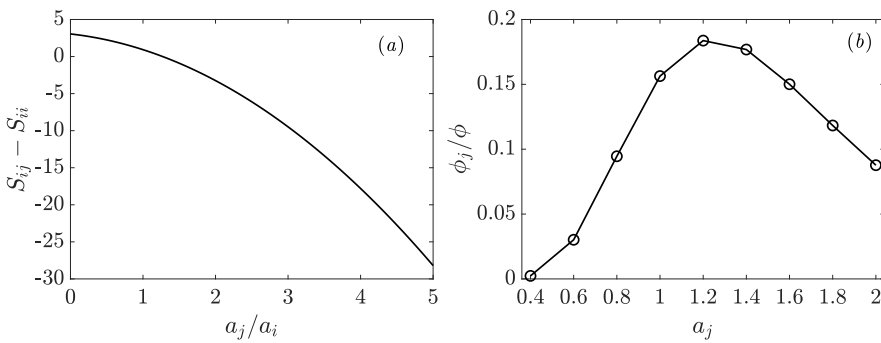


Figure 4.29: (a) Interaction coefficients $S_{ij} - S_{ii}$ and (b) volume fraction distribution corresponding to the interaction term of figure 4.28.

is $|S_{ii}\phi| = 0.33$. Let us compare this value to the inter-class interaction term for $\phi = 0.05$. In figure 4.28 $(S_{ij} - S_{ii})\phi_j$ is shown for $\alpha_i = 0.4$ (small particles) and $\alpha_i = 2$ (large particles), for $\alpha = 0.4$. The maximum absolute value of the inter-class interaction term for the small particle is 0.13, not negligible in comparison to 0.33. The maximum value of the inter-class interaction term for the largest particles is instead 18 times smaller than the intra-class interaction term. The question is: in the case of log-normally distributed particles, why is the inter-class interaction term small for the large particles? Is this because the interaction coefficients are small in magnitude? Or because of the distribution of volume fractions?

To reply to these questions, in figures 4.29 (a) and (b) we show $(S_{ij} - S_{ii})$ and ϕ separately. For completeness, in figure 4.29 (a) $(S_{ij} - S_{ii})$ is shown also for $\alpha_j/\alpha_i \rightarrow 0$ (even though the smallest value we consider in our work is 0.2). It is seen that in our log-normal distribution the volume fraction corresponding to the small particles is small in comparison to that of the large particles, and tends to zero as the lower tail of the particle size distribution is approached. The quantity $(S_{ij} - S_{ii})$ is on the other hand not diverging for $\alpha_j/\alpha_i \ll 1$, and is $O(1)$ in this limit. Therefore, specifically for a log-normal particle size distribution the reason why the lower tail has a small influence on the upper tail is that the volume fraction corresponding to the lower tail is comparatively small and is weighted by an interaction term that is not large. For a more general particle size distribution, the situation is more subtle. For example, if the particle size distribution was such that ϕ was comparatively large in the small particle range, one would expect the settling velocity of the largest particles to be more affected by the smallest particles than seen in our simulations. To test this hypothesis, we simulated a case where there are 5 size classes and all size classes have the same volume fraction. The corresponding number frequency distribution is shown in figure 4.30. The smallest size class occupies in terms of particle numbers more than 80% of the total. The normalized average settling velocities from simulations and model predictions are shown in figure 4.31 for a total volume fraction of 0.03. Batchelor's model gives quite accurate predictions, whereas other models overpredict the hindered settling functions of smaller size classes. The large particles are still relatively uninfluenced by the small particles, even if the volume fraction of the small particles is significantly larger than in the simulations with the log-normal particle size distribution. The reason for this is that while $S_{ij} - S_{ii} \approx 3$ for $\alpha_j/\alpha_i \ll 1$, this $O(1)$ value is still much smaller than the value $|S_{ij} - S_{ii}| \approx 30$ for α_j/α_i close to 5 (see figure 4.29). In other words, the settling velocity of large particles is *directly* influenced by the size distribution of particles in neighbouring size classes only. It seems that, from the point of view of the velocity of the large particles, the specific size distribution of the small particles does not matter, only the total volume fraction contribution due to the small particles matters, via the term $S_{ii}\phi$ in equation (4.16).

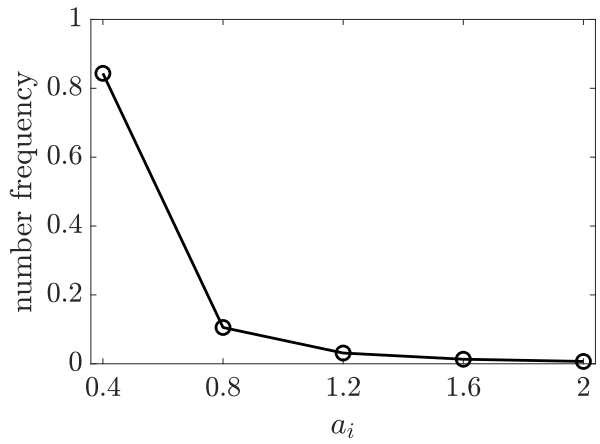


Figure 4.30: Number frequency distribution of a polydisperse suspension where all size classes have the same volume fraction.

CHAPTER 4

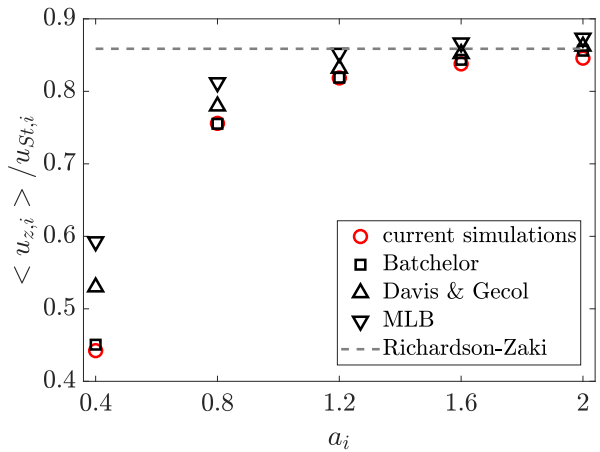


Figure 4.31: Hindered settling function corresponding to the size distribution of figure 4.30.

The analysis above also gives insights into the condition for which models parameterised on the total volume fraction can be used as a first, practical approximation for the prediction of the settling of a dilute polydisperse suspension. This approximation is reasonable when the inter-class interaction term is comparatively small. This term is small when either $\phi_j \ll 1$ for finite $S_{ij} - S_{ii}$, the case discussed above. Or when the particle size distribution is narrow so that $|S_{ij} - S_{ii}| \rightarrow 0$, the case discussed by Davis and Hassen [30] (see the value of $S_{ij} - S_{ii}$ for a_j/a_i approaching 1 in figure 4.28 (a)). If deviations of S_{ij} from S_{ii} are small, then it can be seen from equation (4.13) that the hindered settling function for $\phi \ll 1$ depends only on the total volume fraction. For a not too dense suspension with a narrow size distribution, the use of Richardson-Zaki's correlation is for example partially justified (note that the exponent $n \simeq 5$ in the Richardson-Zaki correlation is numerically close to $|S_{ii}| = 6.5$; this "lucky coincidence" was also noted by Davis and Hassen [30]).

A challenge in the current investigation has been the lack of experimental data to compare to. Experimental techniques such as X-ray radiography [62], magnetic resonance imaging [63], or optical experiments with fluorescent particles [64] could be used to measure the velocity of a given small particle fraction in a widely polydisperse suspension.

REFERENCES

- [1] W. He, Q. Wang, Y. Zhu, K. Wang, J. Mao, X. Xue, and Y. Shi. “Innovative technology of municipal wastewater treatment for rapid sludge sedimentation and enhancing pollutants removal with nano-material.” In: *Bioresource Technology* 324 (2021), p. 124675.
- [2] Francesco Bonaccorso, Mirco Zerbetto, Andrea C Ferrari, and Vincenzo Amendola. “Sorting nanoparticles by centrifugal fields in clean media.” In: *The Journal of Physical Chemistry C* 117.25 (2013), pp. 13217–13229.
- [3] K. Papuga, J. Kaszubkiewicz, and D. Kawalko. “Do we have to use suspensions with low concentrations in determination of particle size distribution by sedimentation methods?” In: *Powder Technology* 389 (2021), pp. 507–521.
- [4] Robert Dorrell and Andrew J Hogg. “Sedimentation of bidisperse suspensions.” In: *International Journal of Multiphase Flow* 36.6 (2010), pp. 481–490.
- [5] J. M. Revay and J. J. L. Higdon. “Numerical simulation of polydisperse sedimentation: equal-sized spheres.” In: *Journal of Fluid Mechanics* 243 (1992), pp. 15–32.
- [6] F.R. Cunha, G.C. Abade, A.J. Sousa, and E.J. Hinch. “Modeling and direct simulation of velocity fluctuations and particle-velocity correlations in sedimentation.” In: *Journal of Fluids Engineering* 124.4 (2002), pp. 957–968.
- [7] Micheline Abbas, Eric Climent, Olivier Simonin, and Martin R Maxey. “Dynamics of bidisperse suspensions under Stokes flows: Linear shear flow and sedimentation.” In: *Physics of Fluids* 18.12 (2006).
- [8] M. Wang and J. F. Brady. “Short-time transport properties of bidisperse suspensions and porous media: A Stokesian dynamics study.” In: *The Journal of Chemical Physics* 142.9 (2015).
- [9] MA Al-Naafa and M Sami Selim. “Sedimentation of monodisperse and bidisperse hard-sphere colloidal suspensions.” In: *AIChE Journal* 38.10 (1992), pp. 1618–1630.
- [10] Robert H Davis and Hatice Gecol. “Hindered settling function with no empirical parameters for polydisperse suspensions.” In: *AIChE Journal* 40.3 (1994), pp. 570–575.

- [11] H. Chen, X. Jia, M. Fairweather, and T. N. Hunter. “Characterising the sedimentation of bidisperse colloidal silica using analytical centrifugation.” In: *Advanced Powder Technology* 34.2 (2023), p. 103950.
- [12] GK Batchelor. “Sedimentation in a dilute polydisperse system of interacting spheres. Part 1. General theory.” In: *Journal of Fluid Mechanics* 119 (1982), pp. 379–408.
- [13] S. Berres, R. Bürger, and E. M. Tory. “Applications of polydisperse sedimentation models.” In: *Chemical Engineering Journal* 111.2-3 (2005), pp. 105–117.
- [14] Claudia Backes, Beata M Szydłowska, Andrew Harvey, Shengjun Yuan, Victor Vega-Mayoral, Ben R Davies, Pei-liang Zhao, Damien Hanlon, Elton JG Santos, Mikhail I Katsnelson, et al. “Production of highly monolayer enriched dispersions of liquid-exfoliated nanosheets by liquid cascade centrifugation.” In: *ACS Nano* 10.1 (2016), pp. 1589–1601.
- [15] S. Pednekar, J. Chun, and J. F. Morris. “Bidisperse and polydisperse suspension rheology at large solid fraction.” In: *Journal of Rheology* 62.2 (2018), pp. 513–526.
- [16] E. Gonzalez, C. Aponte-Rivera, and R. N. Zia. “Impact of polydispersity and confinement on diffusion in hydrodynamically interacting colloidal suspensions.” In: *Journal of Fluid Mechanics* 925 (2021), A35.
- [17] A. A. Howard, M. R. Maxey, and S. Gallier. “Bidisperse suspension balance model.” In: *Physical Review Fluids* 7.12 (2022), p. 124301.
- [18] N. Malbranche, B. Chakraborty, and J. F. Morris. “Shear thickening in dense bidisperse suspensions.” In: *Journal of Rheology* 67.1 (2023), pp. 91–104.
- [19] O.M. Lavrenteva, I. Smagin, and A. Nir. “Shear-induced particle migration in viscous suspensions with continuous size distribution.” In: *Physical Review Fluids* 9.2 (2024), p. 024305.
- [20] M. J. Lockett and K.S. Bassoon. “Sedimentation of binary particle mixtures.” In: *Powder Technology* 24.1 (1979), pp. 1–7.
- [21] R.H. Davis and K.H. Birdsell. “Hindered settling of semidilute monodisperse and polydisperse suspensions.” In: *AIChE Journal* 34.1 (1988), pp. 123–129.
- [22] B. Vowinckel, J. Withers, P. Luzzatto-Fegiz, and E. Meiburg. “Settling of cohesive sediment: particle-resolved simulations.” In: *Journal of Fluid Mechanics* 858 (2019), pp. 5–44.
- [23] N. J. Di Vaira, Ł. Łaniewski-Wołk, R. L. Johnson, S. M. Aminossadati, and C. R. Leonardi. “Influence of particle polydispersity on bulk migration and size segregation in channel flows.” In: *Journal of Fluid Mechanics* 939 (2022), A30.

- [24] C. Rettinger, S. Eibl, U. Rde, and B. Vowinkel. "Rheology of mobile sediment beds in laminar shear flow: effects of creep and polydispersity." In: *Journal of Fluid Mechanics* 932 (2022), A1.
- [25] R. H. Davis and A. Acrivos. "Sedimentation of noncolloidal particles at low Reynolds numbers." In: *Annual Review of Fluid Mechanics* 17.1 (1985), pp. 91–118.
- [26] G.K. Batchelor. "Sedimentation in a dilute dispersion of spheres." In: *Journal of Fluid Mechanics* 52.2 (1972), pp. 245–268.
- [27] G.K. Batchelor and C.S. Wen. "Sedimentation in a dilute polydisperse system of interacting spheres. Part 2. Numerical results." In: *Journal of Fluid Mechanics* 124 (1982), pp. 495–528.
- [28] J. H. Masliyah. "Hindered settling in a multi-species particle system." In: *Chemical Engineering Science* 34.9 (1979), pp. 1166–1168.
- [29] Bo Xue and Yan Sun. "Modeling of sedimentation of polydisperse spherical beads with a broad size distribution." In: *Chemical Engineering Science* 58.8 (2003), pp. 1531–1543.
- [30] R. H. Davis and M. A. Hassen. "Spreading of the interface at the top of a slightly polydisperse sedimenting suspension." In: *Journal of Fluid Mechanics* 196 (1988), pp. 107–134.
- [31] A Abeynaike, AJ Sederman, Y Khan, ML Johns, JF Davidson, and MR Mackley. "The experimental measurement and modelling of sedimentation and creaming for glycerol/biodiesel droplet dispersions." In: *Chemical Engineering Science* 79 (2012), pp. 125–137.
- [32] J.F. T. Richardson and W.N. Zaki. "Sedimentation and fluidization: part 1." In: *Transactions of the Institution of Chemical Engineers* 32 (1954), pp. 35–53.
- [33] T.A. Brzinski III and D.J. Durian. "Observation of two branches in the hindered settling function at low Reynolds number." In: *Physical Review Fluids* 3.12 (2018), p. 124303.
- [34] Z. Cheng and A. Wachs. "Hydrodynamic force and torque fluctuations in a random array of polydisperse stationary spheres." In: *International Journal of Multiphase Flow* 167 (2023), p. 104524.
- [35] John F Brady, Ronald J Phillips, Julia C Lester, and Georges Bossis. "Dynamic simulation of hydrodynamically interacting suspensions." In: *Journal of Fluid Mechanics* 195 (1988), pp. 257–280.
- [36] John F Brady, Georges Bossis, et al. "Stokesian dynamics." In: *Annual Review of Fluid Mechanics* 20.1 (1988), pp. 111–157.

- [37] D. P. Willen and A. Prosperetti. “Resolved simulations of sedimenting suspensions of spheres.” In: *Physical Review Fluids* 4.1 (2019), p. 014304.
- [38] Y. Yao, C. S. Criddle, and O. B. Fringer. “The effects of particle clustering on hindered settling in high-concentration particle suspensions.” In: *Journal of Fluid Mechanics* 920 (2021), A40.
- [39] T. Shajahan and W. Breugem. “Inertial effects in sedimenting suspensions of solid spheres in a liquid.” In: *International Journal of Multiphase Flow* 166 (2023), p. 104498.
- [40] Sangtae Kim and Seppo J Karrila. *Microhydrodynamics: principles and selected applications*. Butterworth-Heinemann, 2013.
- [41] J. F. Brady and L. J. Durlofsky. “The sedimentation rate of disordered suspensions.” In: *Physics of Fluids* 31.4 (1988), pp. 717–727.
- [42] Jens Rotne and Stephen Prager. “Variational treatment of hydrodynamic interaction in polymers.” In: *The Journal of Chemical Physics* 50.11 (1969), pp. 4831–4837.
- [43] Pawel J Zuk, E Wajnryb, KA Mizerski, and P Szymczak. “Rotne–Prager–Yamakawa approximation for different-sized particles in application to macromolecular bead models.” In: *Journal of Fluid Mechanics* 741 (2014), R5.
- [44] C.W.J. Beenakker. “Ewald sum of the Rotne–Prager tensor.” In: *The Journal of Chemical Physics* 85.3 (1986), pp. 1581–1582.
- [45] K. R. Hase and R. L. Powell. “Calculation of the Ewald summed far-field mobility functions for arbitrarily sized spherical particles in Stokes flow.” In: *Physics of Fluids* 13.1 (2001), pp. 32–44.
- [46] H. Hasimoto. “On the periodic fundamental solutions of the Stokes equations and their application to viscous flow past a cubic array of spheres.” In: *Journal of Fluid Mechanics* 5.2 (1959), pp. 317–328.
- [47] E. Wacholder and N. F. Sather. “The hydrodynamic interaction of two unequal spheres moving under gravity through quiescent viscous fluid.” In: *Journal of Fluid Mechanics* 65.3 (1974), pp. 417–437.
- [48] H. Nicolai, B. Herzhaft, E. J. Hinch, L. Oger, and E. Guazzelli. “Particle velocity fluctuations and hydrodynamic self-diffusion of sedimenting non-Brownian spheres.” In: *Physics of Fluids* 7.1 (1995), pp. 12–23.
- [49] J. T. Padding and A. A. Louis. “Hydrodynamic and Brownian fluctuations in sedimenting suspensions.” In: *Physical Review Letters* 93.22 (2004), p. 220601.

- [50] H. Hayakawa and K. Ichiki. “Statistical theory of sedimentation of disordered suspensions.” In: *Physical Review E* 51.5 (1995), R3815.
- [51] A. Moncho-Jordá, A.A. Louis, and J.T. Padding. “Effects of interparticle attractions on colloidal sedimentation.” In: *Physical Review Letters* 104.6 (2010), p. 068301.
- [52] R. J. Phillips, J. F. Brady, and G. Bossis. “Hydrodynamic transport properties of hard-sphere dispersions. I. Suspensions of freely mobile particles.” In: *Physics of Fluids* 31.12 (1988), pp. 3462–3472.
- [53] Y. Peysson and E. Guazzelli. “Velocity fluctuations in a bidisperse sedimenting suspension.” In: *Physics of Fluids* 11.7 (1999), pp. 1953–1955.
- [54] G.K. Batchelor and R. W. Janse Van Rensburg. “Structure formation in bidisperse sedimentation.” In: *Journal of Fluid Mechanics* 166 (1986), pp. 379–407.
- [55] M. A. van der Hoef, R. Beetstra, and J.A.M. Kuipers. “Lattice-Boltzmann simulations of low-Reynolds-number flow past mono-and bidisperse arrays of spheres: results for the permeability and drag force.” In: *Journal of Fluid Mechanics* 528 (2005), pp. 233–254.
- [56] X. Yin and S. Sundaresan. “Fluid-particle drag in low-Reynolds-number polydisperse gas–solid suspensions.” In: *AIChE Journal* 55.6 (2009), pp. 1352–1368.
- [57] S. Sarkar, M. A. van der Hoef, and J. A. M. Kuipers. “Fluid–particle interaction from lattice Boltzmann simulations for flow through polydisperse random arrays of spheres.” In: *Chemical Engineering Science* 64.11 (2009), pp. 2683–2691.
- [58] J. Zhang and W. Ma. “Data-driven discovery of governing equations for fluid dynamics based on molecular simulation.” In: *Journal of Fluid Mechanics* 892 (2020), A5.
- [59] Y. M. F El Hasadi and J. T. Padding. “Do logarithmic terms exist in the drag coefficient of a single sphere at high Reynolds numbers?” In: *Chemical Engineering Science* 265 (2023), p. 118195.
- [60] C. Wu and Y. Zhang. “Enhancing the shear-stress-transport turbulence model with symbolic regression: A generalizable and interpretable data-driven approach.” In: *Physical Review Fluids* 8.8 (2023), p. 084604.
- [61] Z. Cheng and A. Wachs. “Physics-informed neural network for modeling force and torque fluctuations in a random array of bidisperse spheres.” In: *International Journal of Multiphase Flow* 169 (2023), p. 104603.

- [62] E. Dulanjalee, F. Guillard, J. Baker, I. Einav, and B. Marks. “Measuring grain size fractions of bidisperse granular materials using X-ray radiography.” In: *Optics Express* 28.20 (2020), pp. 29202–29211.
- [63] C. M. Boyce, N.P. Rice, A. Ozel, J.F. Davidson, A.J. Sederman, L.F. Gladden, S. Sundaresan, J.S. Dennis, and D.J. Holland. “Magnetic resonance characterization of coupled gas and particle dynamics in a bubbling fluidized bed.” In: *Physical Review Fluids* 1.7 (2016), p. 074201.
- [64] P. Snabre, B. Pouligny, C. Metayer, and F. Nadal. “Size segregation and particle velocity fluctuations in settling concentrated suspensions.” In: *Rheologica Acta* 48 (2009), pp. 855–870.

5

ENHANCED SETTLING OF A GROUP OF SPHERES

To quantify the hindered settling function from the experiments, it is important to accurately measure the single particle Stokes velocity. In this chapter, we present both simulations and experiments in the Stokes regime to illustrate how the particle settling velocity measured from the experiments can be affected by a large error compared to its corresponding Stokes velocity when the particles are added as a group, as usually done in experiments with natural sediments. The experiments are carried out by our collaborators from Deltares.

This chapter is based on the article:

H. Li et al. "Collective settling of spherical particles and implications for the experimental measurement of particle density." In: *(To be submitted)*.

5.1 Introduction

The quantification of particle settling velocities is important in industrial processes, to estimate for instance the residence time of particles in gravity settlers [1], or to predict the transport and fate of sediments in natural systems [2, 3]. Furthermore, interest in the behaviour of microplastics in the aquatic environment, triggered by the fact that more and more microplastics are found in water bodies [4–6], has led to numerous studies on the settling rate of the microplastics [7–11].

The most common approach to measure the settling rate of particles is to transfer a small amount (mL) of liquid containing a dilute particle suspension into a settling column by using a pipette. The settling velocity is recorded with a camera at locations far away from the injection point, to ensure that the particles have reached their terminal velocities [9, 12, 13]. This procedure is also adopted to measure the settling velocity of particle aggregates, such as low-density flocs found in estuarine regions [14–17] and other sediments [18]. In most practical cases involving flocs, particle (floc) density is very close to the density of the suspending liquid, typically water. Therefore, the particles settle in the Stokes regime. In this regime the settling velocity of an isolated particle in an unbounded domain is proportional to the solid-fluid density difference $\Delta\rho$ according to $u = (2/9)\Delta\rho g a^2/\mu$, where μ is the fluid viscosity, g is the acceleration of gravity, and a is the radius of the particle. Provided the suspension is sufficiently dilute, this expression can be used to calculate $\Delta\rho$ from the measured particle velocity.

Recent experiments with flocs have shown that the settling velocity measured with the pipette method is incompatible with predictions using realistic values of the density of the floc. Measurements with the suspension drop give values of the settling velocity of flocs that are much larger than the value predicted by the Stokes settling rate [14]. These experiments have instead showed that dropping single flocs in the settling column gave values that are close to the Stokes settling value. In the current paper we call the first mode of settling collective enhanced settling.

In the current paper we present simulations that illustrate the difference between collective enhanced settling and individual settling, starting from experimental observations using spherical particles of controlled size and density. The use of such well controlled particles enables us to be in the regime where the Stokes formula is known to hold exactly in the individual settling case and avoid the uncertainties in shape, size and density encountered when using flocs.

The results of our paper on the effect of collective motions on particle settling is of practical interest in several contexts. Collective settling is encountered during the discharge of particle-laden plumes in (deep-sea) mining [19], the propagation of turbidity currents [20] and hypopycnal plumes [21], etc. To estimate the settling fluxes in the far-field region of the plume, where the particle concentration is very low, the

Stokes settling velocity is used as input parameter, and its validity assumed. The assumption is based on the fact that the suspension is very dilute (volume fraction within 1%), so hydrodynamic interactions are assumed to be unimportant. The current paper challenges this assumption.

Settling of suspension drops in quiescent viscous liquids has been studied both experimentally and numerically [22–24]. In these studies, the initial velocity of the cloud, breakup of the cloud and particle leakage from the cloud were the main focuses. In the current paper, we are interested in discussing implications of theoretical predictions for the settling velocity as a function of solid concentration and particle polydispersity in view of experimental measurements. For this purpose, we start from some experimental observations with the FLOCCAM setup described in Sec. 5.2 and then use simulations (Sec. 5.3) to illustrate the limitations of the experimental method and ways of overcoming these limitation.

5.2 Experimental method

For the settling experiments two batches of polystyrene particles are utilized, with a median particle diameter of approximately $600\mu\text{m}$ and $900\mu\text{m}$, as characterised by the particle size distribution shown in Fig. 5.1 (obtained with a Malvern Mastersizer 2000 [25]). The density of the particles is in the range of $1020\text{--}1040\text{kg/m}^3$. The liquid used is water (density $\rho_f = 1000\text{ kg/m}^3$).

The settling velocity was measured with TU Delft's FLOCCAM device. The FLOCCAM device is a video microscopy based system designed to measure particle size distributions (PSDs) for particles larger than $20\mu\text{m}$ and the particle settling velocity [26–30]. A schematic of the setup is shown in figure 5.2.

The FLOCCAM system comprises several key components. Central to the setup is a cylindrical settling column measuring $10\text{cm} \times 10\text{cm} \times 30\text{cm}$, with glass panels on the front and back, and plastic side walls. Video footage of the settling particles is captured by a 5MP CMOS camera with a resolution of 2592×2048 pixels and a pixel size of $4.8\mu\text{m}$. The camera, equipped with a Global Shutter (model: iDS UI-3180CP-M-GL Rev.2.1, AB02546), is paired with a telecentric lens (model: S5VPJ2898) manufactured by Sill Optics GmbH & Co. KG, featuring an adjustable working distance and a C-mount. This combination provides a pixel resolution of approximately $8.6\mu\text{m}$.

For illumination, a Flat Lights TH2 Series Red LED panel ($63\text{mm} \times 60\text{mm}$) was employed due to its high directivity, ensuring consistent lighting throughout the experiments. The light panel was powered and controlled by a DC 24V Input Controller (model: PB-2430-1) from CCS Inc.

To inject the particles into the settling column, a plastic conical feed well terminating with a rectangular outlet measuring $2\text{mm} \times 10\text{mm}$ was used. A suspension drop

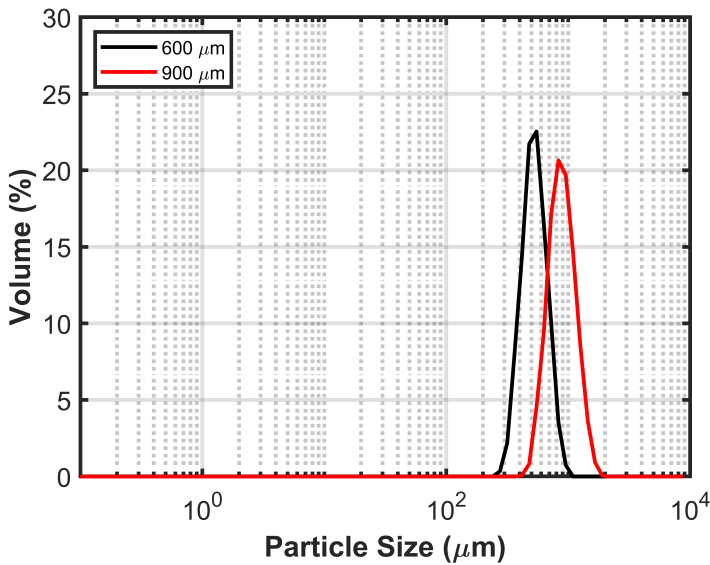


Figure 5.1: Particle size (diameter) distribution of polystyrene particles as measured by Malvern Mastersizer 2000.

containing particles were carefully extracted using a pipette and released into the column. Settling velocities were recorded approximately 25cm below the injection point.

The post-processing of FLOCCAM videos was done by using the software Safas [26, 31]. Safas, which stands for Sedimentation and Floc Analysis Software, is a Python module specifically designed for processing and analyzing images and videos of sedimenting particles, especially cohesive sediment flocs. This open-source software enables users to easily extract critical data such as particle size, morphology, and settling velocity, allowing users to customize its image filters.

In the first set of experiments, particles with a given size (600 μm or 900 μm) were tested under both individual settling and group settling conditions. For the individual settling case, each particle was introduced into the settling column one at the time, ensuring no interference from neighbouring particles. In the collective settling case, a small amount of particles were transferred into the column.

The group settling behaviour of a polydisperse group of particles, consisting of a mixture of 600 μm and 900 μm particles, was also studied and compared to the individual settling behaviours of particles from each size range. The ratio between the number of 600 μm and 900 μm particles in the mixed group is 7 : 1.

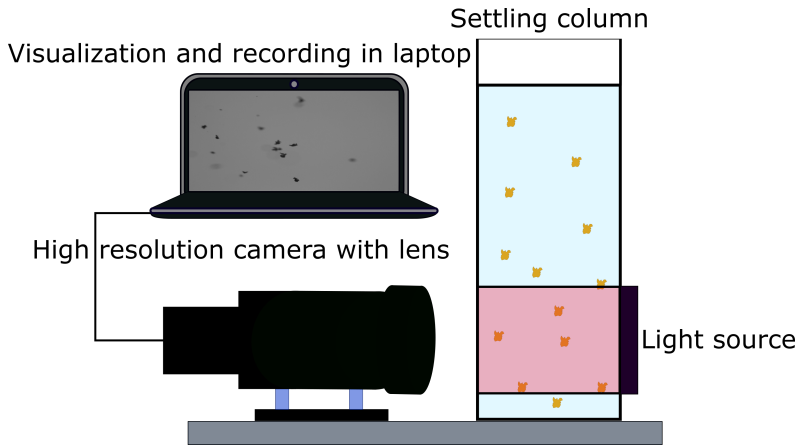


Figure 5.2: Schematic representation of the FLOCCAM setup [26].

5.3 Simulation approach

Simulations are carried out with a Stokesian dynamics method in the force formulation [32, 33]. The simulation code is the same as in Ref. [34], where complete validation cases are presented. Essentially the method is based on calculating the average settling velocity starting from the particle position by knowing that, in a low-Reynolds number suspension, the velocity of each particle is a linear function of the gravitational forces (weight and buoyancy) acting on each particle.

The numerical simulations are carried out as follows. Firstly, particles are randomly placed inside a cubic box ensuring no overlap between any pair of particles. The group of particles in the box is assumed to settle in an unbounded fluid. Then, the particle velocities are calculated by the Stokesian dynamics method [32, 33]. In the Stokesian Dynamics method, a mobility matrix \mathbf{M} is assembled based on the relative position of all the particles. For this matrix, which incorporates the hydrodynamic interactions between the particles, we adopt the Rotne-Prager approximation [35, 36] (this approximation is appropriate for dilute suspensions). Formulas for the components of \mathbf{M} in this approximation are taken from Refs. [35, 36]. The vector containing the velocities of the particles is calculated from the following equation:

$$\mathbf{U} = \mathbf{M}\mathbf{F}, \quad (5.1)$$

where \mathbf{U} is a $3N \times 1$ vector of the velocities of the N particles, and \mathbf{F} is a $3N \times 1$ vector of the forces on the N particles. For a particle with radius a , the force on the particle is $\mathbf{f} = \frac{4\pi a^3}{3}(\rho_p - \rho_f)\mathbf{g}$, where ρ_p and ρ_f are the densities of the particle and the fluid, respectively, and \mathbf{g} is the gravitational acceleration. In the simulations, the

instantaneous particle settling velocities are calculated according to equation (5.1), with forces corresponding to the assigned random configuration of the particles.

Additional dynamic simulations are also carried out. In the dynamic simulations, particle velocities are calculated according to equation (5.1) at each time step, then the particle positions are updated [37]. In the dynamic simulations, particles are randomly positioned inside a spherical domain forming a suspension drop initially.

When the average separation between identical particles of radius a is infinitely large, \mathbf{M} is a diagonal matrix with entries equal to the mobility coefficient $1/(6\pi\mu a)$, where μ is the viscosity of the fluid. At finite interparticle separations, interparticle interactions alter the settling velocity of each particle, and can make the average settling velocity of a group of particles smaller or larger than the Stokes settling velocity. The average settling velocity $\langle \mathbf{U} \rangle = \frac{4\pi a^3}{3}(\rho_p - \rho_f) \langle \mathbf{M} \rangle \mathbf{g}$, so $\langle \mathbf{M} \rangle$ depends on the interparticle separation or, equivalently, on the solid volume fraction. For a polydisperse suspension, each size class will have its own average settling velocity [34].

The simulation results are presented in non-dimensional form. The simulations are non-dimensionalized using a characteristic length a_0 and a characteristic Stokes velocity $u_0 = \frac{2a_0^2}{9\mu}(\rho_p - \rho_f)g$. For the polydispersed simulation, the characteristic length is the average radius of the particles $\langle a \rangle$.

5.4 Results and discussions

Figure 5.3 (top) presents the results of a settling experiment for particles of diameters centered around $600\mu\text{m}$, comparing individual and collective settling. When particles were introduced individually into the settling column, their velocities followed reasonably well Stokes's formula for $\rho_p \simeq 1030\text{kg/m}^3$, with a small dispersion about this law (blue dots). The addition of particles as a group has two main effects: a large dispersion of velocities for a given diameter (compare orange and blue dots) and significantly larger measured velocity of the particles in the group settling case than in the individual settling case. It may seem that the increase in settling velocity due to group settling is limited, but we should take into account that the FLOCCAM setup does not allow to measure velocities larger than 8.5mm/s , so the increase in velocity will be even larger than seen in Fig. 5.3.

Figure 5.3 (bottom) is similar to Fig. 5.3 (top), but now the comparison is between individually settling particles and mixed suspensions containing particles with diameters centered at $600\mu\text{m}$ and $900\mu\text{m}$. The addition of $900\mu\text{m}$ particles in the mixed group causes a significant spread in the velocity distribution, compared to the group settling behavior shown in figure 5.3 (top) and to a notable increase in the settling velocity of $600\mu\text{m}$ particles as well. In this new figure the fact that particle velocities can be larger than 8.5mm/s is more evident than in Fig. 5.3 (top), because the

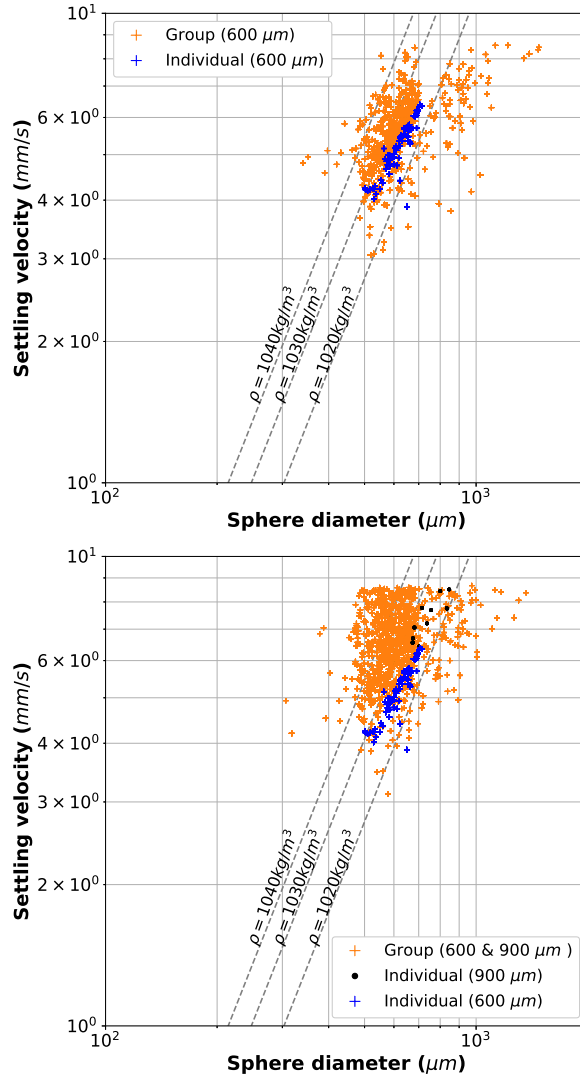


Figure 5.3: (top) experimental particle settling velocities, comparing individual and group settling for a range of particle diameters centered at $600\mu\text{m}$; (bottom) experimental particle settling velocities for a predominantly bi-disperse mixture of $600\mu\text{m}$ and $900\mu\text{m}$.

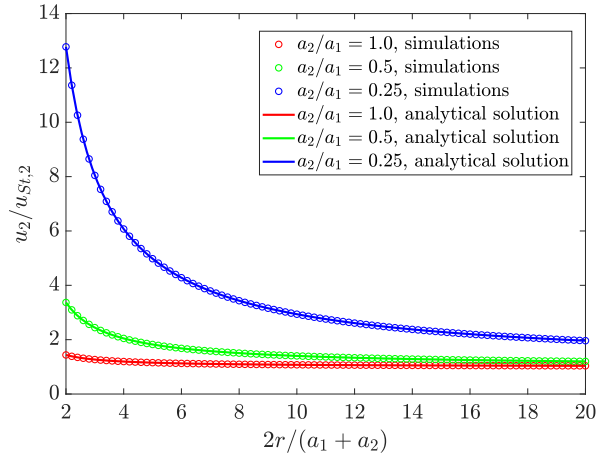


Figure 5.4: Simulated settling velocities of a sphere of radius $a_2 \leq a_1$ in a simulation of a horizontally aligned sphere pair, where one of the spheres has a radius a_1 and the other has a radius a_2 . $u_{St,2}$ is the Stokes velocity of the sphere with radius a_2 and r is the center-to-center distance of the pair. Lines are the analytical solutions of Ref. [38]

scatter plot of orange symbols is ‘cut’ at the upper velocity boundary. Therefore the measured increase in velocity due to polydispersity is in fact a lower bound of the actual increase.

The increase in the number of particles to a suspension generally is believed to give a *reduction* in settling rate [39]. The increase in settling rate in Fig. 5.3 (top) is due to the fact that the particles during addition in the FLOCCAM tank form a suspension region with an extent that is much smaller than the lateral size of the tank. In such case, the hydrodynamic interaction between the particles give a larger settling rate than in individual settling. For example, consider a pair of identical spherical particles of radius $a_1 = a_2$. Their settling velocity increases as the center-to-center separation r between the particle centers decreases, and is larger than the settling velocity of each particle by a factor that reaches almost 50% at close separation for spheres that are horizontally aligned, as illustrated in Fig. 5.4. The hydrodynamic influence of one sphere on the other sphere decays slowly, as $1/r$, so that one should reach separations $r \approx 10a_1$ to reach values comparable to the single-particle settling velocity. For an homogeneous system, an interparticle separation of $r \approx 10a_1$ corresponds to a very small solid volume fraction of 0.1%, so one should have local volume fractions that are extremely small for the the influence of hydrodynamic particle-particle interactions to be negligible.

The addition of long-range velocity disturbances by many particles settling in a group can give settling velocities much larger the single particle settling velocity. In Fig. 5.5 we compare group settling and individual settling for configurations in which

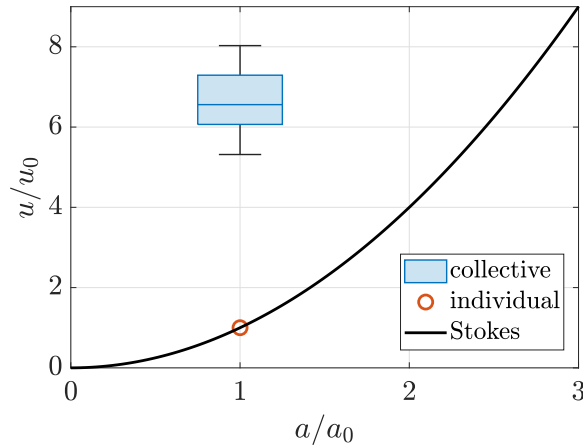


Figure 5.5: Monodisperse case: Normalized particle settling velocities in the collective settling and individual settling. The mean value and standard deviation of the settling velocity are 6.6 and 0.7, respectively. The horizontal line in the blue box represents the median value.

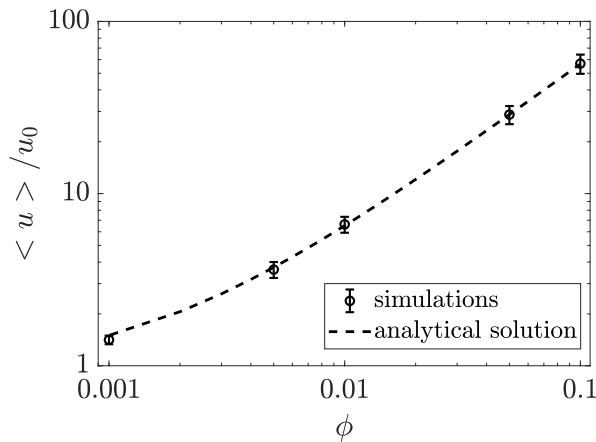


Figure 5.6: Monodisperse case: normalized average particle settling velocity versus volume fraction in the group settling. Symbols are results of current simulations with error bars showing the standard deviation of the particle velocity fluctuations. The dashed line is the analytical solution from the reference [23] for particles randomly distributed within a sphere.

100 particles are randomly placed in a cubic box of side $L = 35a$. In this plot, the average separation is such that the volume fraction is 1% and the average velocity of the group is more than 6 times larger than the single-particle Stokes velocity. The average velocity of the group will depend on the (local) volume fraction, therefore in Fig. 5.6 we plot the average velocity of the group of particles as a function of ϕ ; this plot is obtained by fixing the size of the particle and changing the particle number for a fixed simulation box size. From these graphs we can see that the dispersion about the mean value for these monodisperse simulations is comparatively small (an analysis of the problem of randomly distributed point-forces located within a sphere of radius R in Ref. [23] reports fluctuating velocity of at most 5% of the difference between the average velocity of the particle group and the single particle settling rate) and is due to the fact that particle in the center of the group move with a velocity comparable to the average velocity of the group, while the settling velocity of particles at the group's periphery is smaller than that of the group (see Fig. 5.7(a)). The average velocity of the group follows approximately the expression

$$\langle u \rangle / u_0 = 1 + \frac{6}{5} \left(\frac{R^2 \phi}{a^2} - \frac{a}{R} \right) \quad (5.2)$$

where R and ϕ are the radius and volume fraction of the cloud, derived by Ekiel-Jeżewska and co-workers [23]. To plot the dashed line in figure 5.6, R is chosen as half of the box size $L/2$. This expression could be used for an initial estimation of the size or volume fraction of the cloud so that the average particle velocity is close to the Stokes velocity.

We now turn to the analysis of simulations in the bidisperse case. The normalized particle settling velocities in both individual settling and group settling cases are shown in figure 5.8. For these calculations, in the individual settling case, a single particle with radius a_1 or a_2 is placed inside the domain. For collective settling, 50 small particles with radius a_1 and 50 large particles with radius a_2 are placed inside a cubic box with size $L = 58a_1$, resulting a volume fraction as 0.01. At this volume fraction, in the collective settling, the settling velocities of the small particles range from 10 times to 20 times their Stokes velocity (the mean value and standard deviation of the settling velocity as 16.4 and 2.3, respectively). This large influence of bidispersity on the average settling rate can be understood from the fact that, as shown in Fig. 5.4, in a pair of dissimilarly sized particles the velocity of the small particle is larger than its Stokes settling velocity and approaches the velocity of the large particle as r is reduced (in a very dilute dispersion of particles, hydrodynamic interactions are essentially pair-wise additive, so results for particle pairs translate qualitatively to a particle cloud). Of course, in a bidisperse situation the larger particles will settle faster than the small particles, resulting in phenomena of segregation within an initially homo-

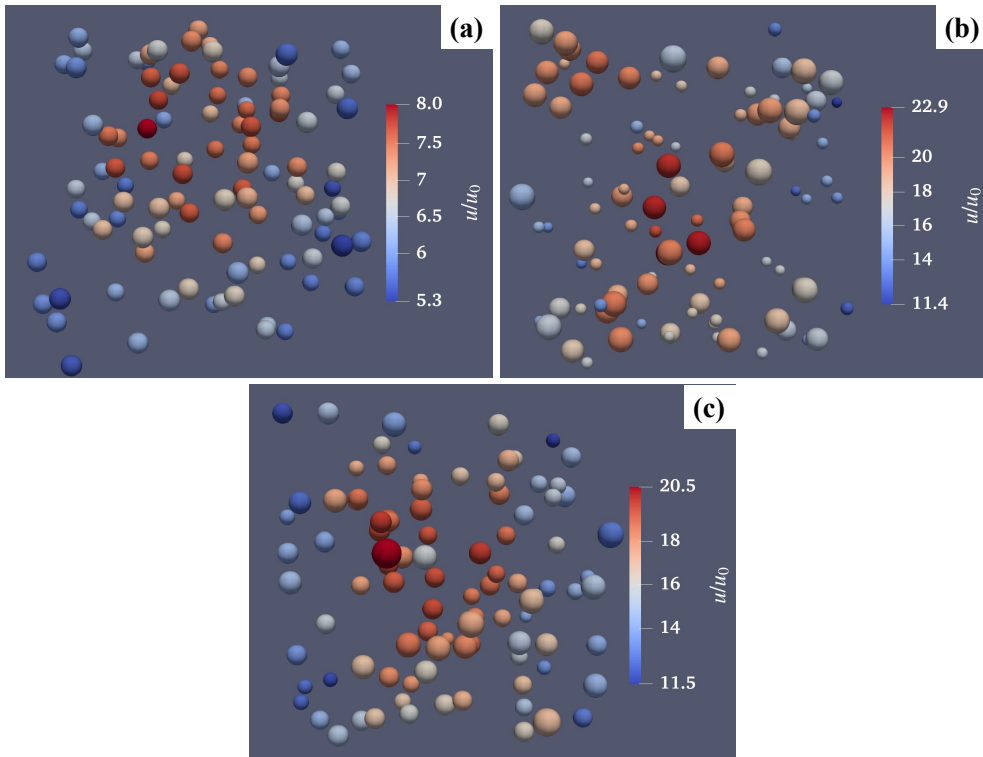


Figure 5.7: Example of simulated configurations for (a) monodisperse, (b) bidisperse and (c) polydisperse cases. The particles are colored according to their settling velocities (normalized by the reference Stokes velocity).

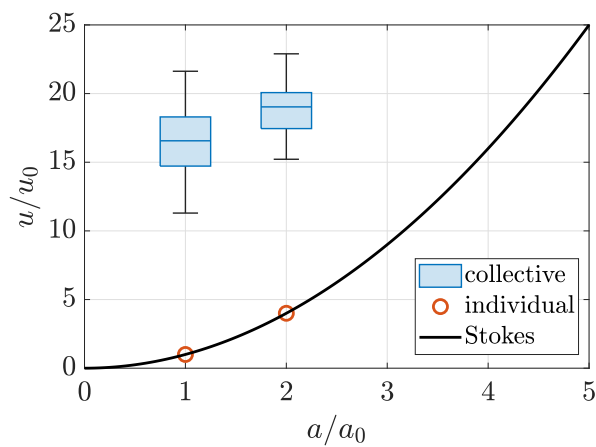


Figure 5.8: Bidisperse case: Normalized particle settling velocities in the collective settling and individual settling.

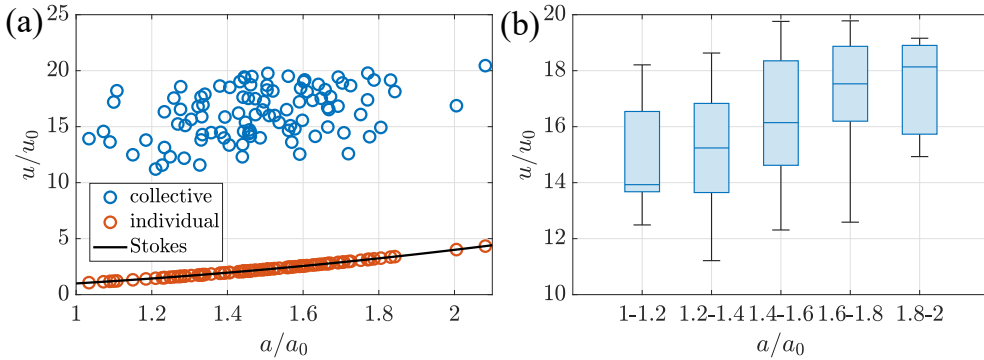


Figure 5.9: Polydisperse case: (a) normalized particle settling velocities comparing collective and individual settling, and (b) normalized particle settling velocities per size range in the collective settling.

geneous cloud [40] or even disintegration of the cloud [37] depending on the relative particle size.

Finally, Fig. 5.9 shows results for the polydisperse case. The particle size is distributed according to a Gaussian with mean 1.5 and standard deviation 0.2. A graph comparing the settling velocity vs particle radius for individual settling and collective settling is shown in figure 5.9 (a). For the collective settling simulation, 100 particles are placed randomly in a cubic box with $L = 50$ (volume fraction $\phi = 0.01$). The average settling velocity of the group of particles is at least 10 times larger than the individual settling rate. Fluctuations in the velocity around the mean value, for each value of a are comparatively large, so assigning a law of dependence between u and a can only be done in a least-square sense. The scatter plot of Fig. 5.9 (a) and the values presented in Fig. 5.9 (b), where the settling data is plotted per particle size classes, indicate that in group settling the correlation between particle size and velocity is weak.

From the discussion above, it may seem that the use of a polydisperse suspension is detrimental to calculating the particle mass density from the settling rate in an experiment. However, we will now argue with the help of dynamic simulations that polydispersity may in fact help.

As a cloud of initially spherical monodisperse particles settles, the cloud maintains its shape while growing in size until it breaks up into “blobs”. While the cloud maintains its shape, the settling velocity is much larger than the single-particle (Stokes) settling velocity, so measurements of settling velocity in the cloud configuration gives an unreliable estimate of the particle density. Small polydispersity has the effect of destabilising the initial cloud, but a cloud still forms and breaks up into smaller clouds that also have a velocity larger than the Stokes velocity. However, if the polydispersity

is large, an initially spherical particle cloud quickly disintegrates. Upon disintegration, the velocity approach the Stokes velocity.

In Fig. 5.10(a) we show a snapshot of a dynamic simulation of a polydisperse suspension of 949 particles initially confined within a sphere. The initial volume fraction is 1%. The particle sizes are distributed according to the discrete logarithmic size distribution shown in Fig. 5.10(b). Because of the large polydispersity (the parameter σ characterising the log-normal is 0.32, while the mean radius is 0.94) the initial spherical cloud has lost its coherence in shape in a comparatively short time. The cloud has disintegrated, leaving a trail of small particles (seen at the top of the image) that settle essentially with their velocity of the same order of the Stokes velocity (but still larger). The larger particles near the bottom still experience hydrodynamic interactions and settle at a velocity larger than the Stokes velocity.

Particles in the tail give a particularly good measure of the Stokes velocity, which becomes better and better as time progresses. This trend is demonstrated in Fig. 5.11, which the velocity of each particle size distinguishing between trail particles (in red) and particles in the core of the cloud (blue) for $\phi = 1\%$. If the distance between a particle and the average position of all the particles is larger than the radius of the initial cloud, this particle is considered as a trail particle. Otherwise it is considered as in the cloud. The red dots approach in time the continuous line indicating the Stokes prediction. The figure also shows that the largest (heaviest) particles in the trail offer the best agreement with the Stokes velocity. This is because the hydrodynamic influence of the smallest particles in a polydisperse distribution on the large particles is relatively weak [34]. The small particles “feel” the influence of the large particles, but not vice versa. This also explains why in the experiments of Ali, Kirichek, and Chassagne [14] the estimation of the effective density of the smallest flocs had a larger variance for the small flocs than for the large flocs. From figure 5.11 it is also apparent that the velocity of the particle belonging to the core of the cloud is almost independent of the particle size.

How long does it take for a polydisperse cluster to disintegrate? The time for disintegration depends on the initial volume fraction. For example, for $\phi = 0.01\%$ and $\phi = 0.001\%$ no typical cloud evolution behaviour (with a toroidal vortex) is observed in our dynamic simulations, regardless of the number of particles in the cloud. For $\phi = 0.1\%$, the evolution follows initially a typical cloud behavior for $N = 250$ until the cloud disintegrates. For monodisperse particle clouds, Ho et al. [37] found that the cloud breakup time is in the range $500 - 1200\tau_c$, where $\tau_c = R_0 / \langle u \rangle$ is the time it takes for a spherical cloud of radius R_0 to travel a distance R_0 when moving with a velocity $\langle u \rangle = 4/15\phi\Delta\rho gR^2/\mu$ (equal to equation (5.2) when $\phi \ll \alpha/R$). For a Gaussian distribution of at least 1500 particles, they found a smaller breakup time in the range 200-700 τ_c . For number of particles smaller than 1000, they found that cloud destabilisation was “difficult to be detected or even does not occur in some

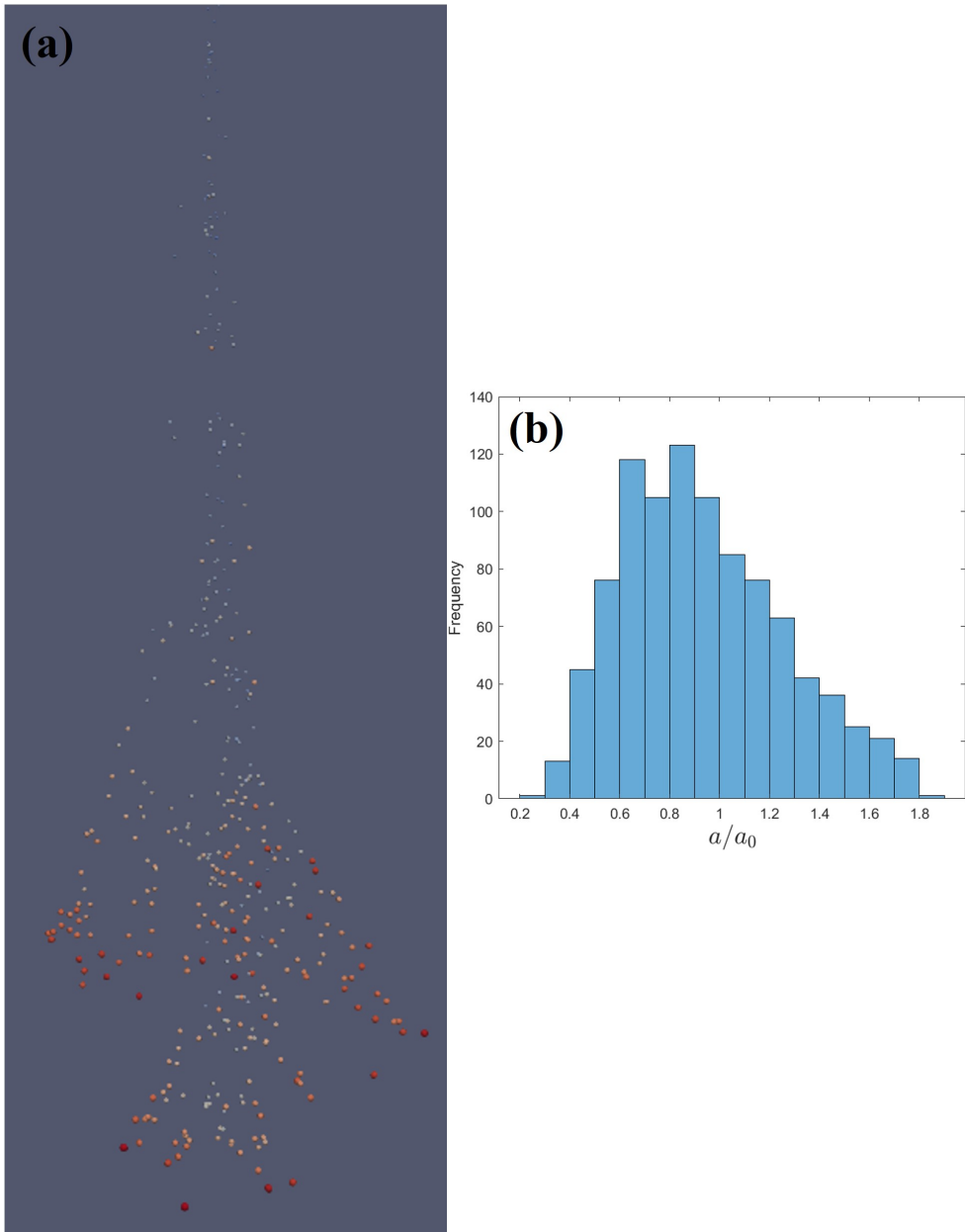


Figure 5.10: (a) A snapshot of a dynamic simulation of a settling polydisperse cloud. Particles are colored according to their sizes. (b) Particle size distribution used in the dynamic simulation. The mean value and standard deviation of the particle radius is 0.94 and 0.32, respectively.

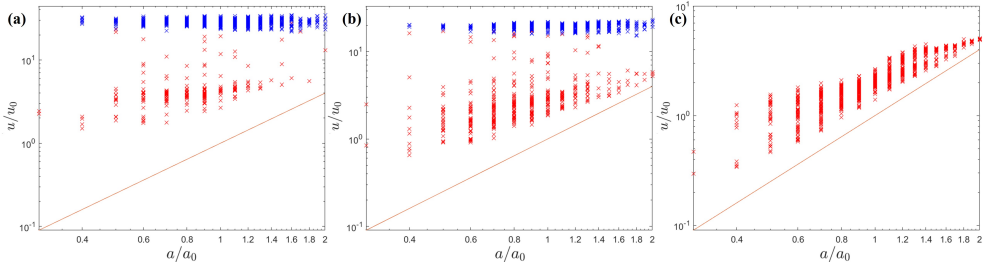


Figure 5.11: Particle velocities for different size classes at three different times in the dynamic simulation. Blue symbols are for the particles in the cloud, red symbols are for the particles in the trail, and the red lines are the Stokes velocities.

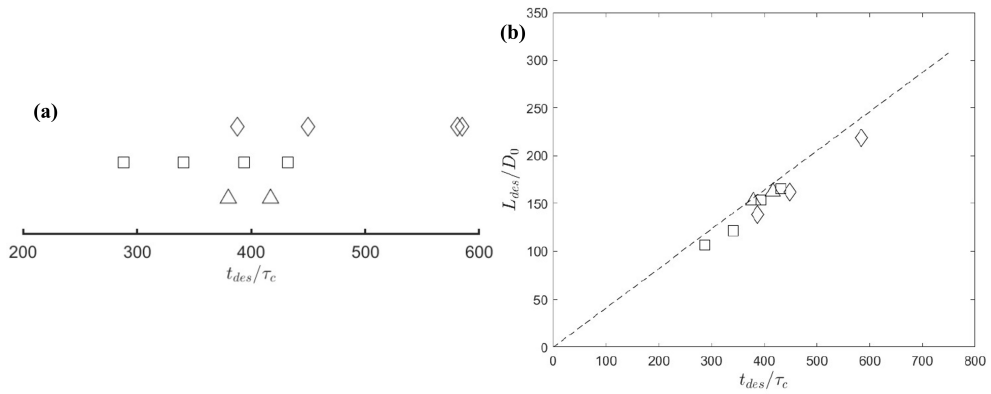


Figure 5.12: (a) The destabilization times from different dynamic simulations. Triangles for monodisperse clouds, squares and diamonds for polydisperse clouds. (b) The destabilization length versus the destabilization time of the cloud. Symbols are the results of our dynamic simulations, and the dashed line is the correlation given in the Ref.[37].

realizations”. This result is compatible with our observation of absence of conventional breakup for extremely small volume fractions when the particle distribution is lognormal with a large variance.

In an experiment, most interesting is the destabilisation length L_{des} , as this sets the position where the camera should be placed. Fig. 5.12 shows $L_{des}/D_0 = L_{des}/(2R_0)$ vs the normalised destabilisation time t_{des}/τ_c as measured in our simulations, against the correlation for $L_{des}/D_0 = 0.41 t_{des}/\tau_c$ developed by Ho et al. [37]. This correlation provides a reasonably good fit to the data. Taking a lower bound $t_{des}/\tau_c \simeq 200$, we find $L_{des}/D_0 \simeq 82$. For the experiments of Fig. 5.2 we use a rectangular outlet $2\text{mm} \times 10\text{mm}$ to inject the particles. Using for D_0 the average dimension of the outlet 6mm we get $L_{des} \simeq 49.2\text{cm}$, almost two times larger than the value we use for the placement of the camera in the experiments of Fig. 5.2. A much taller column, or a much smaller particle volume fraction, would have been needed to avoid

hydrodynamic interaction effects in the measurement of the settling rate by the pipette method.

5.5 Conclusions

In this paper we use simulation results of cloud of particles sedimenting at low Reynolds number in an unbounded fluid to evaluate the effect of collective particle interactions on the increase in settling rate over the single-particle (Stokes) settling rate formula. Experiments with spherical particles are also carried out to motivate the study and indicate trends in the data that the simulations aim to explain. The experiments are done with the same FLOCCAM setup that has been used in previous publications to evaluate the density of environmental flocs.

Previous experiments with flocs suggest that the values of effective floc density, ρ_{eff} , obtained by fitting the Stokes formula to the measured settling velocity data, are incompatible with the intrinsic density of the solid component of the floc, ρ_s . A truly isolated particle settles with a velocity proportional to the radius of the particle squared, yielding a particle density $\rho_p = \rho_f + \frac{9}{2}\mu u_0/(ga^2)$. However, the method to introduce particles in a settling column intrinsically leads to the formation of a particle cloud. In this case the particle settles approximately with the velocity of the cloud, which scales proportionally to the squared radius of the cloud R^2 and is thus much larger than the single particle settling rate. This, in turn, gives rise to an overestimation of the effective density. From Eq. (5.2), the measured particle density in the collective settling case satisfies approximately $\frac{\rho_{coll}}{\rho_s} \simeq 1 + \frac{6}{5}\frac{R^2}{a^2}\phi$, assuming $R/a \gg 1$. This equation can be used to correct the density estimation and obtain ρ_s from ρ_{coll} , provided that a measurement of the instantaneous size of the cloud and of the corresponding (local) volume fraction of particles in the cloud (or, alternatively, of the average interparticle distance) are available. Experimentally, this could be achieved by using two cameras with different fields of view allowing the resolution of the typical interparticle separation and the visualisation of the cloud as a whole.

The origin of the increased settling rate is of course purely hydrodynamic. The dependence of hydrodynamic interactions on the particle configuration should be a warning to draw conclusions from experimental estimates of the density that do not consider the way the particles are suspended. For example, if the particles were homogeneously distributed in the settling tank, the settling rate would decrease for increasing ϕ [39, 41]. The fact that the particles form a cloud of finite extent smaller than the width of the settling column is thus essential. Sketch Fig. 5.13 illustrates the two types of “collective settling”, giving rise to either hindered settling (for a suspension that spans the width of the settling column) or enhanced settling.

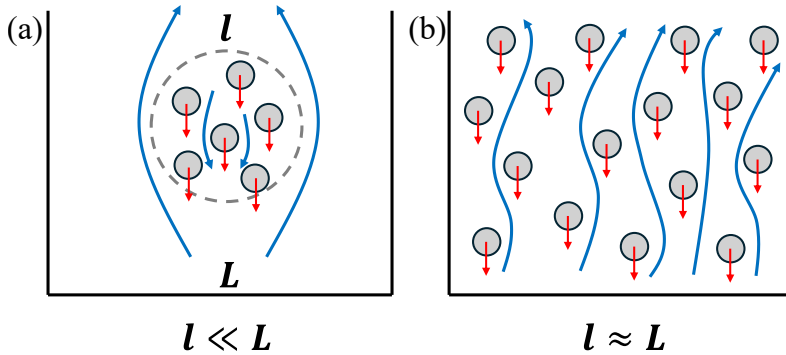


Figure 5.13: Sketches showing (a) collective settling of particles, and (b) hindered settling of a suspension. Blue lines with arrows represent the fluid streamlines, and red arrows show the particle moving direction. l is the size of the particle group (i.e. the diameter of the grey dashed circle enclosing the particles in (a)), and L is the lateral size of the container.

Other essential ingredients highlighted in the paper are the expansion of the cloud during settling (which increases R and thus reduces ϕ for a given number of particles), the cloud breakup at a critical time (see Fig. 5.12) and the dispersion in the velocity values for different particles belonging to the same cloud. For a widely polydisperse cloud at very low volume fractions, the particles in the tail are largely isolated from hydrodynamic interaction with the core of the cloud, and therefore their settling rate is much closer to the Stokes settling rate than the rest of the cloud, as our simulations demonstrate. The velocities of the particles in the core instead have been found to be largely uncorrelated with the particle size. For this latter particle sub-population the approach of mapping the particle density to the particle velocity is intrinsically flawed. Finding methods to distinguish trail from core particles experimentally would give a better estimation of the density. This in fact is quite challenging because, as shown in Fig. 5.10(a), a highly polydisperse cloud does not appear as an easily identifiable spherical blob. Again, it seems that the analysis of experimental images would benefit from viewing the particle distribution both at the level of the single particle and at the much larger scale of the cloud. Furthermore, the data recorded should include the position of the sample particle with respect to the center of mass of the cloud.

REFERENCES

- [1] Weizhou Jiao, Shuai Luo, Zhen He, and Youzhi Liu. “Applications of high gravity technologies for wastewater treatment: a review.” In: *Chemical Engineering Journal* 313 (2017), pp. 912–927.
- [2] Scott C James, Craig A Jones, Matthew D Grace, and Jesse D Roberts. “Advances in sediment transport modelling.” In: *Journal of Hydraulic Research* 48.6 (2010), pp. 754–763.
- [3] Nicola Mingotti and Andrew W Woods. “Stokes settling and particle-laden plumes: implications for deep-sea mining and volcanic eruption plumes.” In: *Philosophical Transactions of the Royal Society A* 378.2179 (2020), p. 20190532.
- [4] Robert C Hale, Meredith E Seeley, Mark J La Guardia, Lei Mai, and Eddy Y Zeng. “A global perspective on microplastics.” In: *Journal of Geophysical Research: Oceans* 125.1 (2020), e2018JC014719.
- [5] Anthony L Andrady. “Microplastics in the marine environment.” In: *Marine Pollution Bulletin* 62.8 (2011), pp. 1596–1605.
- [6] Jingyi Li, Huihui Liu, and J Paul Chen. “Microplastics in freshwater systems: A review on occurrence, environmental effects, and methods for microplastics detection.” In: *Water Research* 137 (2018), pp. 362–374.
- [7] Hadeel Al-Zawaidah, Merel Kooi, Ton Hoitink, Bart Vermeulen, and Kryss Waldschlager. “Mapping Microplastic Movement: A Phase Diagram to Predict Nonbuoyant Microplastic Modes of Transport at the Particle Scale.” In: *Environmental Science & Technology* (2024).
- [8] Zijian Yu, Ge Yang, and Wenming Zhang. “A new model for the terminal settling velocity of microplastics.” In: *Marine Pollution Bulletin* 176 (2022), p. 113449.
- [9] Stefan Dittmar, Aki S Ruhl, and Martin Jekel. “Optimized and Validated Settling Velocity Measurement for Small Microplastic Particles (10–400 μm).” In: *ACS ES&T Water* 3.12 (2023), pp. 4056–4065.
- [10] Stefan Dittmar, Aki S Ruhl, Korinna Altmann, and Martin Jekel. “Settling Velocities of Small Microplastic Fragments and Fibers.” In: *Environmental Science & Technology* 58.14 (2024), pp. 6359–6369.

- [11] Koray Deniz Goral, Hasan Gokhan Guler, Bjarke Eltard Larsen, Stefan Carstensen, Erik Damgaard Christensen, Nils B Kerpen, Torsten Schlurmann, and David R Fuhrman. “Settling velocity of microplastic particles having regular and irregular shapes.” In: *Environmental Research* 228 (2023), p. 115783.
- [12] David Kaiser, Arne Estelmann, Nicole Kowalski, Michael Glockzin, and Joanna J Waniek. “Sinking velocity of sub-millimeter microplastic.” In: *Marine Pollution Bulletin* 139 (2019), pp. 214–220.
- [13] Liliya Khatmullina and Irina Chubarenko. “Thin synthetic fibers sinking in still and convectively mixing water: laboratory experiments and projection to oceanic environment.” In: *Environmental Pollution* 288 (2021), p. 117714.
- [14] W Ali, Alex Kirichek, and C Chassagne. “Collective effects on the settling of clay flocs.” In: *Applied Clay Science* 254 (2024), p. 107399.
- [15] AJ Manning, JV Baugh, RL Soulsby, JR Spearman, and RJS Whitehouse. “Cohesive sediment flocculation and the application to settling flux modelling.” In: *Sediment Transport* (2011), pp. 91–116.
- [16] A Manning. “LabSFLOC-2—The second generation of the laboratory system to determine spectral characteristics of flocculating cohesive and mixed sediments.” In: *UK: HR Wallingford Ltd* (2015).
- [17] Kelsey A Fall, Carl T Friedrichs, Grace M Massey, David G Bowers, and S Jarrell Smith. “The importance of organic content to fractal floc properties in estuarine surface waters: Insights from video, LISST, and pump sampling.” In: *Journal of Geophysical Research: Oceans* 126.1 (2021), e2020JC016787.
- [18] Michael Glockzin, Falk Pollehne, and Olaf Dellwig. “Stationary sinking velocity of authigenic manganese oxides at pelagic redoxclines.” In: *Marine Chemistry* 160 (2014), pp. 67–74.
- [19] Thomas Peacock and Raphael Ouillon. “The fluid mechanics of deep-sea mining.” In: *Annual Review of Fluid Mechanics* 55.1 (2023), pp. 403–430.
- [20] Eckart Meiburg and Ben Kneller. “Turbidity currents and their deposits.” In: *Annual Review of Fluid Mechanics* 42.1 (2010), pp. 135–156.
- [21] Patrick J Snyder and Tian-Jian Hsu. “A numerical investigation of convective sedimentation.” In: *Journal of Geophysical Research: Oceans* 116.C9 (2011).
- [22] JM Nitsche and GK Batchelor. “Break-up of a falling drop containing dispersed particles.” In: *Journal of Fluid Mechanics* 340 (1997), pp. 161–175.
- [23] ML Ekiel-Jezewska, B Metzger, and E Guazzelli. “Spherical cloud of point particles falling in a viscous fluid.” In: *Physics of Fluids* 18.3 (2006).

- [24] Bloen Metzger, Maxime Nicolas, and Élisabeth Guazzelli. “Falling clouds of particles in viscous fluids.” In: *Journal of Fluid Mechanics* 580 (2007), pp. 283–301.
- [25] W Ali and C Chassagne. “Comparison between two analytical models to study the flocculation of mineral clay by polyelectrolytes.” In: *Continental Shelf Research* 250 (2022), p. 104864.
- [26] W Ali, D Enthoven, Alex Kirichek, C Chassagne, and R Helmons. “Effect of flocculation on turbidity currents.” In: *Frontiers in Earth Science* 10 (2022), p. 1014170.
- [27] W Ali, D Enthoven, Alex Kirichek, C Chassagne, and R Helmons. “Can flocculation reduce the dispersion of deep sea sediment plumes?” In: *Proceedings of the World dredging conference, Copenhagen, Denmark* (2022).
- [28] Leiping Ye, Andrew J Manning, and Tian-Jian Hsu. “Oil-mineral flocculation and settling velocity in saline water.” In: *Water Research* 173 (2020), p. 115569.
- [29] Andrew J. Manning, P.L. Friend, N. Prowse, and Carl L. Amos. “Estuarine mud flocculation properties determined using an annular mini-flume and the LabSFLOC system.” In: *Continental Shelf Research* 27.8 (2007), pp. 1080–1095.
- [30] W Ali, A Kirichek, and C Chassagne. “Flocculation of deep-sea clay from the Clarion Clipperton fracture zone.” In: *Applied Ocean Research* 150 (2024), p. 104099.
- [31] M.R. MacIver. *Safas: Sedimentation and floc analysis software*. 2019.
- [32] Louis Durlofsky, John F Brady, and Georges Bossis. “Dynamic simulation of hydrodynamically interacting particles.” In: *Journal of Fluid Mechanics* 180 (1987), pp. 21–49.
- [33] John F Brady, Georges Bossis, et al. “Stokesian dynamics.” In: *Annual Review of Fluid Mechanics* 20.1 (1988), pp. 111–157.
- [34] Heng Li and Lorenzo Botto. “Hindered settling of a log-normally distributed Stokesian suspension.” In: *Journal of Fluid Mechanics* 1001 (2024), A30.
- [35] Jens Rotne and Stephen Prager. “Variational treatment of hydrodynamic interaction in polymers.” In: *The Journal of Chemical Physics* 50.11 (1969), pp. 4831–4837.
- [36] Pawel J Zuk, E Wajnryb, KA Mizerski, and P Szymczak. “Rotne–Prager–Yamakawa approximation for different-sized particles in application to macromolecular bead models.” In: *Journal of Fluid Mechanics* 741 (2014), R5.

- [37] Think X Ho, Nhan Phan-Thien, and Boo Cheong Khoo. “Destabilization of clouds of monodisperse and polydisperse particles falling in a quiescent and viscous fluid.” In: *Physics of Fluids* 28.6 (2016).
- [38] E. Wacholder and N. F. Sather. “The hydrodynamic interaction of two unequal spheres moving under gravity through quiescent viscous fluid.” In: *Journal of Fluid Mechanics* 65.3 (1974), pp. 417–437.
- [39] T.A. Brzinski III and D.J. Durian. “Observation of two branches in the hindered settling function at low Reynolds number.” In: *Physical Review Fluids* 3.12 (2018), p. 124303.
- [40] Melissa Faletra, Jeffrey S Marshall, Mengmeng Yang, and Shuiqing Li. “Particle segregation in falling polydisperse suspension droplets.” In: *Journal of Fluid Mechanics* 769 (2015), pp. 79–102.
- [41] Claire Chassagne. *Introduction to colloid science: Applications to sediment characterization*. DOI: <https://doi.org/10.34641/mg.16>, 2021.

6

BUCKLING OF FLEXIBLE SHEETS IN SHEAR FLOW

In previous chapters, dilute suspensions of polydisperse spheres are studied. Since the suspensions are dilute, the particles are far from each other and the hydrodynamic interactions have weak dependence on the particle shape. In this chapter, the effect of hydrodynamic interactions on the buckling of a pair of flexible sheets in the shear flow is studied, using both experiments and simulations. The sheets are positioned parallel and close to each other and the deformation is measured at the particle scale. The experiments are carried out by a former postdoc in our group.

This chapter is based on the article:

H. Perrin*, H. Li* and L. Botto. “Hydrodynamic interactions change the buckling threshold of parallel flexible sheets in shear flow.” In: *Phys. Rev. Fluids* 8 (2023), 124103.

* denotes equal contribution

6.1 Introduction

Soft biological or synthetic objects, such as cells, lipid bilayers, macromolecules, and nanoparticles, can deform when suspended in sufficiently strong shear or extensional flows [1–4]. Predicting flow-induced morphological changes is crucial in many fields, ranging from biophysics, where swimming of micro-organisms relies on fluid-structure interactions [5], to soft matter physics, where the rheological response of a particulate suspension is affected by the instantaneous particle shape [6]. Model studies in canonical flows have provided profound physical insights of general applicability. For example, the theoretical prediction of the coil-stretch transition of polymers in simple shear flow [7, 8] was instrumental in the development of rheological models for dilute polymer solutions [9].

The recent need to develop liquid-based methods to process two-dimensional (2D) nanomaterials [10–12] has triggered new interest on the effect of flow on the morphology of sheet-like materials [3, 10, 11, 13–17]. Two-dimensional materials have low bending moduli and therefore can undergo transient or permanent buckling in flow [3]. Recent numerical studies [3, 18] demonstrate that purely mechanical models based on the competition between hydrodynamic compressive force and elastic-bending forces can capture the change of morphology of isolated graphene sheet and 2D polymers suspended in a simple shear flow. This agreement demonstrates that the morphology of a single sheet is determined by a buckling instability whose threshold depends, for a given fluid shear rate and viscosity, only on the bending modulus and length of the sheet. However, the extension of this result to suspensions of many particles is an open question. Because of their relatively large contact area, sheet-like particles are prone to stacking at small inter-particle separations [11, 19]. Hydrodynamic interactions between nearly parallel sheets are thus expected to alter the buckling dynamics predicted for single sheets.

In this study we investigate parallel pairs of flexible sheets in a shear flow as a function of their separation distance, and study how the buckling instability threshold depends on hydrodynamic interactions. By performing model experiments, and interpreting the results with the help of boundary-integral simulations and theoretical modeling, we demonstrate that hydrodynamic interactions can trigger bending far below the buckling threshold of a single sheet. Hydrodynamic interactions cannot therefore be considered second-order effects when predicting the morphology of flexible sheets in flow. More specifically, our simulations and theoretical modeling show that the dipolar disturbance flow field induced by each sheet gives rise to a lateral hydrodynamic force. This lateral force modifies the mechanical response of the sheet pair to the compressive axial hydrodynamic force experienced when the pair is oriented in the compressional quadrant of the shear flow. On the other hand, for small separations, the lubrication forces overcome this dipolar contribution and prevent bending. These

two competing effects result in a non-monotonic relation between interparticle distance and critical shear rate for buckling. More generally, our results suggest that the deformation of close sheets in a suspension may not only depend on the mechanical and geometric properties of each sheet but also strongly on the pair-particle separation and thus on the concentration.

6.2 Experiments

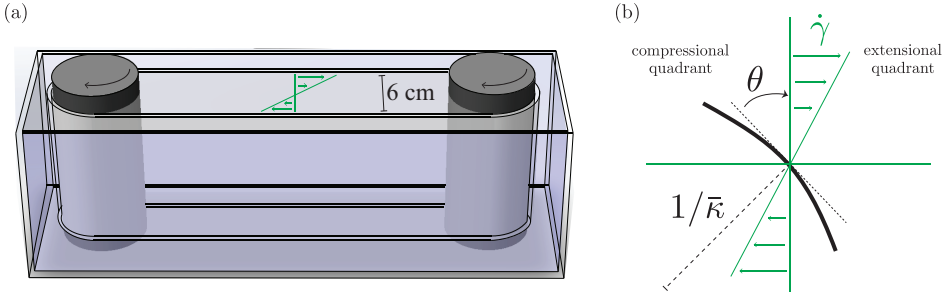


Figure 6.1: (a) Schematic of the shear cell. (b) Schematic of a buckled sheet viewed along the vorticity direction of the shear flow and definition of the mid-point orientation angle θ and mid-point curvature $\bar{\kappa}$. The compressional quadrant and the extensional quadrant are shown. In this schematic, the sheet is oriented in the compressional quadrant ($-\pi/2 < \theta < 0$).

Mylar sheets (Young's modulus $E \simeq 4$ GPa) of different thicknesses ($h = 23, 50$ and 125 μm), width $w = 1$ cm and length L ranging from 1 to 4 cm were used. Corresponding sheet bending moduli are $B \simeq 5.0 \times 10^{-6}, 5.0 \times 10^{-5}$, and 8.1×10^{-4} J ($B = Eh^3/12(1 - \nu^2)$ where $\nu \simeq 0.5$ is the Poisson's ratio). The shear cell is composed of a belt driven by two co-rotating cylinders of diameter 6 cm – see fig.6.1(a). A motor, connected to one of the cylinders, imposes a controlled shear rate in the range $\dot{\gamma} = 0.4 - 10$ s^{-1} . The design of the shear cell is essentially identical to the one described in Ref. [20], so we refer to that publication for construction details. The flow cell allows to generate a flow that, in the central region away from the cylinders, is essentially a two-dimensional simple shear flow (the flow profile was measured by Particle Image Velocimetry, see Appendix C). We considered single sheets, and pairs of parallel sheets with separation distance d varying in the range $d/L = 0.03 - 1$. The sheets were placed in glycerol (the viscosity is $\eta \simeq 1$ Pa.s and the density is $\rho \simeq 1.2 \times 10^3$ kg.m^{-3}). Mylar is slightly more dense than glycerol, and the difference between their densities is $\Delta\rho \simeq 10^2$ kg.m^{-3} . The sedimentation time over one sheet length is of the order of 10^3 s, which is about $100\dot{\gamma}^{-1}$ for the lowest shear rate. Furthermore, the

sedimentation is in the vorticity direction so the motion of the sheet along the vertical direction does not affect the essentially two-dimensional dynamics of the sheets. The maximum Reynolds number $Re = \rho\dot{\gamma}L^2/\eta$ is of order 1 at the maximum shear rate. The sheets were immersed in the liquid when the belts were not in motion (zero flow velocity), and manipulated with tweezers so that their normal was in the plane of the flow. When studying sheet pairs, the sheets were placed parallel to each other and the separation distance d measured. After placing the sheets, the motor driving the belts was switched on. Data from experiments in which the sheets were not sufficiently parallel were discarded. The criterion for parallelism was that the initial angle between the two sheets must not be greater than 2° . During the dynamics, the normal vector remains in the flow-gradient plane and thus the dynamics is two-dimensional. Optical measurements with a camera were carried out from the top, i.e. along the vorticity direction of the undisturbed shear flow, with a time resolution of 0.1 s and with a spatial resolution of 25 $\mu\text{m}/\text{pixel}$. Sheet profile detection is performed manually using imageJ software. We extracted the midpoint orientation angle $\theta(t)$ by fitting a line to each sheet's profile – see fig.6.1(b). The mid-point curvature $\bar{\kappa}(t)$ was obtained by fitting a parabola to each sheet's profile. We detected and analyzed sheet profiles at maximum temporal resolution only when there was a significant temporal variation in angle or curvature. For this reason, the temporal density of data points seen in the graphs is not uniform. As explained in section 2 of the Appendix C, for the few (about one in a hundred) images that were not captured due to a camera software problem, we used linear interpolation to account for the small temporal gap between images. Even though the maximum Re is of order 1, in analyzing the results we will consider a low Reynolds approximation (Stokes flow). As it will appear later, this approximation gives a reasonable agreement between the simulations and the experimental data. For each case, the experiment was repeated 2 to 3 times, and all the results are shown in the figures presented below.

6.3 Simulation Method

We simulated the fluid-structure interaction of thin sheets in Stokes flow by a regularized Stokeslet approach [17, 21–23]. The regularized Stokeslet method has been used to study a variety of fluid-structure interaction problems at low Reynolds number, including cilia-driven transport [21], flagella synchronization [22], and flow around double helices [23]. As in the experiment the flow and the sheet dynamics are two-dimensional, we simplified the simulation choosing a two-dimensional description. For a two-dimensional slender body, the approach consists in placing regularized force singularities along the body's centerline. The integral of the regularized force density over each discretization line segment represents the force exerted by that segment of

the slender body on the fluid. Owing to the linearity of the Stokes equation, the velocity field $\mathbf{u}(\mathbf{x}, t)$ at position \mathbf{x} and time t obeys the following boundary integral equation [24]:

$$\mathbf{u}(\mathbf{x}, t) = \mathbf{u}^\infty(\mathbf{x}) + \frac{1}{4\pi\eta} \int_C \mathbf{G}_\epsilon(\mathbf{x}, \mathbf{x}_0) \cdot \mathbf{f}(\mathbf{x}_0, t) d\mathbf{l}, \quad (6.1)$$

where \mathbf{u}^∞ is the undisturbed background flow, η is the dynamic viscosity, $\mathbf{f}(\mathbf{x}_0, t)$ is the force density exerted on the fluid by the sheet element $d\mathbf{l}$ centered at \mathbf{x}_0 and \mathbf{G}_ϵ is a 2D regularized Stokeslet for an unbounded flow [25]. Here, we neglected the double-layer potential because of the inextensibility approximation for the sheets [17, 23]. Since the sheets are inertia-less, the hydrodynamic force ($-\mathbf{f}$) is balanced by the local internal elastic force. Numerically, we compute the elastic force from the derivative of the bending energy, as done in [17, 22, 26]. A very large value of the spring stretching constant was used to model the inextensibility of the sheets. The maximum relative elongation of the sheet during the dynamics was typically not larger than 10^{-3} . The kinematics of each sheet is governed by the no-slip boundary condition on the surface of the sheet. In the slender body approximation, this condition is approximated by a no-slip condition at the centerline of the sheet:

$$\frac{\partial \mathbf{X}(s, t)}{\partial t} = \mathbf{u}(\mathbf{X}(s, t)), \quad (6.2)$$

where $\mathbf{X}(s, t)$ is the position vector along the centerline of the sheet at the curvilinear coordinate s and time t . In this numerical method the sheet has zero thickness, therefore in order to observe tumbling and bending, the sheet needs to be initialized at an orientation angle different from $\pm\pi/2$ and the initial shape set to a perturbation from a straight line [27]. Based on our previous work [17] we chose for the initial orientation $\theta_0 = -\pi/2 + \pi/10$ and for the initial shape perturbation the first buckling mode $\kappa(s) = \kappa_0 \sin(s\pi/L)$ with a small amplitude $\kappa_0 = 8 \times 10^{-3}/L$, where $\kappa(s)$ is the local curvature at s . At each time step, the velocity field is calculated first by eq.(6.1), then eq.(6.2) is advanced in time by a first-order explicit Euler scheme to obtain the sheet's configuration at the new time step. In the simulations, each sheet is discretized by 51 nodes and the time step is $10^{-5}\dot{\gamma}^{-1}$. Validations of the code on two cases for which asymptotic solutions are known can be found in our previous article [17]. Those two cases are the relaxation of an initially deformed sheet in a quiescent flow and the tumbling dynamics of a single sheet in a shear flow. During the simulation, at each time step the mid-point curvature $\bar{\kappa}(t) = \kappa(s = L/2, t)$ of a sheet is calculated by fitting a parabola to its center.

6.4 Dynamics of a single sheet

For an inextensible flexible sheet of length L , width w and bending modulus B , the Euler buckling force for axial compression scales proportionally to wB/L^2 [28, 29]. The viscous compressive force in a shear flow in the Stokes limit scales as $\eta\dot{\gamma}Lw$. Its dependence on the orientation angle is $-2\sin\theta\cos\theta$ [3, 30], which is maximum when the sheet is oriented along the compressional axis $\theta = -\pi/4$ of the shear flow (see fig.6.1(b)). The buckling dynamics of a single flexible sheet depends therefore on the elasto-viscous number [3]

$$E_v = \frac{\eta\dot{\gamma}L^3}{B}. \quad (6.3)$$

This non-dimensional number can be also interpreted as the ratio of two time scales: $1/\dot{\gamma}$, the characteristic time scale of the shear flow, and $\eta L^3/B$, the characteristic time scale of curvature relaxation in a quiescent viscous liquid.

We determined the single-sheet buckling threshold by measuring experimentally the sheet curvature $\bar{\kappa}$ corresponding to different elasto-viscous numbers, placing only one sheet in the shear cell. The Mylar sheet is practically perfectly flat when not subject to external forces. The residual curvature of each sheet, if at all present, is at most $0.02/L$. For small elasto-viscous numbers, the sheet tumbles in the flow and remains straight. For relatively large elasto-viscous numbers, for example $E_v \simeq 21$ (fig.6.2(a)), the sheet deforms during tumbling. The time dependence of the angle $\theta(t)$ in fig.6.2(a) is well described by Jeffery's solution for rigid oblate ellipsoids [3, 31, 32]. This agreement validates the Stokes flow assumption we made for the simulations. This agreement also shows that the tumbling dynamics is not significantly affected by the sheets deformations for curvatures smaller than $1/L$. The time-dependent curvature is seen to grow when the sheet is oriented in the compressional quadrant ($-\pi/2 < \theta < 0$), which is the signature of the buckling instability. Then the curvature decays to zero, over a time scale $1/\dot{\gamma}$. It is interesting to note that the curvature decays also in the compressional quadrant, likely because for ($-\pi/4 < \theta < 0$), the hydrodynamic forces are predominantly compressive but their magnitude is below the threshold for buckling. As $\theta(t)$ spans the extensional quadrant ($0 < \theta < \pi/2$), the curvature decays monotonically to zero. To identify the single-sheet buckling threshold, we measured the maximum curvature $\bar{\kappa}_{\max}$ attained during a tumbling cycle for different elasto-viscous numbers (see fig.6.2(b)). The results lie in two regions separated by a critical elasto-viscous number $E_v^c \simeq 11 \pm 3$ above which the sheet always deforms with a curvature larger than the experimental resolution. The maximum curvature measured in experiments seems to increase proportionally to E_v^2 , see the Appendix C for a log-log version of fig.6.2(b). Below this number the sheets curvature is negligible. We defined the critical value of E_v as the threshold value above which sheets always deform. The

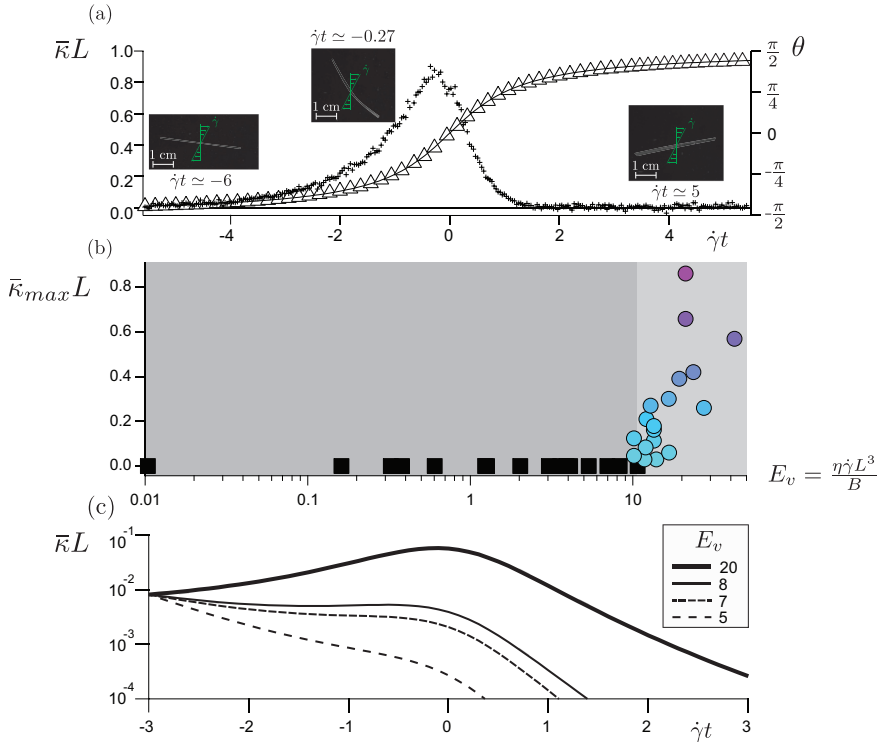


Figure 6.2: (a) Normalized mid-point curvature $\bar{\kappa}L$ (crosses) and mid-point orientation angle θ (triangular markers) versus rescaled time $\dot{\gamma}t$ for $E_v \simeq 21$. Time has been shifted so that $\dot{\gamma}t = 0$ corresponds to the orientation $\theta = 0$. The black line is Jeffery's prediction $\theta(t) = \arctan(\dot{\gamma}t)$ [31]. (b) Maximum normalized curvature versus elasto-viscous number for a single sheet. The dark and light grey regions delimit the rigid limit and the buckling region, respectively. The measured critical elasto-viscous number from this diagram is $E_v^c \simeq 11$. (c) Normalized curvature versus normalized time from dynamic simulations of a single sheet for different elasto-viscous numbers.

uncertainty in the determination of E_v^c was estimated from the dispersion of the data points, see Appendix C for a log-log version of fig.6.2(b). To corroborate this observation, we performed numerical simulations of single sheets for different elasto-viscous numbers, see fig.6.2(c). For elasto-viscous numbers larger than $E_v = 8$, the curvature increases in time, signature of the growth of the buckling instability. For elasto-viscous numbers smaller than $E_v = 8$, the curvature decays. The simulations confirm that the maximum curvature increases approximately as $\sim E_v^2$ for relatively small values of E_v , see the Appendix C. The agreement between the numerical prediction ($\simeq 8$) and the experimental value ($\simeq 11$) is acceptable considering the finite experimental resolution, which makes a very precise determination of the buckling threshold difficult [30]. A mathematical model for the buckling of a thin flexible circular disk, based on applying Jeffery's solution for the hydrodynamic stress on an oblate ellipsoids to predict the compressive load on the disk, predicted a threshold values $\simeq 10^2$ [33]. Recent simulations of an hexagonal flexible sheet modeled as a collection of beads interacting via long-range hydrodynamic interactions - represented at the Rotne-Prager-Yamakawa level - suggested a critical buckling threshold in simple shear flow of about 50 [3]. Since both the hydrodynamic compressive force and the elastic response of the sheet depend on the shape, it is expected that the buckling threshold for rectangular sheets is different than the ones for circular disks or hexagonal sheets, so differences with published work are expected. The experimental determination of the buckling threshold for single rectangular sheets, confirmed by our numerical simulation, is an important step that provides a reference case for the study of pairs of parallel sheets.

6.5 Dynamics of a pair of parallel sheets

A body formed by two sheets bonded together by adhesion or friction has a larger bending rigidity than a single sheet [29, 34, 35]. Therefore one may intuitively assume that two sheets separated by a layer of viscous liquid would have a larger buckling threshold than a single sheet. In contrast, we found that a pair of parallel sheets can deform for values of E_v below the single-sheet threshold. For example, for $E_v \simeq 3.6$ the single-sheet curvature is negligible (see fig.6.2(b) and fig.6.3(a)¹) while for the same parameter two sheets separated by $d/L \simeq 0.2$ display a finite curvature. The curvature of the two sheets increases with time, then decreases, changes sign and finally decays to zero at the end of the tumbling motion (see fig.6.3(a)). In the single-sheet case, for $E_v > E_v^c$ the curvature relaxes while the sheet is oriented in the extensional quadrant (see fig.6.2(a)). In contrast, pair of sheets deform while oriented in the extensional quadrant (fig.6.3(b) right panel). These two changes of behavior for

¹ Four experimental data points are missing at $\dot{\gamma}t \simeq 0.17$ and $\dot{\gamma}t \simeq 5.4$ due to a camera software issue, which does not influence our observation of the concave and convex shape.

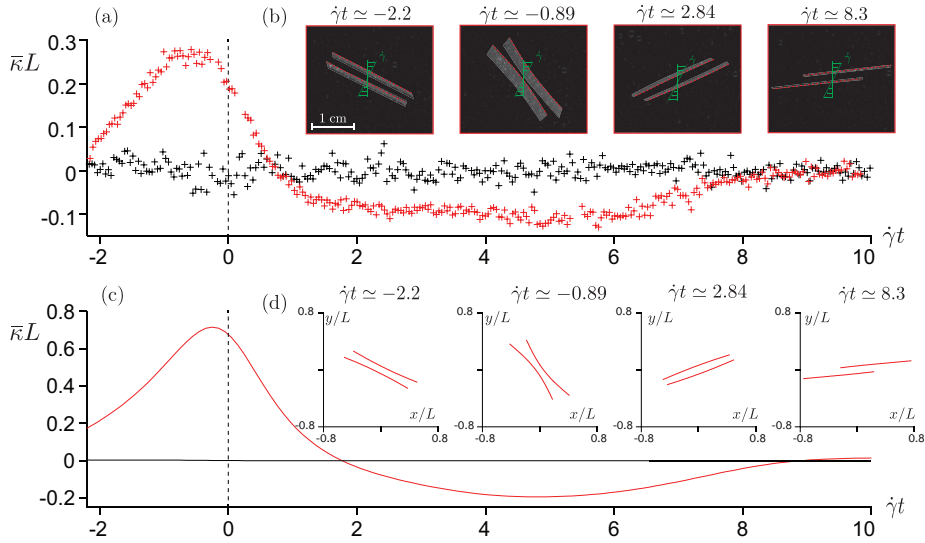


Figure 6.3: Comparison between single sheet dynamics and dynamics of a pair of parallel sheets below the single-sheet buckling threshold. (a) Experimental normalized curvature $\bar{\kappa}L$ versus normalized time $\dot{\gamma}t$ for a single sheet (in black) and a sheet pair separated by $d/L \simeq 0.2$ (in red) for $E_v \simeq 3.6$. (b) Images of a pair of parallel sheets at two selected times. (c) Normalized curvature $\bar{\kappa}L$ versus normalized time $\dot{\gamma}t$ for simulation of a single sheet (in black) and a pair of sheets separated by $d/L = 0.1$ (in red) for $E_v = 7$. (d) Simulated shapes of a pair of parallel sheets corresponding to the two selected times of fig.6.3(b).

a pair of sheets, bending below the buckling threshold and bending in the extensional quadrant, are consequences of hydrodynamic interactions between the sheets, as it will be demonstrated below. A further example illustrating how the curvature changes with time for $d/L \simeq 0.04$ and $E_v \simeq 12.8$ is given in the Appendix C.

To rationalize the experimental observations, we simulated the dynamics of two parallel flexible sheets. For $E_v = 7$, the simulations indicate that the single sheet dynamics is stable: a small initial curvature decreases in time – see the black line in fig.6.3(c). For a pair of parallel sheets separated by a distance $d = 0.1L$ and the same value $E_v = 7$, the computed curvature follows qualitatively the experimental dynamics, see the red line in fig.6.3(c): each sheet of the pair deforms, adopts a concave shape in the compressional quadrant (fig.6.3(d), left panel), then the curvature changes sign, the sheets adopt a convex shape in the extensional quadrant (fig.6.3(d), right panel) and finally the deformation relaxes to zero. Because in the simulation only hydrodynamic interactions are accounted for, the simulation results support the hydrodynamic origin of the two changes of behavior discussed above in relation to experiments.

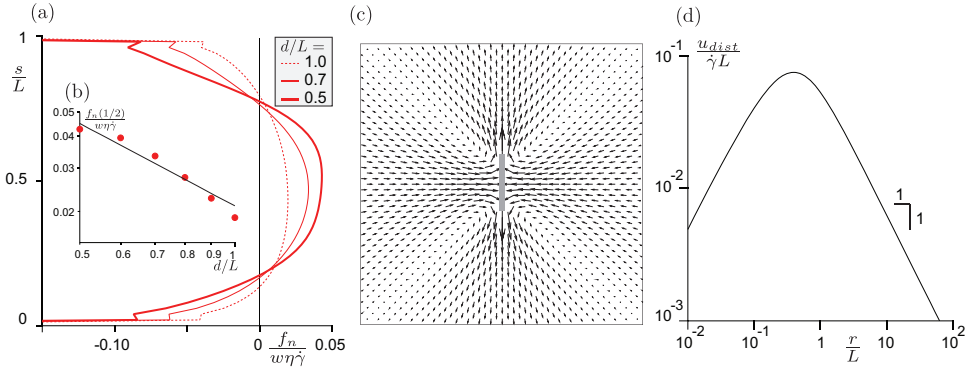


Figure 6.4: Hydrodynamic interactions from simulation. (a) Lateral force induced by the first sheet on the second sheet in the case of two parallel sheets in a shear flow, oriented in the compressional quadrant (at $\theta_0 = -\pi/2 + \pi/10$), for $d/L = 1, 0.7$ and 0.5 . (b) Magnitude of the lateral force at the center of the sheet versus the separation distance when the sheets are oriented in the compressional quadrant (at $\theta_0 = -\pi/2 + \pi/10$). The line is the best fit $y = Ax^\alpha$ with $A \simeq 0.02$ and $\alpha \simeq -1.1$. (c) Vector plot of the 2D disturbance flow. The rectangle represents the sheet. (d) Magnitude of the disturbance flow velocity u_{dist} induced by a sheet in a 2D compressional flow, versus the distance r measured orthogonally to the sheet.

From the numerical simulations of two sheets we computed the lateral force on one of the two sheets, when oriented in the compressional quadrant and for varying distance d/L , see fig.6.4(a). The lateral force is non-uniform along the sheet, with a maximum value in the center of the sheet and minima located at the two edges. The force distribution can be described, to a first approximation, as a parabola. As d/L increases it is seen from fig.6.4(b) that the amplitude of the parabolic profile decreases, following a power law with an exponent close to -1 . To explain and model this lateral force, we quantified the disturbance flow field set up by a sheet. Because the sheet is inertia-less and the flow 2D, the disturbance flow field in the far field is that of a 2D force dipole whose amplitude decreases as $1/r$ [36], where r is the distance from the geometric center of the sheet. The flow disturbance induced by a body oriented along the compressional or extensional axis of a shear flow can be approximated by placing an elongated particle in a two-dimensional purely straining flow [37], with the long axis of the particle along the extensional direction. We performed simulations with this simplified flow configuration. The computed vector plots in fig.6.4(c) illustrate the dipolar characteristics of the flow, where it is seen that the spatial variation of the flow corresponds to the parabolic distribution of the lateral force. The amplitude of the disturbance flow field is reasonably well captured by a $1/r$ dependence for r as small as $0.5L$ (see fig.6.4(d)). The sign of the background straining flow governs the sign

of the dipole: with our convention the sign is positive for compressional background flow and negative for extensional background flow. Hence, the simulations show that the presence of one sheet generates a parabolic lateral force on the other sheet; this lateral force originates from the disturbance dipole flow field, its amplitude scales as L/d and its sign is governed by the background flow field, being positive when the sheets are in the compressional quadrant and negative in the extensional quadrant.

The information above enables to construct a minimalistic model of flow-induced shape changes that takes into account the dependence on sheet-to-sheet distance. From a balance of forces and moments on an inextensible sheet, in the linear approximation the curvature κ obeys the Euler-Bernoulli equation

$$Bw \frac{d^2 \kappa}{ds^2} - T_t(s) \kappa(s) - f_n(s) = 0, \quad (6.4)$$

where s is the curvilinear coordinate, f_n is the lateral hydrodynamic force per unit length and T_t is the axial tension [29, 38]. The axial tension satisfies

$$\frac{dT_t}{ds} + f_t(s) = 0, \quad (6.5)$$

where f_t is the axial hydrodynamic force per unit length [29, 38]. To model f_n and f_t we used a quasi-static approximation that consists of two main assumptions. First, we neglected the effect of the lateral hydrodynamic drag force caused by the time variation of the curvature. Second, we assume that the curvature is only coupled to the orientation θ through the amplitude of f_t , which we assume to be $-2 \sin \theta \cos \theta$. Considering the two extreme cases $\theta = -\pi/4$ (orientation at maximum compression) and $\theta = \pi/4$ (orientation at maximum extension) and modeling the axial force per unit length as an edge force arising from the straining component of the imposed shear rate, we obtain $T_t = -\eta\dot{\gamma}Lw$ for $\theta = -\pi/4$ and $T_t = \eta\dot{\gamma}Lw$ for $\theta = \pi/4$. Fitting the results of our numerical simulations, we modeled the lateral force per unit length arising from the dipolar flow field as

$$f_n(s) = \pm w \frac{L}{d} \eta\dot{\gamma} K g(s) \quad (6.6)$$

where the sign depends on whether the sheet is oriented along the compressional or the extensional axis. The function $g(s) = \frac{1}{12} - \left(\frac{s}{L} - \frac{1}{2}\right)^2$ is a symmetric parabola of zero mean that reproduces the spatial variation of the lateral force seen in fig.6.4(a) and K is a numerical pre-factor. We estimated $K \simeq 0.4$ from the force amplitude computed at the orientation θ_0 , see fig.6.4(b) (by definition $K = A g(1/2)/2 \sin \theta_0 \cos \theta_0$, where A is a fitting parameter). The moment balance then reads

$$\frac{d^2 \tilde{\kappa}}{d\tilde{s}^2} \pm E_v \left(\tilde{\kappa}(\tilde{s}) - \frac{K}{d} g(\tilde{s}) \right) = 0, \quad (6.7)$$

where $\tilde{\kappa} = \kappa L$, $\tilde{s} = s/L$ and $\tilde{d} = d/L$. The "+" sign corresponds to the maximum compression ($\theta = -\pi/4$). The "-" sign corresponds to the maximum extension ($\theta = +\pi/4$). At maximum compression, for the single sheet case ($1/\tilde{d} \rightarrow 0$) this differential equation reduces to the classical Euler-buckling equation for an edge axial load. If $E_v = \pi^2$, the Euler-buckling equation admits two solutions verifying the free end boundary conditions $\tilde{\kappa}(0) = \tilde{\kappa}(1) = 0$. One solution is the trivial solution $\tilde{\kappa}(\tilde{s}) = 0$ and the other is the first buckling mode $\tilde{\kappa}(\tilde{s}) = \tilde{\kappa}_0 \sin(\pi\tilde{s})$ for a purely axial load. The value of the buckling threshold, here π^2 , corresponds to a uniform axial tension. However, it can be shown that for a more realistic model of the axial hydrodynamic force $f_t(s)$, i.e. a linear variation of $f_t(s)$ along the sheet [30] for which the axial tension is a parabola, the threshold is reduced by only 15% with respect to π^2 . Therefore the model of uniform axial tension captures the essential behavior of buckling. The value $E_v^c = 11 \pm 3$ we measured experimentally is comparable with the prediction π^2 of this minimal model. On the other hand, at the maximum compression, for finite \tilde{d} eq. (6.7) admits only one solution satisfying the boundary conditions for any given value of E_v :

$$\begin{aligned} \tilde{\kappa}(\tilde{s}) = & \frac{K}{6\tilde{d}E_v} \left([E_v(-6(\tilde{s}-1)\tilde{s}-1) + 12] + (E_v - 12) \cos\left(\sqrt{E_v}\tilde{s}\right) \right) \\ & + \frac{K}{6\tilde{d}E_v} (E_v - 12) \tan\left(\sqrt{E_v}/2\right) \sin\left(\sqrt{E_v}\tilde{s}\right). \end{aligned} \quad (6.8)$$

The existence of a unique non-zero solution means that there is no buckling instability in the strict sense. Hydrodynamic interactions remove the buckling instability and the curvature has a finite bending amplitude for all values of E_v . To summarize, for a single sheet in pure compression there is a buckling instability while for a pair of sheets, there is no buckling instability but bending deformations do occur. Taking the limits $E_v \rightarrow 0$ and $E_v - E_v^c \rightarrow 0$ with $E_v < E_v^c$, one can derive from eq. (6.8) the following approximation for the maximum curvature (at $\theta = -\pi/4$) of the mid-point of the sheet:

$$\tilde{\kappa} \sim +K \frac{L}{d} \frac{E_v}{E_v^c - E_v}. \quad (6.9)$$

Here we have indicated explicitly the sign of the lateral force, the "+" sign corresponding to the compressional quadrant. In the extensional quadrant, by solving eq. (6.7), one can show that the curvature scales as $\tilde{\kappa} \sim -KE_v L/d$. As illustrated in the sketch on the left panel of fig.6.5, the change of sign of the dipole force as the sheet tumbles explains the change from concave to convex morphologies seen in fig.6.3(b). Equation 6.7 is linear, so the scaling in L/d for the dipole amplitude determines the dependence of the bending curvature with respect to d .

To evaluate the ability of the model above to capture essential features of the experimental data, for each value of the parameters ($E_v, d/L$), we measured the maximum

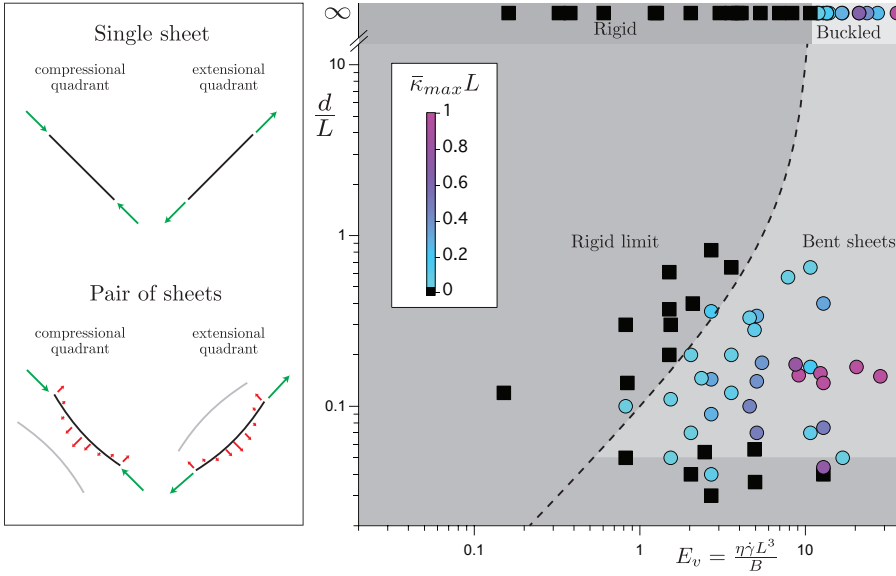


Figure 6.5: Left panel: sketch of the hydrodynamic forces distribution in the single and two sheet cases. The black line segments represent the sheets. The green arrows represent the compressional or extensional tangential forces. The red arrows represent the dipolar lateral forces. For $E_v < E_v^c$ the single sheet remains straight while the pair of sheets adopts concave and convex shapes. Right panel: morphology diagram. Maximum normalized curvature for different normalized separation distances d/L and elasto-viscous numbers $E_v = \eta\dot{\gamma}L^3/B$. The black squares correspond to deformation below the experimental resolution $\kappa_r = 0.02/L$, the color circles to a finite curvature. The shadow regions are guides for the eye. The experimental data for single sheets of fig.6.2(b) are reported in correspondence to $d/L = \infty$. The equation of the dashed line is $d/L = KE_v / (\kappa_r L (E_v^c - E_v))$, with $E_v^c = 11$, $\kappa_r L = 0.02$ and $K = 0.02$. The dashed line is plotted for $d/L > 0.05$.

rescaled curvature $\bar{\kappa}_{max}L$ during tumbling. For pair of sheets, the results indicate two regions of behavior (see right panel fig.6.5). A first region where each sheet's curvature is lower than the experimental resolution. The label "Straight" in the figure indicates this first region. And a second region where the sheets deform significantly (indicated by the label 'Bent' in the figure). Significant deformations are seen to occur for E_v as small as $0.8 - 1$, i.e. approximately ten times smaller than in the single-sheet case. Sheet proximity has thus a strong effect on the morphology. Our simple model provides a criterion for which the curvature becomes larger than the experimental resolution $\kappa_r = 0.02/L$. This criterion defines two regions in the morphology diagram delimited by the dashed line of equation $d/L = KE_v / (\kappa_r L (E_v^c - E_v))$ in fig.6.5. The model predicts a much larger amplitude of deformation than observed in the experiments, but a similar trend with respect to E_v . Indeed, the value of K used in fig.6.5,

$K = 0.02$, is smaller than the one obtained from fitting the lateral force profiles of fig.6.4(b), $K \simeq 0.4$. The overestimation of the amplitude of deformation in the model likely originates from two aspects of the quasi-static approximation we used: first, we neglected the hydrodynamic drag force in the normal direction to the sheets, which delays the curvature response time; second, we assumed that the compressive force f_t is constant while in the experiments the sheets tumbles and thus are not submitted to a constant force. But it can be seen accounting for the difference in the value of K that the model is in reasonably good agreements with experimental data for $d/L \gtrsim 0.05$, as the dashed line in this interval separates the circles from the squares symbols with the correct scaling law in L/d . For $d/L \lesssim 0.05$, the sheets are observed to remain straight during the tumbling motion for all E_v tested and the L/d prediction fails. The experimental data of fig.6.5 reveal thus that the relation between the separation distance and the critical elasto-viscous number to observe significant bending is non monotonic. Further experimental and simulation results of $\bar{\kappa}_{\max}L$ versus d/L for fixed E_v are shown in the Appendix C to give further evidence that the relation is non monotonic. Lubrication forces between two plates separated by a distance d scale as $1/d^3$ for a normal displacement [39] and so are dominant at small distances over the dipolar forces. The time scale for the growth of the deformation in the case of a steady compressive force and lubrication scales as $(L/d)^3\tau$ [39] where $\tau = \eta L^3/B$ is the elasto-viscous time scale. This time scale is much longer than the tumbling time scale $1/\dot{\gamma}$ for moderate $E_v = \dot{\gamma}\tau$ and small d/L . Thus, lubrication forces constrain dynamically the deformation for very small distances and moderate E_v . The convex shape is not observed in every experimental case, because for large distance between the sheets ($d/L > 0.5$) the centers of mass of the sheets are convected by the flow and thus the sheets are not always perfectly “in registry”. A plot showing the amplitude of the maximum curvature of the convex shape from simulations can be found in the Appendix C.

6.6 Conclusion

In this study we measured for the first time the effective buckling threshold, which we define as the threshold to observe significant bending, for a pair of flexible sheets suspended in a viscous simple shear flow as function of the sheet-sheet distance. In experiments, we obtain a value of the critical elasto-viscous number for buckling of a single rectangular sheet of $E_v^c \simeq 11$. This number is quite close to the one we obtain from 2D simulations, $E_v^c \simeq 8$. Our main result is the demonstration of a large reduction, by about a factor of ten, of the elasto-viscous number for which a close pair of parallel sheets bend significantly. This reduction is caused by the dipolar flow disturbance induced by one sheet. This disturbance induces a lateral force on the second sheet.

With a minimal model we showed that this lateral force enhances the effect of the compressional force experienced by the pair when oriented along the compressional axis of the shear flow. Furthermore, we showed that the dipolar flow disturbance induces bending also when the pair is oriented in the extensional quadrant. Experiments and simulations suggest that the amplitude of bending is inversely proportional to the distance between the sheets. For small separations, the lubrication force prevails and limits the dynamical deformation of the sheets. The competition between the dipolar enhancement and lubrication leads to a non-monotonic relation between distance and effective buckling threshold.

In the applied context of designing macroscopic materials, for instance nanocomposites, from sheet-like nanoparticles by liquid-based methods (as ink printing, coating, polymer nano-composite processing and liquid-phase exfoliation [10, 11]), our results suggest that at finite volume fraction hydrodynamic interactions could amplify deformations induced by the shear flow. The effect could alter thermal, optical or electrical properties that are dependent on the nanoparticle shape. In the context of rheology, by focusing on hydrodynamic pair-interactions our results provide a first step to understand the dynamics of flexible sheets in suspension. In particular, it has been evidenced for suspensions of fibers that buckling produces normal stress differences [27]. Hence, our results suggest that the microstructure of a suspension of sheet-like particles, including the statistics of pair-particle orientation and inter-particle distance, could have a profound influence on the rheology by affecting the instantaneous particle shape. Therefore, the microstructure of suspensions of sheet-like particles should be well-characterized in future rheological studies.

REFERENCES

- [1] Beatrice W. Soh, Alexander R. Klotz, Rae M. Robertson-Anderson, and Patrick S. Doyle. “Long-Lived Self-Entanglements in Ring Polymers.” In: *Physical Review Letters* 123 (4 2019), p. 048002.
- [2] Manouk Abkarian, Magalie Faivre, and Annie Viallat. “Swinging of Red Blood Cells under Shear Flow.” In: *Physical Review Letters* 98 (18 2007), p. 188302.
- [3] Kevin S. Sillmore, Michael S. Strano, and James W. Swan. “Buckling, crumpling, and tumbling of semiflexible sheets in simple shear flow.” In: *Soft Matter* 17 (2021), pp. 4707–4718.
- [4] S W Marlow and P D Olmsted. “The effect of shear flow on the Helfrich interaction in lyotropic lamellar systems.” In: *The European Physical Journal E* 8.5 (2002), pp. 485–497.
- [5] Eric Lauga. “Bacterial Hydrodynamics.” In: *Annual Review of Fluid Mechanics* 48.1 (2016), pp. 105–130.
- [6] J. G. Oldroyd and Alan Herries Wilson. “The elastic and viscous properties of emulsions and suspensions.” In: *Proceedings of the Royal Society of London. Series A. Mathematical and Physical Sciences* 218.1132 (1953), pp. 122–132.
- [7] P. G. De Gennes. “Coil-stretch transition of dilute flexible polymers under ultrahigh velocity gradients.” In: *The Journal of Chemical Physics* 60.12 (1974), pp. 5030–5042.
- [8] Vasily Kantsler and Raymond E. Goldstein. “Fluctuations, Dynamics, and the Stretch-Coil Transition of Single Actin Filaments in Extensional Flows.” In: *Physical Review Letters* 108 (3 2012), p. 038103.
- [9] RG Larson. “The rheology of dilute solutions of flexible polymers: Progress and problems.” In: *Journal of Rheology* 49.1 (2005), pp. 1–70.
- [10] Valeria Nicolosi, Manish Chhowalla, Mercouri G. Kanatzidis, Michael S. Strano, and Jonathan N. Coleman. “Liquid Exfoliation of Layered Materials.” In: *Science* 340.6139 (2013).
- [11] Sina Naficy, Rouhollah Jalili, Seyed Hamed Aboutalebi, Robert A. Gorkin III, Konstantin Konstantinov, Peter C. Innis, Geoffrey M. Spinks, Philippe Poulin, and Gordon G. Wallace. “Graphene oxide dispersions: tuning rheology to enable fabrication.” In: *Materials Horizons* 1 (2014), pp. 326–331.

- [12] Keith R Paton et al. “Scalable production of large quantities of defect-free few-layer graphene by shear exfoliation in liquids.” In: *Nature Materials* 13.6 (2014), pp. 624–630.
- [13] Yijiang Yu and Michael D. Graham. “Coil–stretch-like transition of elastic sheets in extensional flows.” In: *Soft Matter* 17 (2021), pp. 543–553.
- [14] Vincent Labalette, Alexis Praga, Florent Girard, Martine Meireles, Yannick Hallez, and Jeffrey F. Morris. “Shear-induced glass-to-crystal transition in anisotropic clay-like suspensions.” In: *Soft Matter* 17 (2021), pp. 3174–3190.
- [15] Yueyi Xu and Micah J. Green. “Brownian dynamics simulations of nanosheet solutions under shear.” In: *The Journal of Chemical Physics* 141.2 (2014), p. 024905.
- [16] Yijiang Yu and Michael D. Graham. “Wrinkling and multiplicity in the dynamics of deformable sheets in uniaxial extensional flow.” In: *Physical Review Fluids* 7 (2022), p. 023601.
- [17] G. Salussolia, C. Kamal, J. Stafford, N. Pugno, and L. Botto. “Simulation of interacting elastic sheets in shear flow: Insights into buckling, sliding, and re-assembly of graphene nanosheets in sheared liquids.” In: *Physics of Fluids* 34.5 (2022), p. 053311.
- [18] Kevin S. Sillmore, Michael S. Strano, and James W. Swan. “Thermally fluctuating, semiflexible sheets in simple shear flow.” In: *Soft Matter* 18 (4 2022), pp. 768–782.
- [19] Ya Wang et al. “Conformational Phase Map of Two-Dimensional Macromolecular Graphene Oxide in Solution.” In: *Matter* 3.1 (2020), pp. 230–245.
- [20] Bloen Metzger and Jason E Butler. “Clouds of particles in a periodic shear flow.” In: *Physics of Fluids* 24.2 (2012).
- [21] David J Smith. “A boundary element regularized Stokeslet method applied to cilia-and flagella-driven flow.” In: *Proceedings of the Royal Society A: Mathematical, Physical and Engineering Sciences* 465.2112 (2009), pp. 3605–3626.
- [22] Sarah D Olson and Lisa J Fauci. “Hydrodynamic interactions of sheets vs filaments: Synchronization, attraction, and alignment.” In: *Physics of Fluids* 27.12 (2015).
- [23] Thomas D Montenegro-Johnson, Lyndon Koens, and Eric Lauga. “Microscale flow dynamics of ribbons and sheets.” In: *Soft Matter* 13.3 (2017), pp. 546–553.
- [24] Constantine Pozrikidis. *Boundary integral and singularity methods for linearized viscous flow*. Cambridge university press, 1992.

- [25] Ricardo Cortez. “The method of regularized Stokeslets.” In: *SIAM Journal on Scientific Computing* 23.4 (2001), pp. 1204–1225.
- [26] Lisa J Fauci and Charles S Peskin. “A computational model of aquatic animal locomotion.” In: *Journal of Computational Physics* 77.1 (1988), pp. 85–108.
- [27] Leif E. Becker and Michael J. Shelley. “Instability of Elastic Filaments in Shear Flow Yields First-Normal-Stress Differences.” In: *Physical Review Letters* 87 (2001), p. 198301.
- [28] José Bico, Étienne Reyssat, and Benoît Roman. “Elastocapillarity: When Surface Tension Deforms Elastic Solids.” In: *Annual Review of Fluid Mechanics* 50.1 (2018), pp. 629–659.
- [29] Basile Audoly and Yves Pomeau. *Elasticity and Geometry*. Oxford University Press, 2000.
- [30] Olivia du Roure, Anke Lindner, Ehssan N. Nazockdast, and Michael J. Shelley. “Dynamics of Flexible Fibers in Viscous Flows and Fluids.” In: *Annual Review of Fluid Mechanics* 51.1 (2019), pp. 539–572.
- [31] George Barker Jeffery. “The motion of ellipsoidal particles immersed in a viscous fluid.” In: *Proceedings of the Royal Society of London. Series A, Containing papers of a mathematical and physical character* 102.715 (1922), pp. 161–179.
- [32] Catherine Kamal, Simon Gravelle, and Lorenzo Botto. “Effect of hydrodynamic slip on the rotational dynamics of a thin Brownian platelet in shear flow.” In: *Journal of Fluid Mechanics* 919 (2021), A1.
- [33] P.S Lingard and R.L Whitmore. “The deformation of disc-shaped particles by a shearing fluid with application to the red blood cell.” In: *Journal of Colloid and Interface Science* 49.1 (1974), pp. 119–127.
- [34] Samuel Poincloux, Tian Chen, Basile Audoly, and Pedro M. Reis. “Bending Response of a Book with Internal Friction.” In: *Physical Review Letters* 126 (2021), p. 218004.
- [35] Guorui Wang, Zhaohe Dai, Junkai Xiao, ShiZhe Feng, Chuanxin Weng, Luqi Liu, Zhiping Xu, Rui Huang, and Zhong Zhang. “Bending of Multilayer van der Waals Materials.” In: *Physical Review Letters* 123 (2019), p. 116101.
- [36] Élisabeth Guazzelli and Jeff Morris. *A Physical Introduction to Suspension Dynamics*. Cambridge University Press, 2012.
- [37] G K Batchelor. “The stress generated in a non-dilute suspension of elongated particles by pure straining motion.” In: *Journal of Fluid Mechanics* 46.4 (1971), pp. 813–829.

- [38] Jason S. Wexler, Philippe H. Trinh, Helene Berthet, Nawal Quennouz, Olivia du Roure, Herbert E. Huppert, Anke Lindner, and Howard A. Stone. “Bending of elastic fibres in viscous flows: the influence of confinement.” In: *Journal of Fluid Mechanics* 720 (2013), pp. 517–544.
- [39] N. Sridhar, D.J. Srolovitz, and B.N. Cox. “Buckling and post-buckling kinetics of compressed thin films on viscous substrates.” In: *Acta Materialia* 50.10 (2002), pp. 2547–2557.

7

CONCLUSIONS AND RECOMMENDATIONS

In this chapter, the main conclusions of this thesis corresponding to the research questions proposed in the first chapter are given. Moreover, some recommendations of the future research directions are listed.

7.1 Conclusions

This thesis addresses two fluid dynamics problems: (i) sedimentation of polydisperse suspensions, and (ii) buckling of flexible particles in the shear flow. These topics are motivated by the need to better understand the processing of 2D nanomaterials in liquids. The flow regime considered in this thesis is the Stokes flow, as the local particle Reynolds number in liquid processing of 2D materials is particularly small. In Stokes flow, the hydrodynamic interaction between particles is long-ranged, and the main focus of this thesis is to study the effect of long range hydrodynamic interactions on the particle dynamics (e.g. settling velocity, buckling threshold). The work is based on numerical simulations, complemented by the theoretical analysis of experiments carried out by collaborators. In this section, answers to the research questions proposed in chapter 1 are provided.

Sedimentation of polydisperse suspensions

The first objective of the PhD research was to understand the sedimentation of polydisperse suspensions, in view of applications to particle size fractionation. This objective is addressed in chapters 3, 4 and 5.

In chapter 3, a one-dimensional model is used to study the multicascade centrifugation of polydisperse suspensions to isolate certain size ranges from an initial size distribution. The model predicts the time evolution of the volume fraction distribution of each size class. Assuming the suspension to be very dilute, the settling velocity of each size class is calculated by using the corresponding Stokes velocity, neglecting particle-particle interactions. Two scenarios are considered: band sedimentation, where initially particles are dispersed in a small slab on top of the clear fluid, and homogeneous sedimentation, where initially particles are evenly dispersed in the vial. The question we want to answer is:

- What are the optimal parameters to obtain a relatively monodisperse suspension starting from a polydisperse suspension through a liquid cascade centrifugation process?

It is demonstrated that band sedimentation is preferred to homogeneous sedimentation for the purpose of size fractionating a particulate suspension, as there is a clear distinction between the size classes in the supernatant and those in the sediment layer at each time in band sedimentation. The drawbacks of band sedimentation are the limited amount of materials being processed in each step of the multicascade centrifugation and the potential occurrence of Rayleigh-Taylor instabilities happening at the interface between the particle-laden layer and the clear fluid, which could lead to mixing of particles of different sizes [1]. With regard to the number of centrifugation

steps, it is found that surprisingly a two-step multicascade centrifugation procedure gives the least amount of impurity (i.e. particles that are selected but are not in the desired particle size range) than other procedures involving more steps. To reduce the amount of impurity even further, an improved two-step procedure is proposed by reducing the centrifugation time in the second step by a small amount. However, this also leads to a decrease of the yield. Thus, the multicascade centrifugation process can be optimized based on a trade-off between the yield and the amount of impurity desired. Despite the limitations of neglecting hydrodynamic interactions, this is the first analysis of multicascade centrifugation presented in the literature.

For suspensions where particle-particle interactions are not negligible, the average and fluctuating particle settling velocity depend on the distribution of particle sizes. The effect of hydrodynamic interactions on the particle settling velocities of polydisperse suspensions of spheres is studied in chapter 4. In this chapter, settling velocity statistics for dilute, non-Brownian homogeneous suspensions of polydisperse spheres having a log-normal size distribution are generated from Stokesian dynamics simulations and investigated, as a function of the total volume fraction ϕ and normalized with α of the particle size distribution. Both the average velocities and the velocity fluctuations of each size class are analyzed. The question we want to answer is:

- How to predict the average settling velocity of each size class in a dilute settling polydisperse suspension?

The average settling velocity $\langle u_{z,i} \rangle$ of each size class decreases for increasing α . Moreover, $\langle u_{z,i} \rangle$ decays faster for the smaller particles than for the largest particles, with increasing ϕ or increasing α , indicating a larger effect of hydrodynamic interactions on the lower tail of the size distribution. A thorough comparison between our numerical results and predictions of existing models of the hindered settling function of each size class is made in chapter 4. The Batchelor's model which is proposed based on the first principle gives quite accurate predictions for all size classes when $\phi \leq 0.05$, and it underpredicts the hindered settling function of every size class at larger volume fractions. The Davis & Gecol model and the MLB model give comparable predictions, with both overestimating the hindered settling functions of the smaller particles. As for the Richardson-Zaki model, which is parameterized only on the total volume fraction, gives the worst predictions, especially for the smaller particles. As an extension of the Richardson-Zaki model, the MLB model performs better because it uses the Richardson-Zaki model to estimate the slip velocity between each particle class and the fluid, rather than the settling velocity directly. Considering the model derivations and applications, it would be valuable to improve the MLB model. The main assumption of the MLB model is that the Stokes drag correction for each size class depends on the total volume fraction. This assumption cannot hold in gen-

eral, and thus this is the main area of model improvement. Our results suggest that when using these hindered settling models to predict the volume fraction distribution of each size class in a settling polydisperse suspension [2, 3], there will be large errors in the predictions of the smaller size classes. For example, the composition of smaller particles in the sediment will be overestimated.

For the velocity fluctuations of each size class, they increase as ϕ or α increases, and appear to follow the approximate scaling $u'_i \sim u_{St,i} (\alpha_i / \langle \alpha \rangle)^{-2}$. The anisotropy ratio between the vertical and horizontal velocity fluctuations is around 3.5 in our simulations. Our results of the velocity fluctuation scaling have implications on the modeling of hydrodynamic diffusivity in polydisperse systems. The hydrodynamic self-diffusivity of monodisperse suspensions is often modeled as $D \sim \alpha \langle u \rangle$, where α is the particle size and $\langle u \rangle$ is the average velocity of the particles [4]. This expression can be understood as the product of a correlation length proportional to α and a fluctuating particle velocity proportional to the mean particle velocity. Our results suggest that this formulation may not be generalized to polydisperse systems to write the hydrodynamic diffusivity of class i as $D_i \sim \alpha_i \langle u_i \rangle$. Indeed, we have shown that the mean velocity $\langle u_i \rangle$ depends on the particle size α_i whereas the velocity fluctuations do not seem to depend on the size of the particle. Instead, the diffusivity of class i might be written as $D_i \sim \alpha_i \langle u \rangle$ where $\langle u \rangle$ is the average velocity of the suspension, and this needs more further research.

During this thesis, a Stokesian dynamics method has been developed. This code has also been used to reply to a practical problem of interest to experimental collaborators who try to calculate the density of the flocs based on the Stokes velocity formula and the measured settling velocity [5]:

- What are the implications of the widely used experimental procedure based on pipetting a suspension drop in a vertical tank to measure the single particle Stokes velocity?

In chapter 5, the implications of this procedure on the experimental measurement of particle density are analyzed by considering two types of particle settling: individual settling where a single particle is allowed to settle, and collective settling where a collection of particles are injected into the column. Simulations are carried out using the Stokesian dynamics code and experiments are carried out by the collaborators in Deltares. In the individual settling case, the particle settling velocity agrees with the Stokes velocity, whereas in the collective settling case the individual particle settling velocity is around $O(10)$ times the Stokes velocity even at very small volume fractions. Moreover, the particle settling velocity is further enhanced when part of the particles are replaced with particles of larger sizes. There is no strong correlation between the particle settling velocity and size in the collective settling of a group of polydisperse

particles, as different sized particles have similar settling velocity ranges. The increase of settling rate is due to the hydrodynamic interactions between particles. Additional dynamic simulations show that for a widely polydisperse cloud at very low volume fractions, particles in the tail have very weak hydrodynamic interactions with particles in the core of the cloud, thus tail particles have settling rates much closer to the Stokes velocities. Our study suggests that by recording the settling dynamics both at the individual particle level and at the suspension cloud level in the experiments, it is possible to correct the measured settling velocities to the Stokes velocities by using the cloud velocity formula. Moreover, by measuring the distance between each particle and the center of mass of the cloud in the experiments, it is possible to identify the tail particles whose settling velocities are rather close to their Stokes velocities in the settling of a polydisperse cloud.

Buckling of flexible particles in the shear flow

The second objective is to investigate the deformation dynamics of flexible particles in a simple shear flow.

In chapter 6, the effect of viscous hydrodynamic interactions on the morphology of flexible sheets in a simple shear flow is investigated both experimentally and numerically. The research questions are:

- What is the threshold above which a flexible sheet will deform in the shear flow?
- How does this threshold change due to hydrodynamic interactions in the shear flow?

From experiments of thin sheets suspended in a shear cell, the critical value of the elasto-viscous number for the buckling of a single rectangular sheet is found to be around 11. This value is close to the one obtained from boundary integral simulations, which is around 8. For a close pair of parallel sheets, a large reduction by about a factor of ten of the elasto-viscous number for which they bend significantly is found. This reduction is caused by a lateral hydrodynamic force from the disturbance flow induced by the neighboring sheet. At the leading order, this disturbance flow can be described by the flow of a force dipole. This dipolar flow also induces bending when the pair is oriented in the extensional quadrant. The amplitude of bending of the pair is inversely proportional to the inter-sheet distance. For small separations, the lubrication between them prevails and limits the bending. The competition between the dipolar enhancement and lubrication leads to a non-monotonic relation between the distance and effective buckling threshold. Our study suggests that the deformation of close sheets in a suspension may not only depend on the mechanical and geometric properties of each sheet but also on the pair-particle distance (and thus on the concentration).

7.2 Recommendations

A few directions are recommended for future research:

- In chapter 3, the hydrodynamic interactions are neglected in the mathematical model. To consider them, the hindered settling functions analyzed in chapter 4 can be used as closures for the settling velocity of each size class. Then the model can be extended to study non-dilute suspensions and investigate the effect of hydrodynamic interactions on the evolution of volume fraction distributions.
- For the hindered settling of polydisperse suspensions, systems of larger volume fractions should be analyzed. The largest volume fraction considered in chapter 4 is 0.1. It is shown in chapter 4 by dynamic simulations that clustering is not obvious in dilute suspensions. However, particles may cluster together in dense suspensions. Thus, dynamic simulations in which the particle positions are updated in time should be carried out for dense suspensions. Moreover, stresslet and lubrication should also be included in the code when simulating larger volume fractions.
- As pointed out in chapter 4, a promising way to improve the MLB model is to adopt more accurate drag closures in the MLB model. However, published drag models for polydisperse systems have been proposed in the literature based on the data of flow past fixed random arrays. Could these closures be adapted to sedimenting polydisperse suspensions? Simulations of polydisperse systems where particles move freely should be carried out to build polydisperse drag models which consider particle relative motions.
- In this thesis, only spherical particles are considered for sedimentation. It would be interesting to study the settling of plate-like particles for applications to nanosheets, clay particles, etc. Numerical simulations of settling of plate-like particles are possible by representing each plate through connected spheres as done in the multiblob approach [6]. Relevant references for the possible numerical approaches are refs [7–9]. Fast settling streamers are found in fiber suspensions [4], and it would be interesting to see if they exist in platelet suspensions.
- Experiments of sedimentation of polydisperse suspensions with broad size distributions should be carried out, as currently there is no such study in the literature. The velocity of each size class in the homogeneous region where all size classes are present should be measured. The mean settling velocity of each size class should be compared with model predictions. The velocity fluctuations of different size classes can be compared with each other to see if they have similar magnitudes as observed in our simulations in chapter 4.

REFERENCES

- [1] Shusaku Harada, Takashi Mitsui, and Kodai Sato. “Particle-like and fluid-like settling of a stratified suspension.” In: *The European Physical Journal E* 35 (2012), pp. 1–6.
- [2] S. Berres, R. Bürger, and E. M. Tory. “Applications of polydisperse sedimentation models.” In: *Chemical Engineering Journal* 111.2-3 (2005), pp. 105–117.
- [3] Robert Dorrell and Andrew J Hogg. “Sedimentation of bidisperse suspensions.” In: *International Journal of Multiphase Flow* 36.6 (2010), pp. 481–490.
- [4] Elisabeth Guazzelli and John Hinch. “Fluctuations and instability in sedimentation.” In: *Annual Review of Fluid Mechanics* 43 (2011), pp. 97–116.
- [5] W Ali, Alex Kirichek, and C Chassagne. “Collective effects on the settling of clay flocs.” In: *Applied Clay Science* 254 (2024), p. 107399.
- [6] Florencio Balboa Usabiaga, Bakytzhan Kallemov, Blaise Delmotte, Amneet Bhalla, Boyce Griffith, and Aleksandar Donev. “Hydrodynamics of suspensions of passive and active rigid particles: a rigid multiblob approach.” In: *Communications in Applied Mathematics and Computational Science* 11.2 (2017), pp. 217–296.
- [7] James W Swan and Gang Wang. “Rapid calculation of hydrodynamic and transport properties in concentrated solutions of colloidal particles and macromolecules.” In: *Physics of Fluids* 28.1 (2016).
- [8] Vincent Labalette, Alexis Praga, Florent Girard, Martine Meireles, Yannick Hallez, and Jeffrey F Morris. “Shear-induced glass-to-crystal transition in anisotropic clay-like suspensions.” In: *Soft Matter* 17.11 (2021), pp. 3174–3190.
- [9] Hang Su and Eric E Keaveny. “Accelerating the force-coupling method for hydrodynamic interactions in periodic domains.” In: *Journal of Computational Physics* 510 (2024), p. 113060.

PART II APPENDICES

A

APPENDIX TO CHAPTER 3

A.1 Derivation of Eq.3.8

Since Eq.3.2 is linear, it can be solved analytically, and the solution under initial condition Eq.6.2 is:

$$N(x, t, q) = N_0(x - qt, q).$$

Based on this analytical solution, the number of particles with settling velocity q in the supernatant at time t is:

$$\begin{aligned} n_q^s(t) &= \int_0^H N(x, t; q) dx = \int_0^H f_0(q) n_0(x - qt) dx \\ &= f_0(q) \int_{-qt}^{H-qt} n_0(x - qt) d(x - qt) = f_0(q) \int_{-qt}^{H-qt} n_0(u) du. \end{aligned}$$

For band sedimentation, based on the expression for initial total particle number density $n_0(x)$, we have:

$$n_q^s(t) = \begin{cases} f_0(q) \times 1 \times h = hf_0(q) & H - qt \geq h \\ f_0(q) \times 1 \times (H - qt) = (H - qt)f_0(q) & 0 < H - qt < h \\ 0 & H - qt \leq 0 \end{cases}$$

Here h is the thickness of the initial particle-laden layer, H is the filling height of the dispersion, and the value of n_0 is chosen as 1.

For homogeneous sedimentation, we have:

$$n_q^s(t) = \begin{cases} (H - qt)f_0(q) & H - qt > 0 \\ 0 & H - qt \leq 0 \end{cases}.$$

Based on the expression for $n_q^s(t)$, we know that at time t the number of particles of q larger than H/t is 0 in the supernatant. Since the largest value of q in the sample is Q , the largest value of q in the supernatant at time t is:

$$q_{\max}^s = \begin{cases} H/t & t > H/Q \\ Q & t \leq H/Q \end{cases}.$$

A.2 Derivation of Eq.3.10

Consider a thin disk with lateral size d and thickness L settling in a viscous liquid under an external force field with equivalent g -force g_e . The body force on this disk is:

$$F_b = (\rho_p - \rho_l) \frac{\pi}{4} d^2 L g_e.$$

Here, ρ_p and ρ_l are densities of the particle and liquid, respectively. The drag force on the disk can be expressed as:

$$F_d = f \cdot 3\pi\mu_l d_e q,$$

where μ_l is the dynamic viscosity of the liquid, d_e is the equivalent-volume diameter of the particle which equals $(3Ld^2/2)^{1/3}$ for a disk particle, q is the settling velocity, and f is the correction factor due to the non-spherical shape [1]. For a thin disk with aspect ratio $E = L/d$, the correction factor f is $\frac{8E^{-1/3}}{3\pi}$ when the disk settles in the direction parallel to its axis of symmetry (broadwise), and is $\frac{16E^{-1/3}}{9\pi}$ when the disk settles in the direction perpendicular to its axis (edgewise) [1]. To account for the rotational Brownian motion, the correction factor is averaged over all orientations, which is $\frac{2E^{-1/3}}{\pi}$. This gives the drag force as:

$$F_d = 6.87\mu_l q d.$$

By equating the body force and drag force on the disk, the settling velocity of a thin disk particle is

$$q = \frac{\pi}{27.48\mu_l} (\rho_p - \rho_l) g_e d L.$$

B

APPENDIX TO CHAPTER 4

B.1 Derivation of the slip velocity closure in the MLB model

A derivation of the MLB model is provided here to highlight the key assumptions of the model, which was too concisely described in the original papers [2, 3]. Consider a homogeneous polydisperse suspension with m particulate classes. The radius and density of the j -th class are a_j and ρ_j , respectively, with $j = 1, 2, \dots, m$. The density and dynamic viscosity of the fluid are ρ_f and μ , respectively. Gravity is in the negative z direction. Due to the differences between the particle and the fluid densities, a macroscopic pressure gradient dp/dz along the height of the mixture is needed to balance the excess weight of the particles. This pressure gradient drives the back flow of the fluid during settling of the particles. Corresponding to this pressure gradient, each particle experiences a buoyancy force $F_{\nabla p} = (-dp/dz)V_p$, where V_p is the volume of that particle. The total force exerted on each particle by the fluid is given by $F_{\nabla p}$, by the buoyancy force due to the undisturbed hydrostatic pressure gradient and by the drag force due to the relative fluid-particle velocity difference.

The steady-state momentum equation for the fluid phase is

$$\left(-\frac{dp}{dz}\right)(1 - \phi) - \sum_{j=1}^m f_{d,j} = 0, \quad (\text{A.S1})$$

where ϕ is the total volume fraction, and $f_{d,j}$ is the volumetric drag force density (drag per unit volume) exerted by the j -th particle class. The steady-state particle momentum equation for the j -th particle class is

$$\left(-\frac{dp}{dz}\right)\phi_j + f_{d,j} - (\rho_j - \rho_f)\phi_j g = 0, \quad (\text{A.S2})$$

where ϕ_j is the volume fraction of the j -th class. Using equations (A.S1) and (A.S2) gives

$$\frac{dp}{dz} = -\sum_{j=1}^m (\rho_j - \rho_f)\phi_j g, \quad (\text{A.S3})$$

and

$$f_{d,j} = (\rho_j - \rho_{susp})\phi_j g, \quad (\text{A.S4})$$

where $\rho_{susp} = (1 - \phi)\rho_f + \sum_{i=1}^m \rho_i \phi_i$ is the density of the suspension (see e.g. Xia et al. [4] for the case $m = 1$). The predictive accuracy of equation (A.S4) for small particles immersed in a suspension of larger particles has been put into question [5, 6].

To calculate the particle velocity, a constitutive equation relating relative velocity to force must be postulated. The MLB model uses a linear law between the drag force and the slip velocity $u_{slip,j}$ between the j -th particle class and the average fluid velocity:

$$f_{d,j} = -\beta_j u_{slip,j}. \quad (\text{A.S5})$$

where $u_{slip,j}$ is defined as in equation (4.14). The friction coefficient was calculated as $\beta_j = \frac{9\mu\phi_j C(\phi)}{2a_j^2}$. The case $C = 1$ corresponds to no influence of neighbouring particles on the drag force exerted on a test particle (the factor ϕ_j is due to the fact that $f_{d,j}$ is a force per unit volume). To model hydrodynamic interactions on the drag force, the MLB model assumes $C(\phi) = (1 - \phi)^{2-n}$, as for a monodisperse case at the same total volume fraction (from Richardson-Zaki's correlation, the slip velocity in the monodisperse case is $u_{slip} = \langle u_p \rangle - \langle u_f \rangle = \frac{\langle u_p \rangle}{1-\phi} = u_{st}(1 - \phi)^{n-1}$; equating (A.S4) and (A.S5) using this slip velocity gives $C(\phi) = (1 - \phi)^{2-n}$).

From (A.S4) and (A.S5), the slip velocity for the polydispersed case is

$$u_{slip,j} = \frac{2a_j^2}{9\mu} (1 - \phi)^{n-2} (\rho_j - \rho_{susp}). \quad (\text{A.S6})$$

If all the particles have the same density, $\rho_{susp} = (1 - \phi)\rho_f + \phi\rho_p$ and $\rho_j - \rho_{susp} = (1 - \phi)(\rho_p - \rho_f)$. In this case the slip velocity simplifies to

$$u_{slip,j} = u_{st,j}(1 - \phi)^{n-1}, \quad (\text{A.S7})$$

where $u_{st,j}$ is the Stokes velocity of the j -th species. Using the definition of the slip velocity and using mass continuity $\sum_j \phi_j \langle u_j \rangle + (1 - \phi)\langle u_f \rangle = 0$ yields equation (4.3).

It can be seen from the derivation that the main assumptions in MLB's model are embedded in equations (A.S4) and (A.S5).

APPENDIX TO CHAPTER 6

c.1 PIV measurement of the shear flow

The PIV was performed in the plane orthogonal to the vorticity direction with millimeters size air bubbles as tracers. Results are shown in Fig.C.S1. Fig.C.S1(a) is a vector plot of the mean velocity field averaged over 13 seconds. It can be seen the mean flow is a simple shear flow. To show the magnitude of the velocity fluctuation, time variation of the velocity at a fixed position inside the shear cell is shown in Fig.C.S1(b). It is seen that the horizontal velocity (in the shear direction) is quite steady and the vertical velocity (in the gradient direction) is around 0 over time.

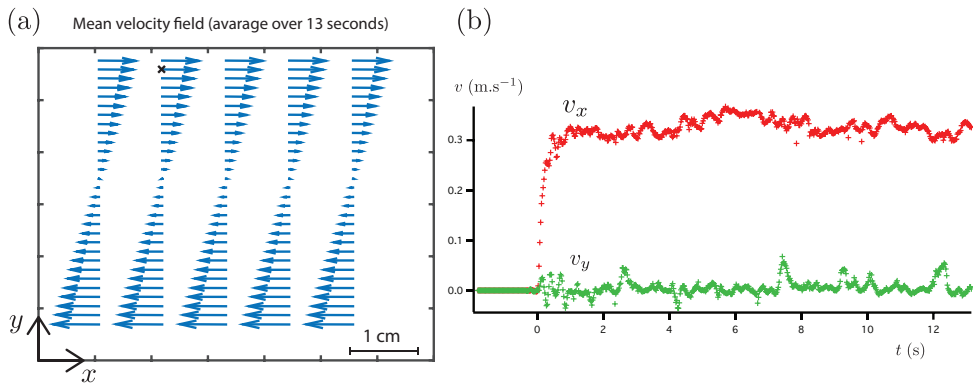


Figure C.S1: (a) Mean PIV field in the plane orthogonal to the vorticity direction. The length of the arrow indicates the magnitude. The average velocity in the flow direction at the position of the black cross is 0.33 m.s^{-1} . (b) Time series of the amplitude of the velocity in the flow direction v_x and in the flow gradient v_y direction at a fixed position (see the black cross on Fig.C.S1(a)). The motor is switched on at time zero on the graph.

c.2 Angle versus time for two parallel sheets

Fig.C.S2 shows the angle versus time from experiment corresponding to fig.6.3(a) for $E_v \simeq 3.6$ and $d/L \simeq 0.2$. The monotonic time evolution of the angle was used to shift correctly the time by a linear interpolation for the period where few frames are missing (at $\dot{\gamma} \simeq 0.17$ and 5.4).

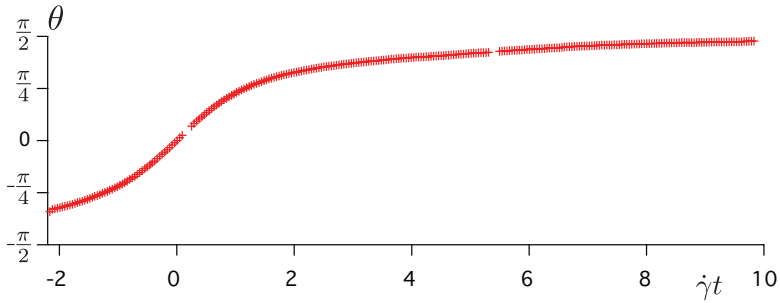


Figure C.S2: Angle versus time corresponding to to fig.6.3(a) of chapter 6.

c.3 Curvature versus time

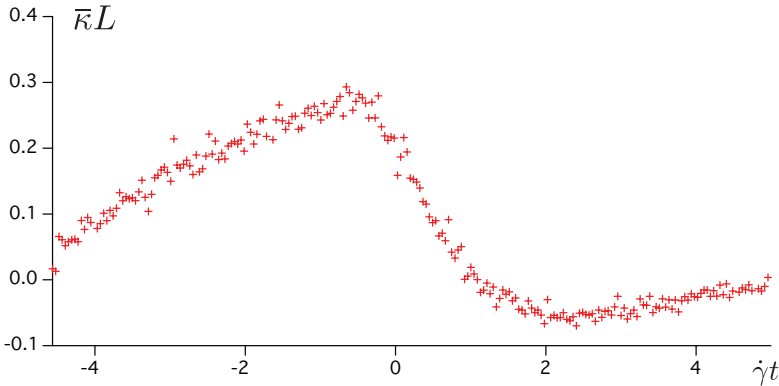


Figure C.S3: Normalized curvature $\bar{\kappa}L$ versus normalized time $\dot{\gamma}t$ for a sheet pair separated by $d/L \simeq 0.09$ for $E_v \simeq 7.5$ in the experiment.

Here we show another example of how the curvature of the sheets changes with time for the two sheets separated by $d/L \simeq 0.09$ and $E_v \simeq 7.5$ in the experiment. Same signature with that seen in Fig.6.3(a) in chapter 6 is observed here also. The

curvature of the two sheets first increases with time, then decreases, changes sign and finally decays to zero. Whereas for a single sheet in the shear flow with $E_v \simeq 7.5$, its deformation is negligible as shown in Fig.6.2(b) in chapter 6.

c.4 Measurement of the curvature and orientation

Here we explain how the curvature and orientation of the sheet is measured in the experiments. From the image of the sheets in the shear flow obtained in the experiments, as shown in Fig.C.S4, the profile of one sheet is manually detected with imageJ ($X(n), Y(n)$) (red crosses in Fig.C.S4(Left)). The average orientation is extracted with linear fit of Y versus X . The curvature is extracted with parabolic fit of $X(n)$ and $Y(n)$ (red lines in Fig.C.S4(Right)). From these parabolic fits, the mid-point curvature is

$$\kappa = \frac{X'Y'' - Y'X''}{(X'^2 + Y'^2)^{3/2}}. \quad (\text{C.S1})$$

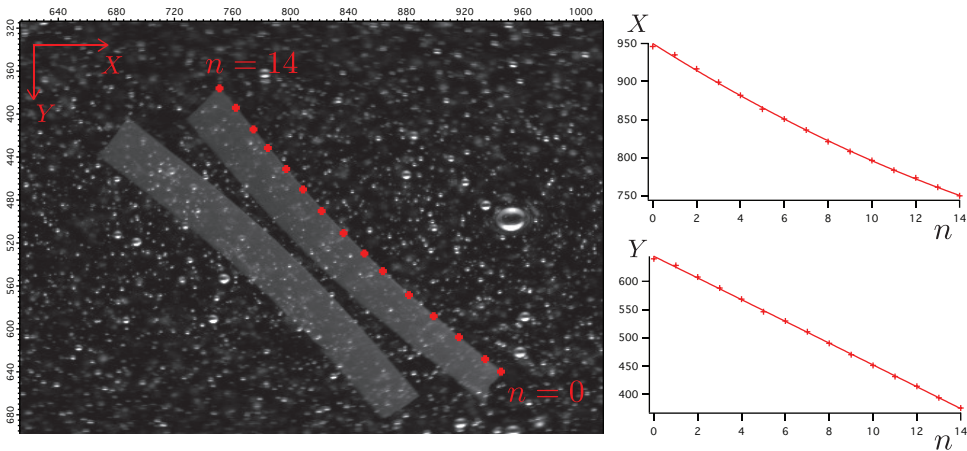


Figure C.S4: Left: Snapshot of two sheets in the compressional quadrant. The red crosses are manually detected for the profile of the sheet. Right: Parabolic fit of the sheet profile.

c.5 Fig.6.2(b) in lin-lin scale and log-log scale

Here we reproduce the Fig.6.2(b) in chapter 6 in linear-linear scale, as shown in Fig.C.S5. From the data we defined the threshold elasto-viscous number to be 11 ± 3 .

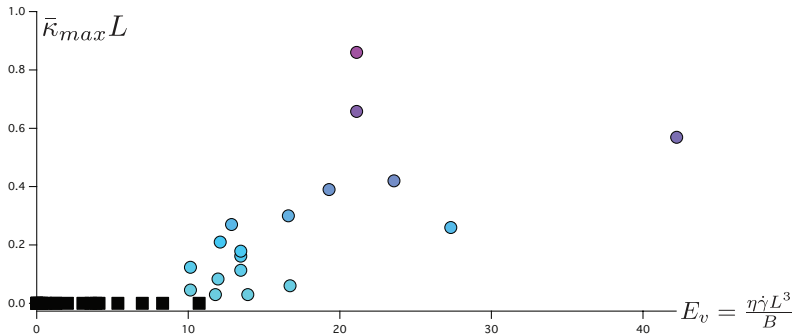


Figure C.S5: Maximum normalized curvature versus elasto-viscous number for a single sheet in linear-linear scale.

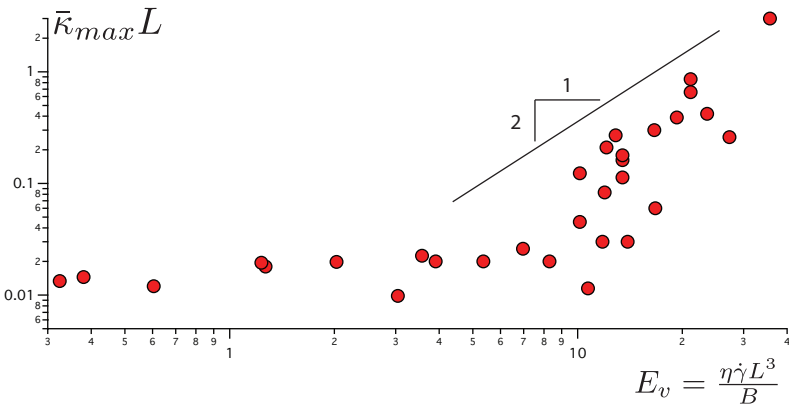


Figure C.S6: Maximum curvature versus the elasto-viscous number in Log-Log scale for a single sheet.

c.6 Maximum curvature versus elastoviscous number for a single sheet from simulations

See Fig.C.S7.

c.7 Non-monotonic relation between curvature and separation distance

We plotted the maximum normalized curvature ($\bar{\kappa}_{max}L$) as a function of normalized separation distance (d/L) for different elasto-viscous numbers (E_v) from simulations in Fig.C.S8 and from experiments in Fig.C.S9. From Fig.C.S8, it is seen that the maximum curvature first increases and then decreases at each fixed E_v as d/L in-

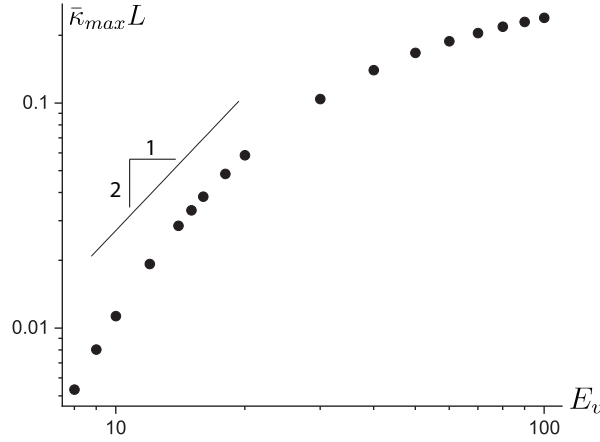


Figure C.S7: Maximum curvature v.s. E_v for a single sheet from simulations.

creases from 0.1 to 1 in the simulations. From Fig.C.S9, it is seen that the maximum curvature is clearly larger when d/L is about 0.1 to 0.3 than the maximum curvature for both smaller d/L ($d/L < 0.1$) and larger d/L ($d/L > 0.3$) in the experiments. Thus, the relation between the curvature of the bent sheets and the separation distance is non-monotonic. Moreover, shapes of the pair of sheets when they have maximum curvatures during tumbling for different initial separation distances at $E_v = 20$ from simulations are shown in Fig.C.S10. It is seen that the sheets have similar 'C' shapes at different d/L values, and they are more curved when $d/L = 0.4$ comparing to $d/L = 0.1$ and $d/L = 0.7$.

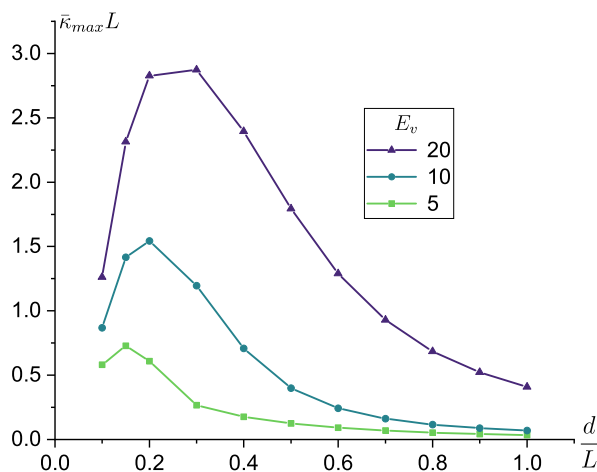


Figure C.S8: Maximum normalized curvature for different normalized separation distances d/L and elasto-viscous numbers E_v from simulations.

c.8 Curvatures of convex shapes

The convex shape is not observed in every experimental case, because for large distance between the sheets ($d/L > 0.5$) the centers of mass of the sheets are convected by the flow and thus the sheets are not perfectly “in registry”. Thus, we have convex shape data only for a limited number of cases. We have studied the convex curvature numerically, and found that our model predicts the sign of the curvature, but not the scaling with respect to E_v and d . Below (Fig.C.S11) we provide data from simulations of the amplitude of the maximum curvature of the convex shape. From this plot, it is seen that the amplitude of the maximum curvature of the convex shape first increases then decreases as E_v increases for fixed d/L .

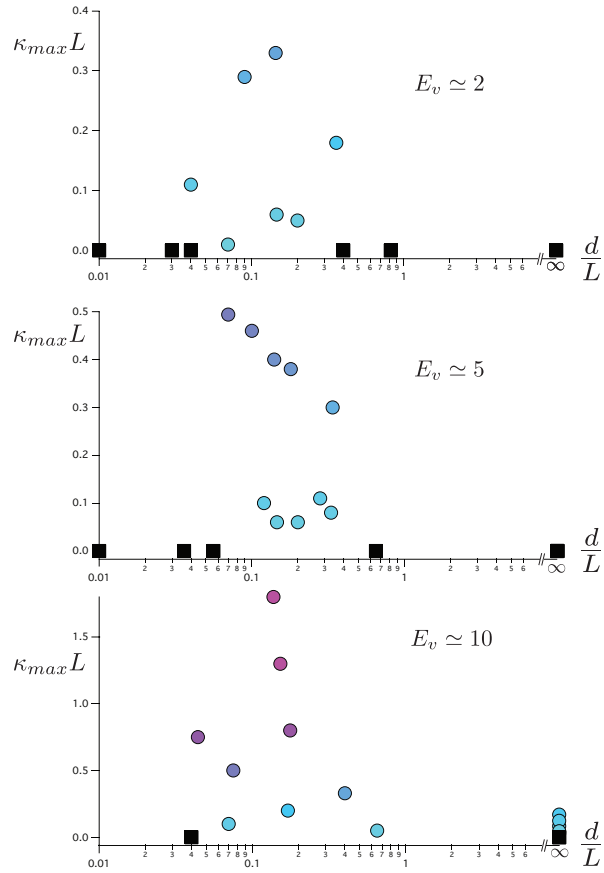


Figure C.S9: Maximum normalized curvature for different normalized separation distances d/L at $E_v \simeq 2, 5$ and 10 from experiments.

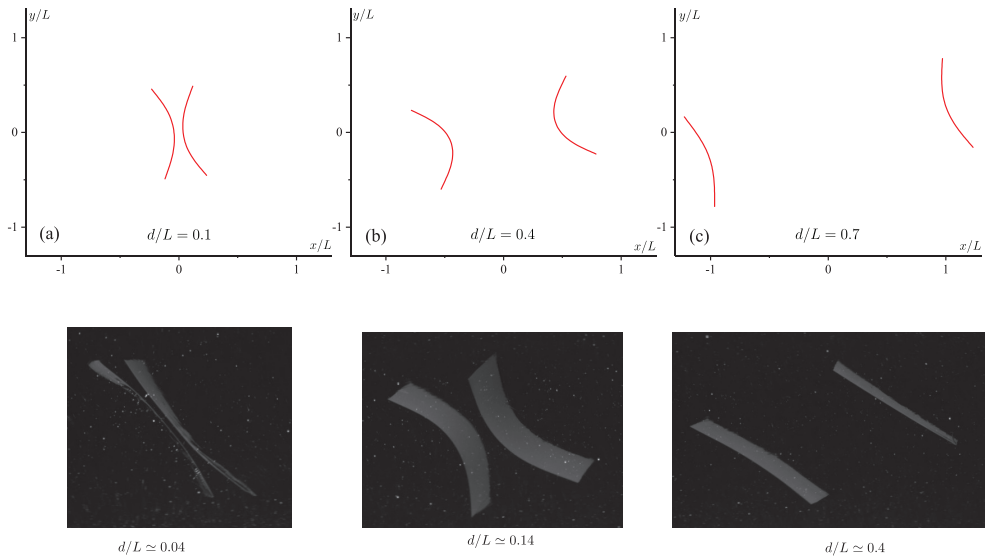


Figure C.S10: Shapes of the pair of sheets when they have maximum curvatures during tumbling for different initial separation distances at $E_v = 20$ from simulations. $d/L = 0.1$ (a), 0.4 (b) and 0.7 (c). Bottom row. Snapshot from experiments at $E_v \approx 12.8$ of pairs of sheets at maximum curvature for different distance $d/L = 0.04, 0.14$ and 0.4 .

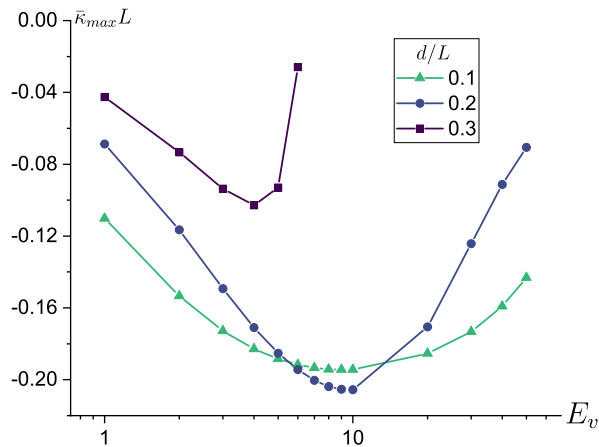


Figure C.S11: Maximum normalized curvature of the convex shape for different normalized separation distances d/L and elasto-viscous numbers E_v from simulations.

REFERENCES

- [1] E Loth. “Drag of non-spherical solid particles of regular and irregular shape.” In: *Powder Technology* 182.3 (2008), pp. 342–353.
- [2] J. H. Masliyah. “Hindered settling in a multi-species particle system.” In: *Chemical Engineering Science* 34.9 (1979), pp. 1166–1168.
- [3] M. J. Lockett and K.S. Bassoon. “Sedimentation of binary particle mixtures.” In: *Powder Technology* 24.1 (1979), pp. 1–7.
- [4] Y. Xia, Z. Yu, D. Pan, Z. Lin, and Y. Guo. “Drag model from interface-resolved simulations of particle sedimentation in a periodic domain and vertical turbulent channel flows.” In: *Journal of Fluid Mechanics* 944 (2022), A25.
- [5] M. Poletto and D. D. Joseph. “Effective density and viscosity of a suspension.” In: *Journal of Rheology* 39.2 (1995), pp. 323–343.
- [6] M. Rotondi, R. Di Felice, and P. Pagliai. “Validation of fluid–particle interaction force relationships in binary-solid suspensions.” In: *Particuology* 23 (2015), pp. 40–48.

PART III

ACKNOWLEDGMENTS

How time flies! Now I have reached nearly the end of my PhD journey. Looking back on this challenging yet thrilling journey, I am overwhelmed with the memories it brings and emotions it provokes. I could not have made it this far without the support and encouragement of the many people who went along with me on this journey.

First and foremost, I would like to express my deepest gratitude to my supervisor, Dr. Lorenzo Botto. Thank you for providing me this opportunity to work on this research project. I appreciate your guidance, your patience, and your belief in me even during the times when I struggled to believe in myself. Your insights and encouragement have made me grow not just as a researcher, but as a more mature person. Meanwhile, I want to thank my promotor, Prof. dr. Johan Padding, for your valuable inputs on my research. I am constantly inspired by your depth of knowledge and your humbleness.

I would also like to express my appreciation to the committee members: Prof. dr. Christian Poelma, Prof. dr. Dingena Schott, Dr. Blaise Delmotte, Dr. Selene Pirola, and Prof. dr. Wiebren de Jong, for their time and their constructive comments which have helped me to profoundly improve the quality of this thesis.

Special thanks to my group members: Dr. Hugo Perrin and (soon-to-be Dr.) Suriya Prakash, for all the stimulating discussions and fun activities we had together. I want to thank my master student, Ayoub Sihmidi, who contributed to some results of chapter 5. I also would like to thank my collaborators, Dr. Claire Chassagne and Dr. Ali Waqas, for welcoming me to visiting their lab in Deltares. It was my pleasure to have worked with you.

I would like to thank my past and current office members: Dr. Hugo Perrin, Dr. Rishabh Ghotge, Dr. Mengmeng Zhang, Dr. Sofen Kumar Jena, Dr. Giandomenico Lupo, Dr. Baptiste Hardy, Marko Draskić, Suriya Prakash, Sanath Kotturshettar, Shaina Blitt, Letizia Panciroli, Tarun Hegde, and Irem Gurbuz, for creating a very pleasant working environment with joy and laughter. I enjoyed our lunch and drink times and our group activities together. I also want to thank my other colleagues: Arvind Pari, Ravi Ramesh, Rumen Georgiev, Nagaraj Nagalingam, Pietro Carlo Boldini, Asif Hasan, Sowmya Kumar, and Jesse Reijtenbagh, for their help in certain ways.

Living abroad alone is certainly not easy. That is why I am very grateful to my Chinese friends: Dr. An Zhao, Dr. Teng Dong, Dr. Mengmeng Zhang, Dr. Rong Fan, Dr. Haoyu Li, Dr. Bin Fang, Dr. Wenze Guo, Dr. Pingping Cui, Dr. Shilong Fu, Fengyi Mi, Ning Ji, Bowen Sha, Qi An, and Zhaopeng Wang, for making me feel like home. I continue to be amazed by the fantastic cooking skills of most of you. Meanwhile, I

am also very grateful to my two brotherly friends in Delft, Faruk Özdemir and Nail İbrahimli. We have had so much fun together. I love you guys!

I am forever grateful to a group of friends who I met at the end of this journey: Avery, Julia, Dominik, Kamini, Penny, Elyshau, Shirae, MorningStar, Jeff, Nico, Marten, and Seval. I cherish the support and love we have given to one another, and I believe we will continue to do so. Love U!

Finally, I would like to thank my mom, for her unconditional love and support for me.

Heng Li
Delft, April 2025

CURRICULUM VITÆ

PERSONAL INFORMATION

FULL NAME: Heng Li

BIRTH DATE: 10-10-1994

NATIONALITY: Chinese

EDUCATION

2020-2025: PhD Research Scholar,
Process & Energy Department, Delft University of Technology, The Netherlands.

2017-2020: MSc in Fluid Mechanics,
Department of Engineering Mechanics, Zhejiang University, China.

2013-2017: BSc in Engineering Mechanics,
Department of Engineering Mechanics, Zhejiang University, China.

LIST OF PUBLICATIONS

* denotes equal contribution.

- [1] H. Li and L. Botto. “Hindered settling of a log-normally distributed Stokesian suspension.” In: *J. Fluid Mech.* 1001 (2024), A30.
- [2] H. Perrin*, H. Li* and L. Botto. “Hydrodynamic interactions change the buckling threshold of parallel flexible sheets in shear flow.” In: *Phys. Rev. Fluids* 8 (2023), 124103.
- [3] H. Li, L. Beetsma, S. Prakash, M. Mikkers and L. Botto. “Analysis and optimization of a multicascade method for the size fractionation of poly-dispersed particle systems via sedimentation or centrifugation.” In: (*To be submitted*), arXiv:2303.05257.
- [4] H. Li, W. Ali, A. Sihmidi, C. Chassagne and L. Botto. “Collective settling of spherical particles and implications for the experimental measurement of particle density.” In: (*To be submitted*).